RI | 9337

REPORT OF INVESTIGATIONS/1991

Coal Mine Entry Intersection Behavior Study

By K. Hanna, D. Conover, and K. Haramy

UNITED STATES DEPARTMENT OF THE INTERIOR

BUREAU OF MINES

DIALOG(R)File 6:NTIS
Comp & dist by NTIS, Intl Copyright All Rights Res. All rts. reserv.

1607877 NTIS Accession Number: PB92-178599/XAB
Coal Mine Entry Intersection Behavior Study
(Rept. of investigations/1991)
Hanna, K. ; Conover, D. ; Haramy, K.
Bureau of Mines, Denver, CO. Denver Research Center.
Corp. Source Codes: 005001006
Report No.: BUMINES-RI-9337
1991 87p
Languages: English
Journal Announcement: GRAI9215
Library of Congress catalog card no. 90-2477.
NTIS Prices: PC A05/MF A01

11/96

?

ALT-F10 HELP 3 ANSI-BBS 3 FDX 3 2400 E71 3 LOG CLOSED 3 PRT OFF 3 CR

Mission: As the Nation's principal conservation agency, the Department of the Interior has responsibility for most of our nationally-owned public lands and natural and cultural resources. This includes fostering wise use of our land and water resources, protecting our fish and wildlife, preserving the environmental and cultural values of our national parks and historical places, and providing for the enjoyment of life through outdoor recreation. The Department assesses our energy and mineral resources and works to assure that their development is in the best interests of all our people. The Department also promotes the goals of the Take Pride in America campaign by encouraging stewardship and citizen responsibility for the public lands and promoting citizen participation in their care. The Department also has a major responsibility for American Indian reservation communities and for people who live in Island Territories under U.S. Administration.

Report of Investigations 9337

Coal Mine Entry Intersection Behavior Study

By K. Hanna, D. Conover, and K. Haramy

UNITED STATES DEPARTMENT OF THE INTERIOR
Manuel Lujan, Jr., Secretary

BUREAU OF MINES
T S Ary, Director

Library of Congress Cataloging in Publication Data:

Hanna, K.

Coal mine entry intersection behavior study / by K. Hanna, D. Conover, and K. Haramy.

p. cm. — (Report of investigations; 9337)

Includes bibliographical references (p. 47).

Supt. of Docs. no.: I 28.23:9337.

1. Shaft sinking. 2. Rock mechanics. I. Conover, D. II. Haramy, Khamis Y. III. Title. IV. Series: Report of investigations (United States. Bureau of Mines); 9337.

TN23.U43 [TN283] 622 s—dc20 [622'.25] 90-2477 CIP

CONTENTS

ILLUSTRATIONS

ILLUSTRATIONS—Continued

TABLES

UNIT OF MEASURE ABBREVIATIONS USED IN THIS REPORT

deg	degree	in^2	square inch
ft	foot	lb	pound
ft^2	square foot	lb/ft^3	pound per cubic foot
ft^3	cubic foot	lb/in	pound per inch
h	hour	pct	percent
in	inch	psi	pound per square inch

COAL MINE ENTRY INTERSECTION BEHAVIOR STUDY

By K. Hanna,[1] D. Conover,[1] and K. Haramy[1]

ABSTRACT

This U.S. Bureau of Mines report describes a rock mechanics instrumentation program conducted in a shallow underground coal mine in central Illinois. This research program was designed to provide a basic understanding of the structural behavior of entry intersections. A wide variety of instruments and measurement techniques including hydraulic borehole pressure cells, multiple-point borehole extensometers, roof bolt compression pads, and overcoring were employed to monitor roof stresses, pillar loading, strata movement, floor heave, and bolt loading before, during, and after intersection development. A summary of intersection design theories, failure modes, and support techniques is included and instrumentation installation procedures and analysis methods are presented. The study identified two critical parameters that affect intersection stability: in situ horizontal stresses and geological discontinuities. Important design parameters for improving intersection stability are roof span and intersection geometry.

[1]Mining engineer, Denver Research Center, U.S. Bureau of Mines, Denver, CO.

INTRODUCTION

The design and stability of underground openings are problems of paramount importance in mining. Insuring the safety of employees, mining in a prescribed and efficient manner, and achieving an optimum recovery from the deposit depend on the ability of the mining engineer to design and excavate underground openings that will remain open for a suitable period. Historically, underground mine openings were designed by instinct and experience rather than by engineering methods. The scientific approach has been developed primarily in the last three decades.

The failure behavior in intersections is highly complex because of the three-dimensional nature of the intersection geometry. Intersecting openings may be of different shapes and sizes and may form a variety of intersection geometries. Although the most common types of intersections are the three-way and four-way intersections (fig. 1), many other types exist. Other types, such as the "X" and the "Y" types, are derivatives of the three-way and four-way types with different intersecting angles. Three-way intersections are more stable than four-way intersections, but are less stable than single entries.

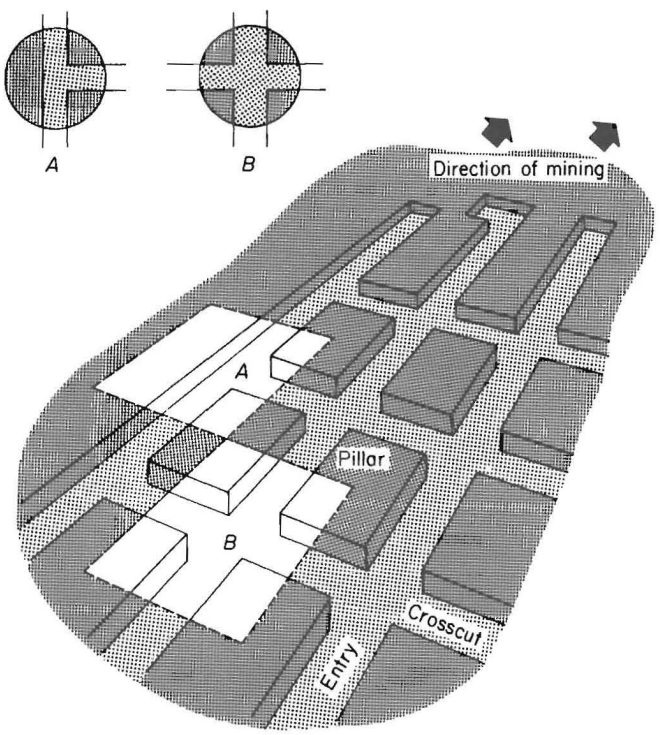

Figure 1.—Types of intersections in underground coal mines. *A*, Three way; *B*, four way.

The intersection region is characterized by conditions that are substantially different from those occurring around an individual opening. The conditions arising from the intersection development tend to reduce the stability of the intersection and result in a higher risk of roof and pillar failures.

The major factors influencing intersection stability are in situ stresses, geological discontinuities, intersection geometry, and intersection roof span. The magnitude of the in situ horizontal stresses determines the failure mode, shear or tension, and the size of the unstable dome over the intersection. Horizontal stresses may also promote excessive deformation and buckling of roof and floor members and may inhibit roof caving in full extraction operations. Geological discontinuities affect both the initiation and progression of failure. The planes of weakness represented by discontinuity surfaces greatly influence the shape and extent of ground failures. The proper orientation of entries and intersections with respect to the directions of horizontal principal stresses and geological discontinuities is a critical design requirement. The complex interaction of stresses, discontinuity surfaces, and entry geometry presents difficult design problems.

Coal mine entry intersections are responsible for a disproportionate number of roof fall fatalities in coal mines. The frequency of roof falls is greater in intersections than in other openings primarily because of the greater effective roof spans and associated stress concentrations. Statistics from underground coal mines reveal that a high percentage of fatalities occurred in intersection areas from roof or rib falls. Out of 897 total roof fall fatalities that occurred between 1956 and 1961, 298 fatalities occurred in intersection areas (*64*).[2] A more recent study conducted in 1980 (*57*) indicated that of 122 fatalities that occurred from 1977 through 1979, 37 fatalities occurred in coal mine intersection areas; 32% of these fatalities occurred at three-way intersections and 68% occurred at four-way intersections. Mine Safety and Health Administration (MSHA) statistics show that 25 miners died from falls of roof and ribs in coal mine intersections between January 1980 and January 1983. Typically, the roof area exposed in intersections constitutes approximately 15% of the total roof exposure from all mine openings, yet intersection areas account for approximately 30% of all roof fall fatalities. In addition, thousands of hours are lost as a result of injuries sustained from falls of face, rib, and

[2]Italic numbers in parentheses refer to items in the list of references preceding the appendixes at the end of this report.

roof at intersections. Therefore, reducing the risk of coal mine roof falls and evaluating structurally related ground control problems associated with coal mine intersections become major U.S. Bureau of Mines research objectives.

Despite their importance to both safety and productivity, intersections have not been studied adequately. So far, only few quantitative research studies have addressed mine intersection design and stability problems due to the lack of technical data. Those studies were limited to simple cases and were directed toward roof falls and pillar stability in general. A summary of relevant technical background information on intersection design theories, failure behavior, and support methods is presented in appendix A.

There is a need to establish both design criteria and guidelines and systematic computational procedures to provide the mining industry with safer and more efficient design methods to reduce the risk of coal mine roof falls, rib falls, and other hazards at intersections. Therefore, the Bureau initiated an in-house research project to investigate failure modes surrounding three-way and four-way intersections, and to provide answers to certain questions frequently being asked by the mining engineer, such as:

- How are these parameters structurally interrelated, and why is the analysis of the intersection failure mechanism so complex?
- What is the major or critical design parameter(s) that has the greatest impact on the stability of intersections?
- How can the influence of these parameters be minimized, or, if possible, eliminated?

The effort for this research is directed toward combining in-mine experience with results from actual field measurements and correlated computational analysis to develop improved mine design procedures for adverse ground conditions.

The objective of the research is to demonstrate, in the field, that potentially dangerous conditions existing in coal mine intersections can be reduced and/or eliminated by designing intersections based on a systematic integrated analysis approach. For instance,

1. Develop methods to determine the extent of the potentially unstable zone above a coal mine intersection for site-specific conditions.
2. Provide procedures to determine maximum safe roof spans (diagonally) at an intersection.
3. Develop guidelines and empirical relationships for the design of safer coal mine intersections.

The basic approach to achieve the above objectives was to instrument and monitor an intersection before, during, and after intersection development and to obtain stress and deformation data to characterize the structural behavior of entry intersections. The data were used to:

1. Identify critical parameters and their associated effect on the stability of intersections and entry system design.
2. Determine absolute and mining-induced stresses in the intersection roof, floor, and pillars.
3. Evaluate actual intersection failure mechanisms in mines with adverse ground conditions.
4. Provide explanations for observed failure modes based on theoretical analyses.

The research effort was conducted in three phases corresponding to three field investigations conducted in shallow, medium depth, and deep mines. This report summarizes the results for the shallow mine only. Results from the second and third phases and improved techniques for the design and support of safer entry intersections system have been reported in previous publications (*26-27*).

TEST SITE

A shallow mine in central Illinois was selected for the field investigation. The mine was experiencing ground control problems in intersections and was able to provide the special scheduling and operational accommodations necessary to conduct the field study.

A continuous room-and-pillar mining method is used to mine the flat-lying 7-ft-thick seam at a depth of 360 ft. The mine plan consists of eight-entry mains branching to submains and production rooms. The entries are 7 ft high by 20 ft wide, separated by 50- by 60-ft rectangular pillars. The entries and rooms are developed using drum type continuous mining machines and electric shuttle cars. The pillars are left intact to minimize subsidence.

Figure 2 shows a typical plan view of the face layout during development and the test site location. The faces at the end of each entry are developed along a line oriented at 45° to the longitudinal axis of the mains. Entry 1 on the intake side is advanced the furthest. Entry 2 is advanced about 70 ft short of entry 1, etc., such that entry 8 on the return is advanced the least. Crosscuts are generally developed toward the right side of the entries because the continuous miner operator has better visibility when making right-hand turns.

The entries are advanced in 20-ft increments and are supported by 3- to 8-ft-long roof bolts, depending upon the depth of a competent bed in the roof. The bolts are

installed on a semiregular 3- to 4-ft-square pattern and are normally installed through wooden header blocks for greater effectiveness. Bolt anchorage is achieved using expansion shells alone or with a combination of expansion shells and epoxy resin depending on rock conditions. Truss bolts, angle bolting, wooden posts spanned by steel crossbars, and cribs are used where supplemental support is needed.

The test intersection was located in entry 2 of the eight-entry main being driven to the north (fig. 2). Because the project objective was to investigate four-way intersections, the staggered pillar plan was modified to provide a four-way intersection for testing. As shown in figure 2, the numbers 1 through 35 indicate the sequence of mining in and around the intersection. Cuts 1 through 5 were completed in 1 week, and mine development at the test site was postponed for 2 weeks while most of the instruments were installed. After installation, cuts 6 through 35 were mined, and the remaining instruments were installed.

The primary roof support at the instrumented test site is 4-ft-long mechanical-anchor bolts, which suspend a 2-ft-thick shale layer from an overlying competent limestone layer.

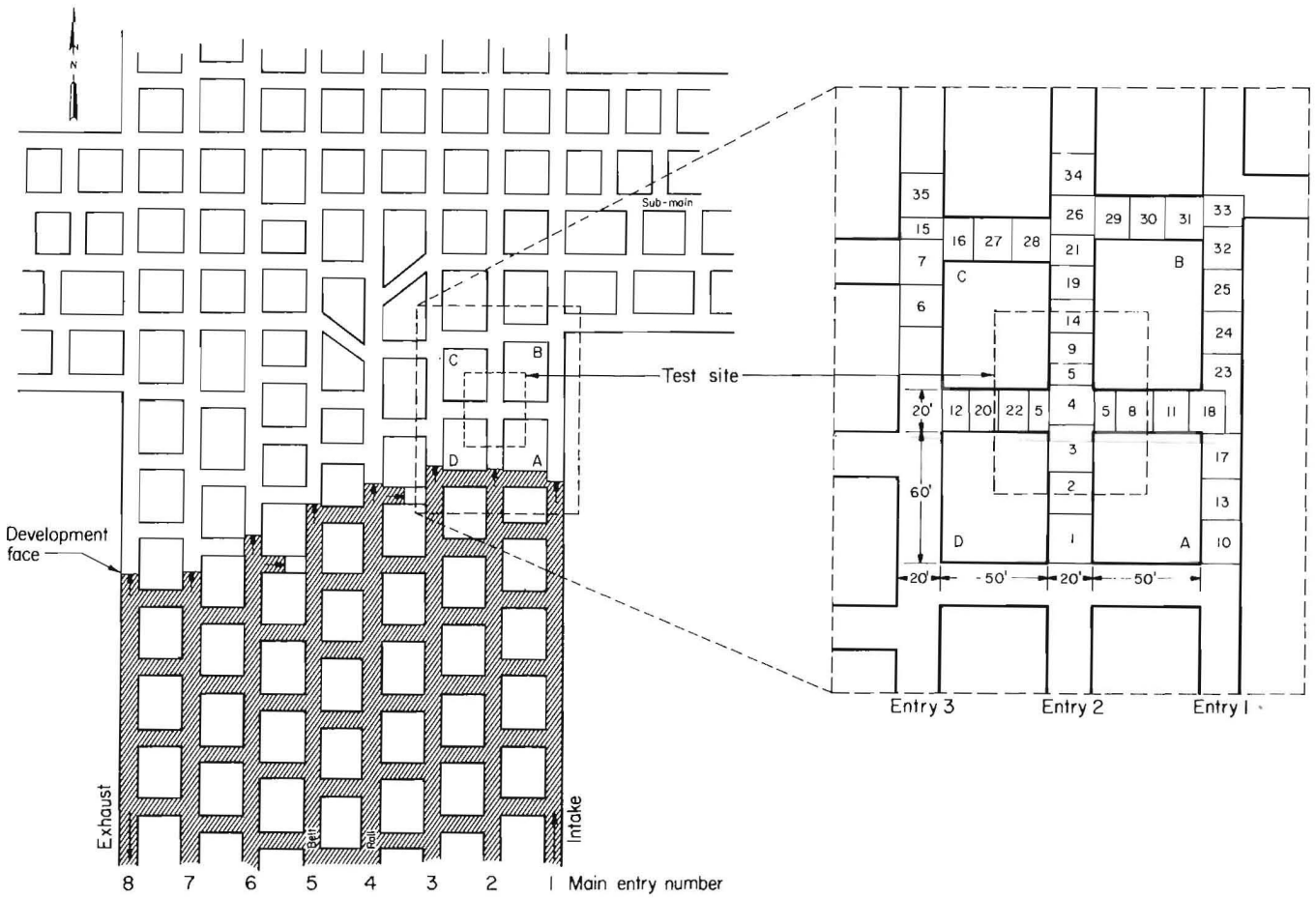

Figure 2.—Test site location and development sequence.

GEOLOGIC INVESTIGATION

Past research on the geologic factors affecting development of a minesite has been directed toward describing generalized features affecting roof stability. This section analyzes the site-specific geology of the study area as a prerequisite to determining stress conditions of a geologically variable mine roof.

The work was carried out in three basic steps. The first step involved collecting geologic information on the Illinois Basin and the coal seams worked in the area. The second step involved collecting information on the coal seam and the geologic factors affecting mine development. This step was accomplished by reviewing published material and through discussions with mine personnel. The third step involved the actual mapping of the intersection test site and surrounding entries. During this step, the roof geology was evaluated using (a) drilling data from roof bolt holes, (b) cores from instrumentation holes, (c) geologic data from the roof in adjacent entries, and (d) borehole scope observations. In the initial intersection area, 18 sections were mapped and 198 cleat and 8 joint measurements were taken in the coal and immediate roof (jointing was poorly developed in the roof shale). The direction, attitude, and quality of any slips encountered in development were also mapped. In addition, core was collected from four instrumentation holes in the roof.

MINE GEOLOGY

The research project is located in the west-central subdivision of the Illinois coalfield. The most important coal horizon within the subdivision is the Herrin No. 6 seam near the top of the Carbondale Formation (Pennsylvania System, Kewanee Group). The seam is persistent throughout a large part of the area, with thicknesses varying from thin to greater than 7 ft. Much of the thicker coal is found adjacent to the Walshville (Paleo) channel (*13, 42*).

The mine is located in the northern end of the thick Herrin No. 6 coal belt north of the Walshville (Paleo) channel. The coal seam averages 7 ft thick throughout the mine and contains two thin clay partings.

Roof conditions in the mine are variable, and are directly related to the roof geology. The most common roof lithologies are shale (the Anna Shale) and limestone, (the Brereton Limestone) and are termed the black shale-limestone roof type. Sandstone is not commonly present (*42*), but is found in some areas of the mine, including the test site.

The shale is madeup of two distinct subunits: the lower subunit, a hard, black fissile, slatey shale; and the upper subunit, a poorly bedded, mottled, weak shale containing two persistent thin bands of phosphatic nodules. The shale varies in thickness from 1 to 5 ft and is not present in all areas.

The limestone overlies the shale and forms the immediate roof where the shale is absent. The limestone consists of a lower layer of calcareous shale, termed clod by the miners, and an upper layer of massive gray limestone. The limestone can vary from less than 2 to more than 10 ft thick and is the primary determinant of roof stability in the mine. Roof problems are uncommon in areas of the mine where the limestone is thick and forms the immediate roof. However, where the limestone is less than 2 ft thick and pinches out and becomes shaley, roof falls are common. The roof, in these areas, is further weakened by the presence of slips and other deformational features and by the contacts between the limestone and shale beds, which constitute horizontal zones of weakness (*42*).

Poor roof conditions are, in part, the result of complicated geologic interrelationships between the different roof types. Area A (fig. 3) can be described as the black shale-limestone roof type. The immediate roof can consist of shale, clod, or limestone, and roof conditions are good provided the limestone is greater than 2 ft thick. In contrast, area B is a transition zone marked by a thinning or absence of limestone and represents an area of multiple-mining problems. Roof fall records indicate that area B consists of a thick section of rock varying from shale and siltstone to a more complex sequence containing clod, mudstone, soft, thinly layered or sideritic sandstone, and shale. Because of the variation in the vertical rock sequence, multiple zones of weakness are present and make roof support difficult. Area B is also characterized by the presence of slips in the roof and mud dikes in the coal and may experience increased water inflows if water-bearing sandstones encroach close to the coal.

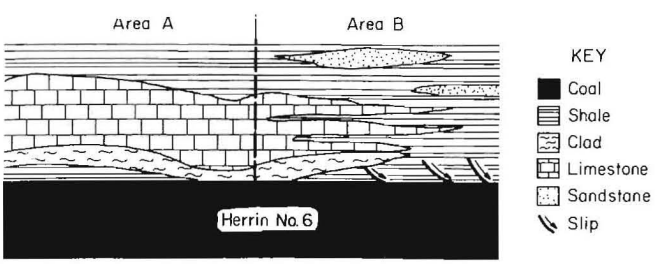

Figure 3.—Generalized geology of roof above Herrin No. 6 coal seam.

GEOLOGY OF STUDY AREA

The study area (fig. 4) includes entry 2, where the instrumentation was installed, and entry 3, which was developed ahead of entry 2. The mapped sections and all cleat and joint readings were taken in entry 2.

Roof Lithology

The roof above the study area can, in general, be described by the area B roof type discussed in the preceding section. The immediate roof (fig. 5) in entry 2 consists predominately of black, slatey shale from 1 to 3 ft thick having poorly developed joints. Pyrite lenses are common in the black shale and often separate and fall from the roof.

Two pots were mapped in the immediate roof in entry 2. The pot found on the northeast side of the entry (fig. 5) measured 0.9 ft in diameter and was separated from the surrounding shale by a pyrite layer. The second pot was not visible; its presence was predicted by the section supervisor from evidence of cracking and a circular, downward bowing of the immediate roof. The pot was located near A30 (fig. 4) where the rib intersects a zone of slips in the roof. Because of the presence of the pot and slip zone, the roof adjacent to sites A30 and A40 was unstable; approximately 0.5 ft of shale slaked from the immediate roof within 4 days.

In entry 3, the immediate roof was composed of black, slatey shale and gray shale (clod). The clod was present in patches extending from the face to the first outby crosscut and contained abundant pyritic films of marine fossils on exposed bedding surfaces. However, the fossils were too fragile to be retrieved intact for identification.

Information on the roof lithology above the shale in entry 2 was derived from bolthole drilling observations, holes cored into the roof, communication with mine personnel, and exposures in entry 3. The roof above the shale was composed of light-gray, massive, compact limestone with light and dark banding. In all core holes, the limestone was interbedded with dark limy shale. Crinoid stems and shell fragments were common in the limestone and the shale throughout the unit. The limestone-shale roof varied from 4.5 to 7.0 ft thick and was overlain by a black and often fissile shale bed 0.5 to 3.0 ft thick.

Sandstone was present above the limestone and shale in entry 2, as well as other entries in the section. Sandstone was found from 9.0 to 12.0 ft above the coal throughout entry 2, except at the northern end of the intersection where sandstone was not encountered (hole depth was 18.5 ft). In entry 3, a sandstone kettle bottom extended through the shale and was exposed in the roof. The sandstone, described from core and roof exposures, was a hard, light-colored rock with subangular, poorly sorted grains ranging in size from fine to medium grained. The cement consisted of calcite at the base, changing upsection into a noncalcitic silicious fill. The sandstone carries water as indicated by observed waterflow through extensometer holes that intercept the sandstone unit.

Slips

Slips are common features in the Herrin No. 6 coal seam and are associated with facies changes in the roof rock (*12*). The slips constitute planes of slippage in the roof strata and are similar to small faults. Although slips may displace the coal, no substantial displacement was observed in the study area. Three well-defined slip zones, composed of belts of one or more slips, were present in the study area. The strikes of these slip zones vary from N 35 E to N 80 E, but generally trend northeast. A fourth, poorly defined slip zone is present near the face in entry 2. This zone may be an extension of the third zone as no continuation of the zone was found in entry 3. The slip planes dip to the north and northwest at varying angles. Typically, the dip angle is relatively flat near the roof surface becoming steeper as the slip extends into the roof. Slips are believed to occur only in the immediate roof; however, a high-angle fracture in a limestone core sample taken near the second slip zone may indicate extension of the slips to greater depths. The slips in all four slip zones appeared predominantly like low-angle listric slips; however, the study area may also be intersected by higher angle slips or fractures. Irregular fractures in the upper portions of the coal seam may represent intersections between slips and the coal seam. In other areas, the slip surfaces parallel the roof bedding planes and do not enter the coal.

The slips in the study area are similar to those reported in literature (*12, 42*) with respect to their effects on roof stability. Slip development is generally localized in the immediate shale roof; however, extensometer measurements near slip zone no. 3 indicate that roof movement occurred at a depth exceeding 4.5 ft and may have occurred at a depth greater than 8.5 ft (see section on Strata Movement). Separation can occur anywhere along the slips, including areas where the slip surface is horizontal, thus creating planes of weakness in the roof and resulting in unstable conditions. Because the slips are concentrated in the immediate roof, falls typically extend only a few feet into the roof. Depending upon the geometry of the slip planes and the mine layout, the roof may fail at any time after coal extraction. In the study area, roof conditions did not begin to degrade until 2 to 3 days after development.

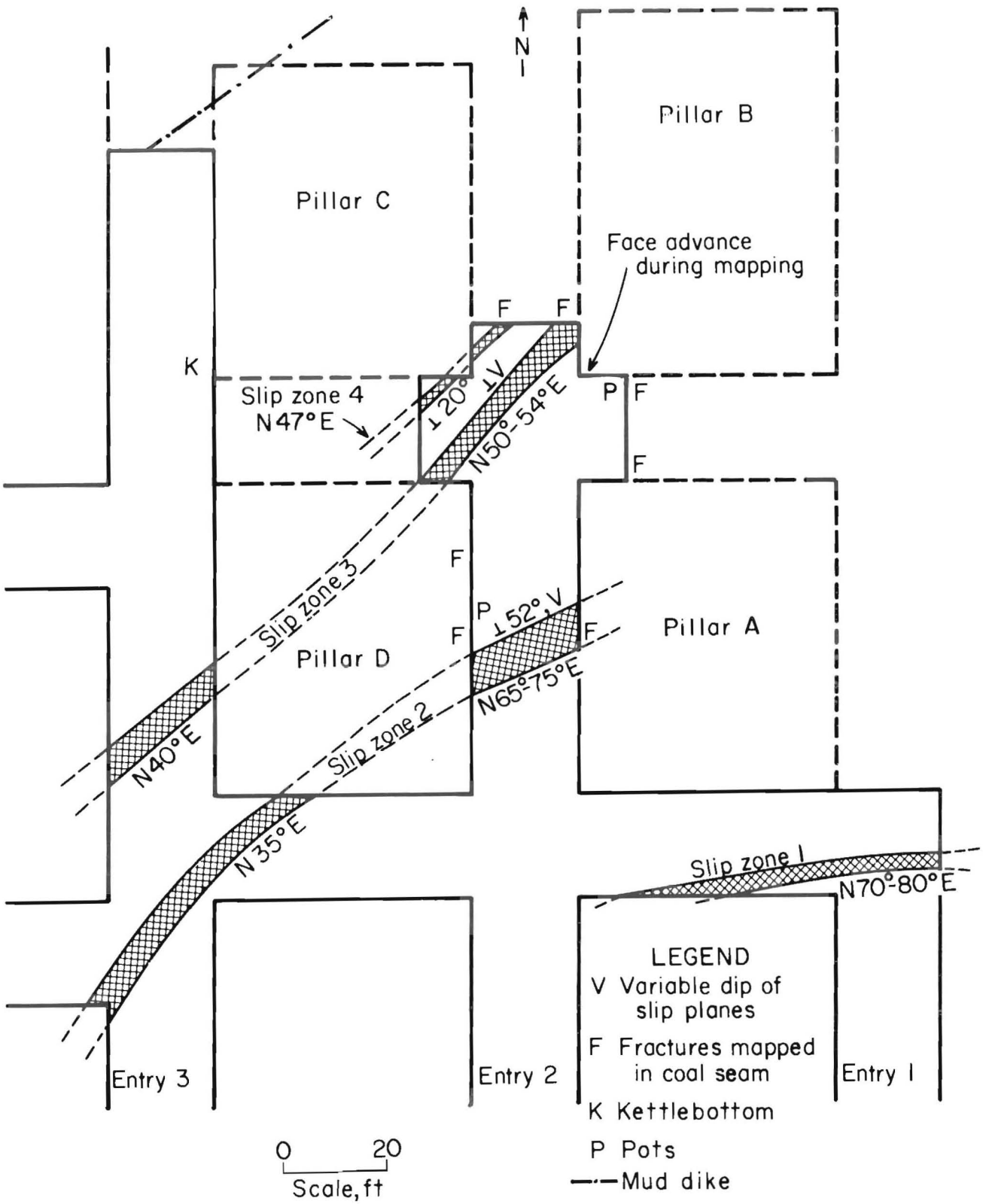

Figure 4.—Location and trends of slip zones and mud dikes in study area.

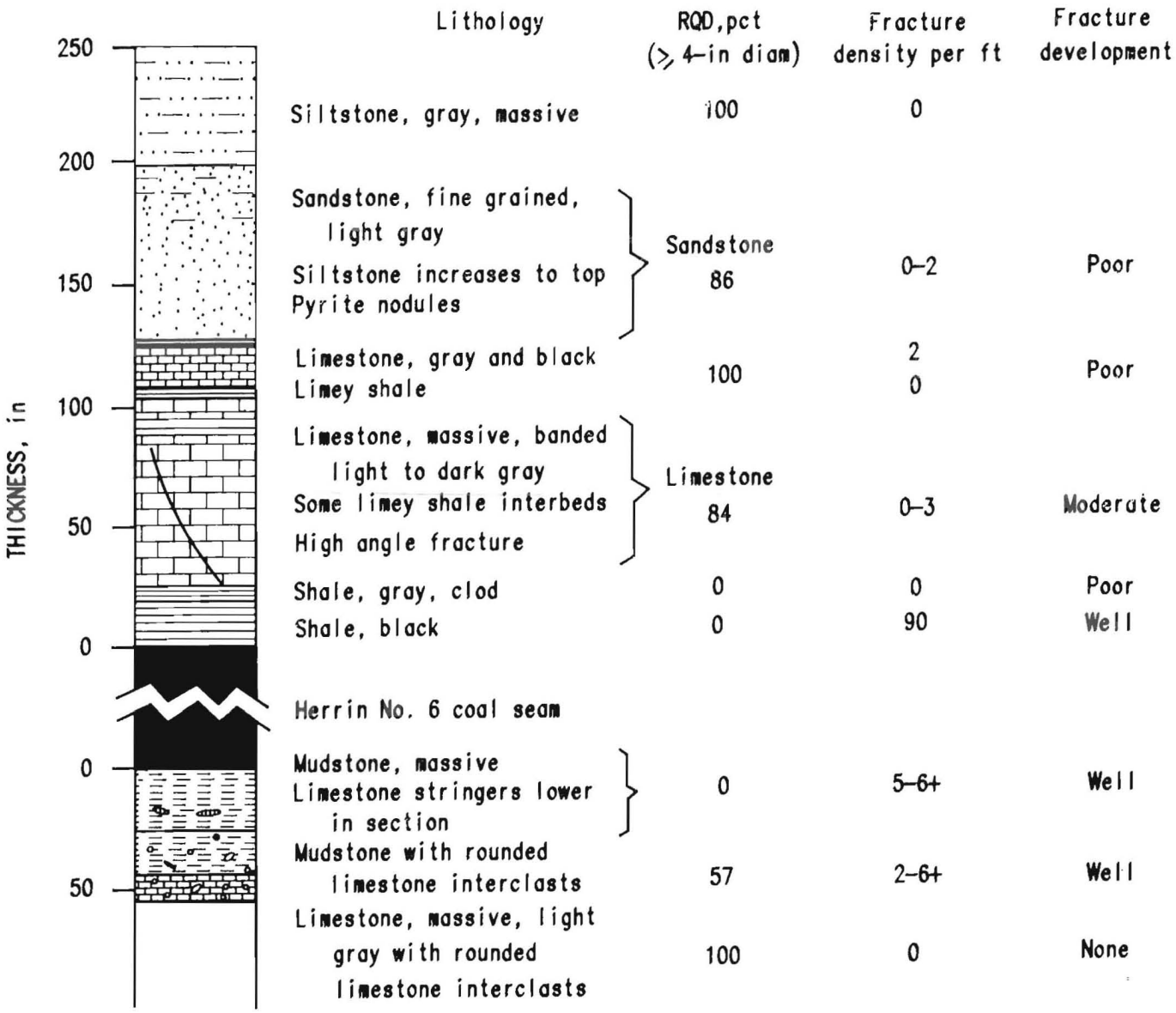

Figure 5.—Composite geologic column of coal, roof, and floor in entry 2.

Herrin No. 6 Coal Seam

The Herrin No. 6 coal seam at the test site ranged from 7.1 to 8.2 ft thick. The coal was black and banded with layers of impurities disseminated throughout the section. The banding was madeup of vitrain and dull attrital, with one to two fusain bands in the upper part of the seam. Vitrain occurred in thin to thick bands (0.02 to 0.4 in) containing 5% to 50% coal. The vitrain content increases upsection with the upper part of the seam containing up to 50% vitrain. Impurities found in the seam consist of pyrite bands and thin clay partings. One of the claystone partings (termed the "blue band" by the miners) varies from 0 to 1.6 in thick (fig. 6). This parting is commonly used as a marker bed throughout the Illinois Basin (*69*). In the study area, the blue band was 4.7 to 6.3 ft below the top of the coal bed. Another thin, discontinuous, claystone split occurs in the upper part of the coal from 1.2 to 3.4 ft below the top of the seam.

Cleat and Joint Development

Cleats in the coal were variable in both their trends and development. A total of 198 cleat and 8 joint measurements were taken in the study area. The primary (face) cleat is represented by N 30-50 W, and the secondary (butt) cleat is N 40-50 E.

Cleats were, in general, more well-developed near the top than near the base of the coal seam. Cleat density was also higher at the top than near the base. In most cases, cleat planes were vertical; yet, in some areas, cleat planes at lesser dips were also present. The measured dip angles for the cleat and/or fracture planes were 3°E, 80°SW, 28°N, and 86°S. Cleats were commonly infilled with mineral matter including: pyrite, an unidentified noncalcareous white mineral (possibly gypsum), and sphalerite (tentative identification).

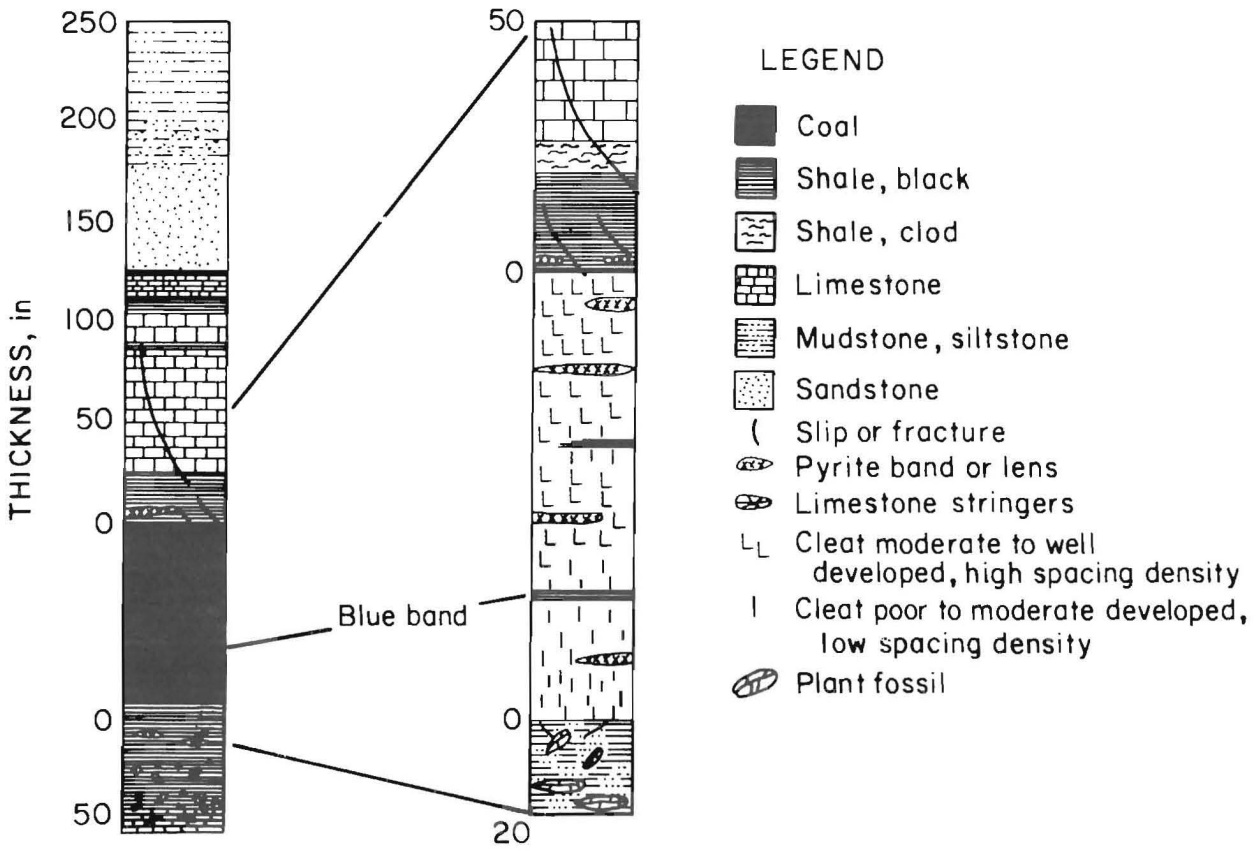

Figure 6.—Detail of coal horizon.

The measured joint attitudes were N 20-35 W, N 30 E, and N 60 E; however, jointing was poorly developed. The attitude of the secondary cleat corresponds to the attitude of jointing in the roof, a feature uncommon in the Illinois Basin.

Mud dikes can be present either as localized features in specific areas, or as linear features extending across several sections (*42*). The mud dikes present in the study area (fig. 4) consisted of a soft, gray clay material and were associated with slips and an increased flow of water into the mine workings. The two occurrences of mud dikes in the study area were presumed to represent two parts of a linear feature. The trend of this feature is N 55 E, which is similar to the trends of slips, cleats, and joints in the area.

Floor Lithology

The floor in the study area (figs. 5-6) consists of gray-white claystone that varies from 1.0 to 1.5 ft thick. The claystone is fossiliferous and contains predominately plant fossils. The soft claystone becomes plastic and sticky when wet and forms a poor floor.

Massive, gray, shaley limestone, 0.7 to 4.0 ft thick, underlies the claystone and contains 25% light gray intraclasts of a similar material.

COMPARISON OF STUDY SITE WITH REST OF MINE

In general, the geology of the roof and floor is similar to that found in other parts of the mine. The relationship between the shale, limestone, and sandstone, and the presence of mud dikes, slips, and wet areas are believed to be comparable with conditions found in sections previously developed. The coal is reported to be softer in some areas compared with the study site; yet, the thickness, in most cases, remains constant.

Similarities are also evident when comparing the structural data. Certain areas, designated as fault zones by the company, were not mined because of difficult mining conditions and occur as linear trends across the property. Average trends taken from company maps are N 36 E, N 55 E, N 45 W, N 75 W, and due west. The attitudes of slips in the area are N 35 E, N 40 E, N 47 E, N 54 E, N 65-75 E, and N 80 E. The major cleat directions are N 40-50 E, N 70-80 E, and N 30-50 W, and the trend of the mud dikes was approximately N 55 E. The primary and secondary directions of these structural features are summarized in table 1. In general, the agreement between the attitudes of cleats, slips, dikes, and mining faults shows a correlation between the structural makeup of both the study area and the overall mine. In addition, correlation was also observed between the directions of these structural features and the directions of the secondary horizontal principal stresses (see the section on Undercoring).

Table 1.—Directional trends of geologic structural features

Structural feature	Primary	Secondary
Faults	N 55° E	N 45° W
Slips	N 60° E	NAp
Joints	N 60° E	N 35° W
Mud dikes	N 55° E	NAp
Coal cleat	N 45° E	N 40° W

NAp Not applicable.

INSTRUMENTATION PLAN

The objective of the instrumentation plan was to obtain sufficient rock mechanics data to characterize the structural behavior of a four-way intersection, during and after development. The plan was implemented to collect three types of rock mechanics data: ground stress, strata movement, and geotechnical properties. The parameters investigated, techniques applied, and instruments used are shown in table 2. Figure 7 shows the instrument layout, and figure 8 illustrates an idealized diagonal vertical section through the pillars and roof.

A brief description of the specific techniques, instruments incorporated in the plan, and the placement rationale of these instruments is summarized below. Detailed descriptions of each instrument used, installation, and analysis procedures are presented in appendix B.

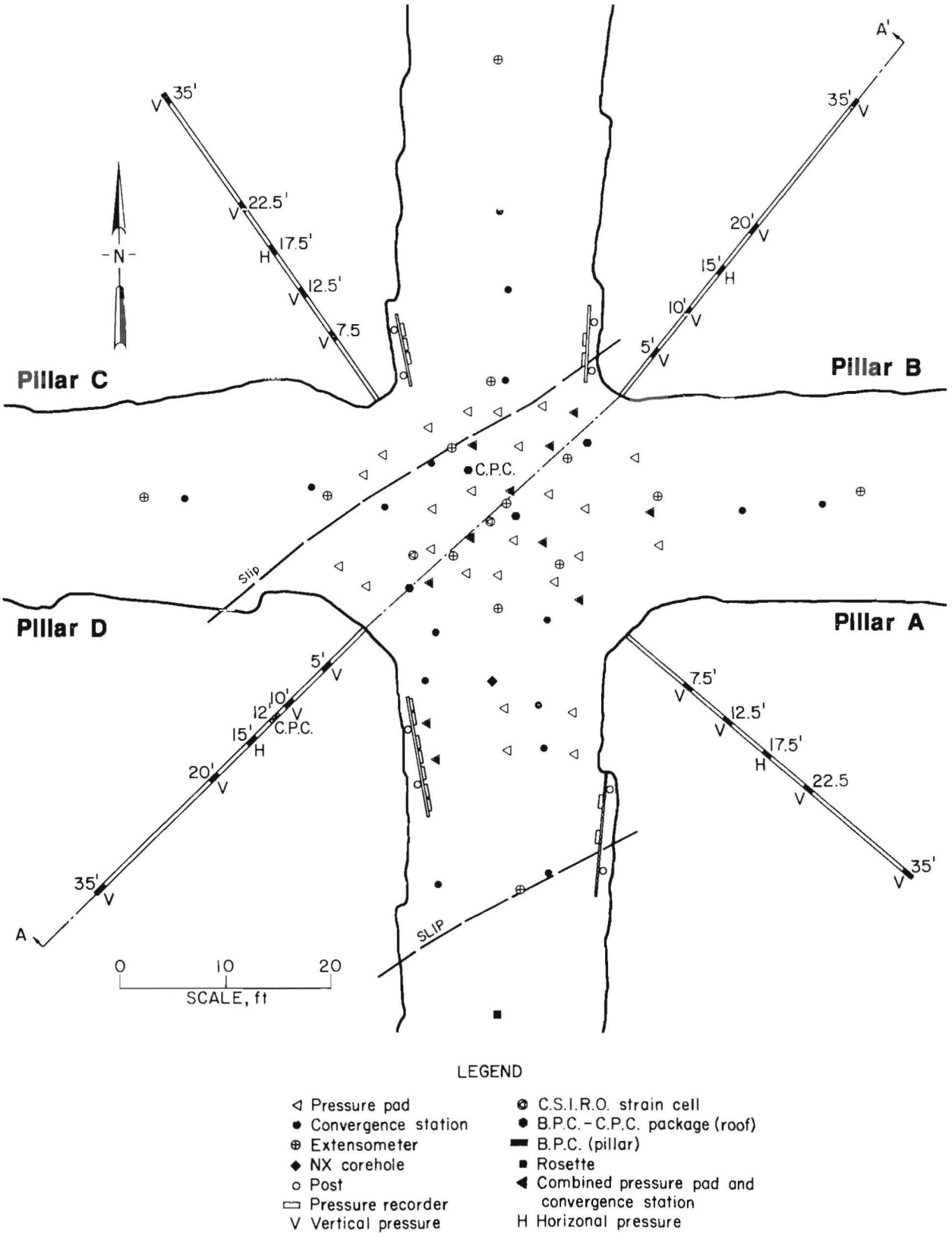

Figure 7.—Instrumentation layout for a four-way intersection.

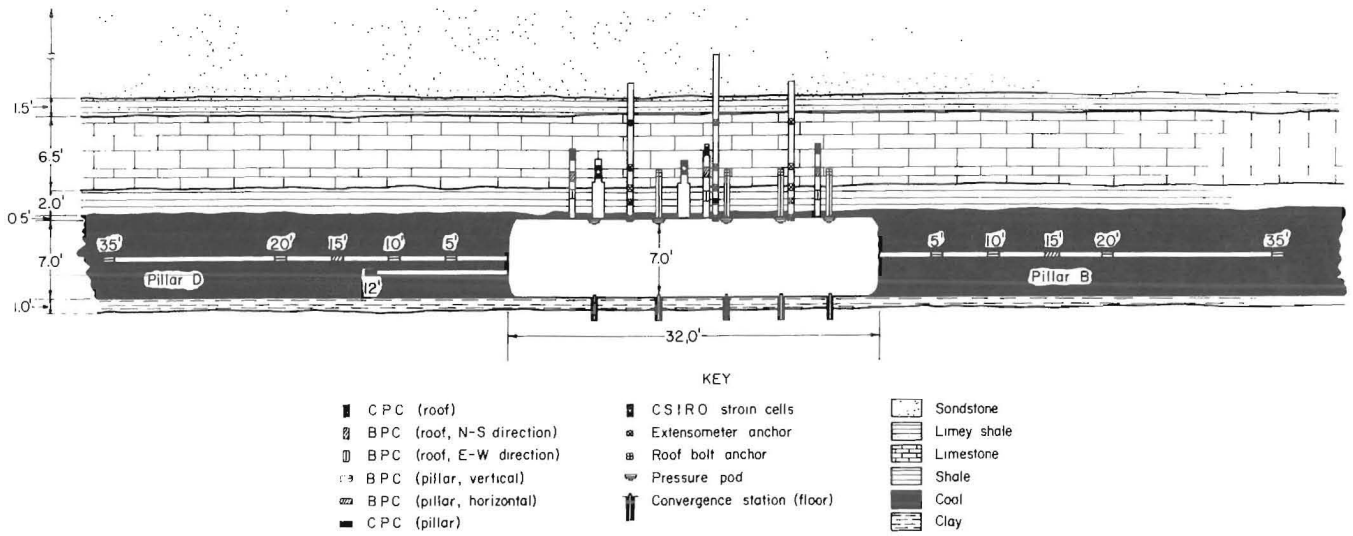

Figure 8.—Cross section A-A' of instrumentation layout.

Table 2.—Instrumentation requirements

Test method	Parameter	Instrumentation
	GROUND STRESS	
Two-dimensional undercoring	In situ stress	Whittemore strain gage.
Two-dimensional overcoring	.. do.	Borehole deformation gage.
Three-dimensional stress state	.. do.	Hollow inclusion stress cell-strain gage.
Pressure convergence-divergence	.. do.	BPC, CPC.
Pressure change measurements	Pillar loading	BPC, CPC.
	STRATA MOVEMENT	
Bolt loading	Roof bolt load	Compression pads.
Differential roof strata displacement.	Roof movement	Multiple-point extensometer.
Convergence measurements	Room closure	Telescoping closure meter.
	GEOTECHNICAL	
Geology	Rock-coal properties	Site mapping and borehole scope.
Laboratory	.. do.	NX core—roof, floor, coal.
In mine	.. do.	Borehole shear tester.

BPC Borehole pressure cell. CPC Cylindrical pressure cell.

GROUND STRESS

The in situ stresses and stress changes around the intersection must be known to assess adequately the response of some instruments and to provide boundary inputs for structural analysis. The rationale for conducting stress measurements was (a) to obtain the magnitude and direction of stresses in different roof lithologies (i.e., shale, limestone, and sandstone) (fig. 8); (b) to enable comparison of stress data obtained using different measurement techniques; (c) to determine stress distributions in pillars; and (d) to obtain stresses outside the zone of influence of the opening. The methods used to determine the in situ stresses are as follows:

(1) Two-dimensional undercoring and overcoring techniques (*6, 37*). The magnitude and direction of the secondary horizontal principal stresses were determined in the immediate roof and main roof from undercoring and overcoring, respectively. The test sites were located in entry 2 about 40 ft south of the instrumented site rather than in the intersection. This location was chosen because it is relatively uninfluenced by intersection stress concentrations.

The undercoring rosette, consisting of six measuring pins spaced 60° apart, was placed in the roof to determine horizontal stresses in the surface of the roof. The overcoring technique was used to determine the stresses in the roof at various depths. The stress-relief measurements were performed between 3- and 11-ft depths using the Bureau's three-component borehole deformation gauge.

(2) Three-dimensional overcoring (*71*). Two hollow inclusion strain cells (HISC) were installed 4 ft deep in the limestone roof layer to measure absolute and mining-induced stresses. The cells were located on the southwest-northeast diagonal to obtain stress profile across the critical (largest) intersection span.

(3) Pressure convergence-divergence. Two types of hydraulic borehole pressure cells were installed in the intersection roof and adjacent pillars: directional borehole pressure cells (BPC's) and nondirectional cylindrical pressure cells (CPC's). Since the intersection diagonal is the critical span in an intersection, the BPC-CPC instrumentation plan was designed to provide stress data from a diagonal pattern in the roof and pillars. Three packages, each consisting of two BPC's and one CPC, were installed in the roof at the center and at each end of southwest-northeast intersection diagonal (fig. 8). The BPC-CPC cells in each package were installed at 2-, 4-, and 6-ft depths in the shale and overlying limestone layers. The BPC's installed at 2-ft depths were oriented to measure pressure in the east-west direction, and BPC's installed at 4-ft depths measured pressures in the north-south direction. The CPC's were installed at a depth of approximately 6 ft to measure radial pressure. A fourth CPC was installed in the roof on the opposite diagonal. In addition, the BPC-CPC packages enabled comparison of stress data obtained from two- and three-dimensional overcoring methods by using pressure-stress equations developed by the Bureau (*45*).

Twenty BPC's were installed diagonally in the pillars and oriented to record horizontal and vertical pressure changes (fig. 7). The cells in two pillars (B and D) were installed at 5-, 10-, 15-, 20-, and 35-ft depths, while the cells in the other two pillars (A and C) were installed at 7.5-, 12.5-, 22.5-, and 35-ft depths. The BPC's installed at 15- and 17.5-ft depths monitored horizontal ground pressures. The remaining BPC's monitored vertical ground pressures. Also, a CPC was installed in pillar D, in a separate borehole located 12 in below the BPC's hole at 12-ft depth (fig. 8). The rationale for placement of the BPC's at 5 ft intervals from the pillar corner was based on the yield zone depth predicted from Wilson's confined core theory (*70*).

STRATA MOVEMENT

The roof was monitored to evaluate failure modes, roof bolt loading, roof strata displacement, and floor heave. Thirty-six compression pads were installed throughout the intersection in a semiregular square pattern to measure the load on roof bolts.

Thirteen multiple-point-borehole extensometers (MPBX), each consisting of four spring anchors, were installed in the intersection roof and in each of the adjoining entries and crosscuts (figs. 7-8). The anchor depths were selected after examining the NX (2.145 in diam) core taken from the roof and inspecting the drilling data from roof bolt holes. The selected anchor depths were 1.5, 2.7, 4.5, and 8.5 ft and were the same for all stations. The MPBX stations were strategically positioned (a) to evaluate the effect of intersection widening on roof strata movement, and (b) to compare bed separation of various roof layers along the intersection diagonal and the axis of entries. Twenty-seven convergence stations were installed using telescoping closure meters in the intersection and entries to monitor mining-induced floor heave relative to roof surface horizon (including roof sag). The convergence station layout in the intersection generally coincided with the intersection diagonals. The layout in the south entry consisted of two rows of stations, each row approximately 2 ft from the ribline. The layout in the other entries consisted of a single row of stations along the center line.

GEOTECHNICAL DATA

The methods and instruments used to obtain geotechnical data, other than those covered by ground stress and strata movement, are generally related to geology and physical properties of rock and coal. The methods used are as follows:

(1) Laboratory physical property tests. Core samples were obtained from an NX (3-in diameter) borehole drilled 20 ft in the roof immediately south of the intersection to conduct uniaxial and triaxial compression tests. Core from 0 to 3.5 ft of the immediate roof was not tested because of the poor core quality of the shale; however, the stronger overlying limestone and sandstone layers and the weaker overlying siltstone layer were tested. A short NX hole was also drilled in the floor, but was abandoned because of a high-clay content which prevented further drilling.

The NX borehole was used for conducting two additional tests: borehole shear tester and borehole scope monitoring.

(2) Borehole Shear Tester (BST). The cohesion and angle of internal friction of in situ rock were determined using the BST (*31*). Since the roof was composed of different lithologies, BST tests were conducted in the NX borehole at 1-ft intervals to a depth of 5 ft, and 5-ft intervals to a depth of 15 ft. At each depth, the BST was rotated about 45° between tests to ensure that undisturbed rock was being tested. Testing was attempted in the floor; however, the hole had become offset, preventing insertion of the instrument.

(3) Borescope. A borescope, consisting of a miniature TV camera, was inserted into the NX borehole and into selected roof extensometer boreholes to observe the change in stratigraphy across the intersection and adjacent entries. The unit performed well in clean holes, but the effectiveness was very limited in most holes due to the rapid accumulation of mud on the lens.

DATA COLLECTION PROGRAM

Data were collected during intersection development and long-term stabilization, which occurred within 6 months. Figure 9 shows the instrument installation sequence and monitoring schedule during initial development and intersection widening. Numbers 1 through 35 show the cut sequence of the continuous miner machine in and around the intersection. Based on the need to gather data before and after intersection development, instrument installation and intersection development were conducted according to the following schedule:

(1) The entry was advanced approximately 90 ft past the projected inby side of the intersection as indicated by the cut sequence 1 through 5 (see initial development configuration in figure 9). During this phase of development, roof bolt compression pads and convergence stations were installed in the entry immediately south of the intersection and throughout the intersection. The compression pads were installed during the normal roof bolting cycle, following the standard roof bolting pattern used at the mine. The pads were read using a calibrated ring, before and immediately after installation and periodically thereafter. In addition, the torque applied to the bolts was measured and recorded.

Convergence was measured between roof bolts and reference rods grouted in the floor using a telescoping closure meter having 0.01-in resolution. The measurements were repeatable and only a single reading was required at each station.

(2) Development was suspended for about 2 weeks while the BPC's-CPC's, HISC's, and roof extensometers were installed and baseline data were collected.

The BPC-CPC cells were installed 4 to 6 days prior to intersection widening. The cells were connected by steel tubing to circular-chart continuous-pressure recorders. The recorders accommodate two or three channels, and have a range of either 5,000 or 10,000 psi. The setting pressure for all cells was approximately 800 psi. The two HISC's were connected to a digital strain indicator through a 10-channel switching box, and the indicated readings were recorded on specially prepared forms.

The boreholes for the extensometer stations were drilled by the roof bolter during the bolting cycle. Data collection consisted of reading a dial gauge positioned between brass sleeves attached to each anchor wire and a copper cap at the collar of the hole. Only one measurement was taken for each anchor, because of close repeatability inherent in the system.

(3) Normal mining operations resumed, and the intersection was widened by extending the entry and crosscuts from the intersection, as indicated by the cut sequence 6 through 35. The remaining convergence stations and extensometers were installed after intersection development was completed.

Initially, instruments were monitored daily to provide complete coverage of the rapidly changing stress and deformation conditions. Once the measurements stabilized, the monitoring frequency was decreased to weekly intervals throughout the remainder of the data monitoring program. The overcoring tests were performed at the end of the data monitoring program.

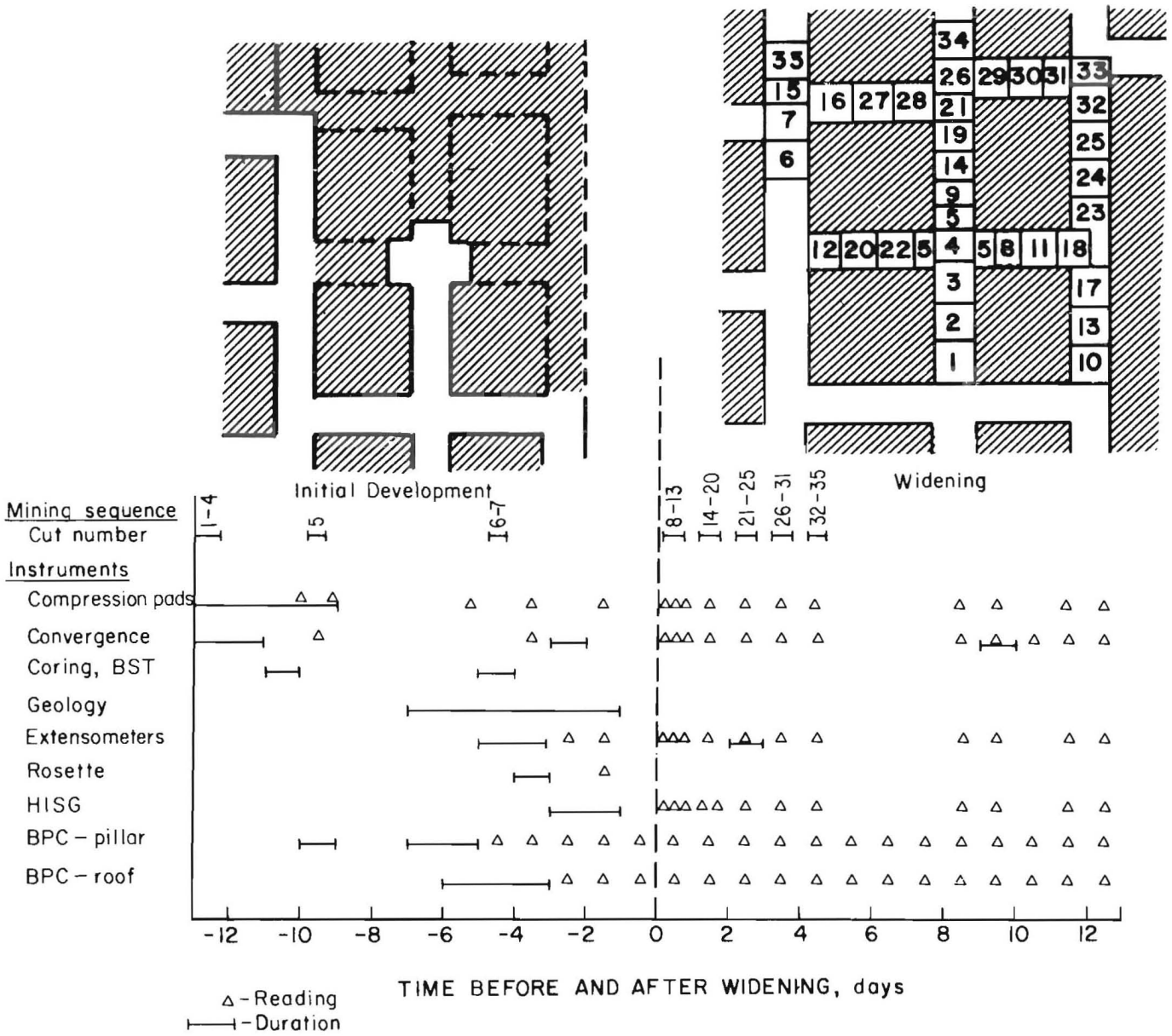

Figure 9.—Instrument installation sequence and data collection.

DATA ANALYSIS

The field and laboratory measurements were analyzed in two phases: a reduction phase and an interpretation phase. The reduction phase involved determining the validity of the measurements and converting the measurement data into the corresponding structural parameters. Most reduction was accomplished using established methods; however, modified techniques were developed to analyze the pressure-cell data. The interpretation phase involved evaluating the validity of the reduction methods and analyzing the ground conditions around the test intersection by comparing the reduced data against various models of structural behavior. These analyses involved both short-term and long-term effects and were conducted for three subcategories: geomechanical properties, ground pressures, and strata movements.

GEOMECHANICAL PROPERTIES

Geomechanical properties were determined using in situ techniques and laboratory compression testing methods. The roof properties were determined at several depths using both in situ and laboratory tests. The coal properties were tested only in the laboratory. No testing was performed for the floor rocks owing to poor immediate floor conditions that prevented core drilling.

In Situ Physical Properties

The BST (*31*) was used in the NX corehole drilled in the roof immediately south of the intersection to obtain in situ physical properties of the roof rock. Data were collected at various depths in the roof. At each depth, initial normal (radial) pressures of 500, 1,000, 1,250, and 1,500 psi were applied. Shearing (axial) pressure was applied until a sudden drop in pressure occurred, indicating failure.

From the normal and shear pressures and calibration curves supplied with the BST, normal and shear stresses were calculated. Table 3 lists the measured pressures and calculated stresses for each test and the values of cohesion, S_o, and friction angle, ϕ, determined from linear regression analyses. Figure 10 shows BST plots of shear stress versus normal stress and the fitted regression lines for each depth. Although the regression lines correlate well with the data, the analyses predict negative cohesion values at several depths. It is believed that these negative values are the result of either the expected regression error associated with the small number of data points or, more likely, slippage of the BST body, particularly at the lower normal pressures due to existence of water in the hole. The cohesions calculated from the BST data are much lower than the cohesions determined from laboratory tests. Although the borehole shear tests and laboratory compression tests involve similar volumes of rock, the borehole test locations may be influenced by discontinuities not present in laboratory samples. Thus, the in situ cohesion values are not expected to be as great as the laboratory values. Because of the uncertainty associated with the negative cohesion values, neither the cohesions nor the friction angles were used in any subsequent analyses.

Table 3.—Borehole shear tester data analysis

Test depth, ft	Pressure, psi		Stress, psi		Cohesion, psi	Friction angle, deg
	Normal	Shear	Normal	Shear		
15	475	510	1,152	808	638	2.4
	980	350	2,467	529		
	1,380	400	3,508	617		
	1,480	650	3,769	1,053		
10	450	550	1,087	878	398	29.2
	880	1,150	2,206	1,925		
	1,200	1,150	3,040	1,925		
5	560	450	1,373	704	-284	39.8
	875	1,050	2,193	1,750		
	1,250	1,450	3,170	2,448		
	1,475	1,600	3,756	2,709		
4	550	550	1,347	704	-99	38.3
	950	1,200	2,389	2,012		
	1,250	1,325	3,170	2,230		
	1,400	1,625	3,560	2,753		
3	500	525	1,217	835	-114	39.3
	1,000	1,175	2,519	1,968		
	1,125	1,375	2,844	2,317		
	1,475	1,700	3,495	2,884		
2	475	350	1,152	529	137	18.5
	925	550	2,324	878		
	1,200	750	3,040	1,227		
	1,375	775	3,495	1,271		
1	500	350	1,217	529	-52	23.2
	925	550	2,324	878		
	1,200	725	3,040	1,183		
	1,500	1,000	3,821	1,663		

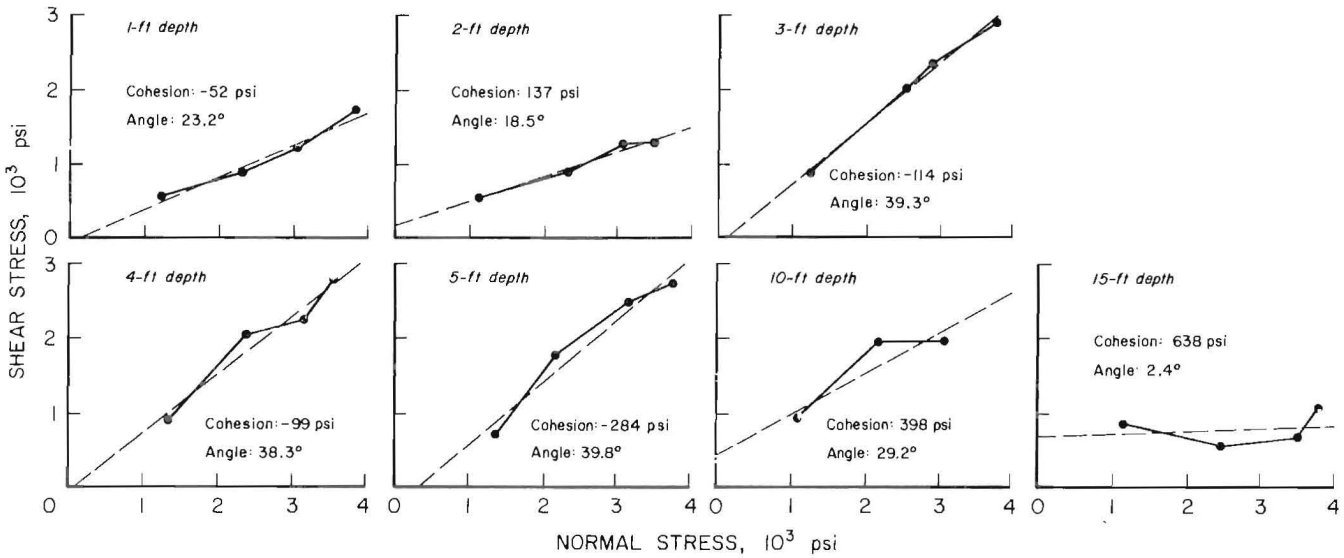

Figure 10.—Shear stress versus normal stress—BST plots.

Laboratory Test Results

Uniaxial and triaxial compression tests were performed on NX core samples taken from the mine roof to determine the uniaxial compressive strength, C_o, Young's modulus, E, and Poisson's ratio, ν. The test results are shown in table 4. The procedures used to calculate these values are discussed below.

Table 4.—Uniaxial and triaxial test results of cores from roof at 2 entry (2.145-in-diam sample, 2:1 sample length-diameter ratio)

Core sample depth range, in	Lateral pressure (σ_3), psi	Breaking load (P), lb	Compressive strength, (σ_1), psi	Young's modulus[1] (E) 10^6 psi		Poisson's[1] ratio (ν)	
				Tangent	Secant	Tangent	Secant
LIMESTONE—2.71 AVERAGE SPECIFIC GRAVITY							
42.5- 46.5	0	86,200	23,852	6.532	4.608	0.28	0.17
45.5- 49.5	500	49,500	13,697	4.760	4.048	NAp	NAp
49.5- 53.5	1,000	95,800	26,508	5.627	4.899	NAp	NAp
58.5- 62.5	1,500	69,600	19,258	3.943	3.030	NAp	NAp
66.5- 70.5	2,000	95,800	26,508	5.012	4.205	NAp	NAp
71.0- 75.0	0	60,500	16,740	2.153	2.027	.40	.32
79.5- 83.0	500	46,300	12,811	5.455	3.379	NAp	NAp
99.0-103.0	1,000	3,900	10,791	2.349	1.892	NAp	NAp
119.0-124.5	1,500	48,700	12,475	2.694	1.719	NAp	NAp
SANDSTONE—2.58 AVERAGE SPECIFIC GRAVITY							
126.5-130.5	2,000	14,800	31,765	6.256	6.170	NAp	NAp
134.0-138.0	0	42,800	11,843	3.264	1.917	0.26	0.10
142.0-146.5	500	51,000	14,112	3.917	3.450	NAp	NAp
146.5-151.0	1,000	57,600	15,938	3.792	3.215	NAp	NAp
SILTSTONE—2.51 AVERAGE SPECIFIC GRAVITY							
180.5-184.5	2,000	28,600	7,914	0.921	1.028	NAp	NAp
189.5-193.5	0	10,000	2,767	.631	.525	0.44	0.30
204.5-209.0	500	24,050	6,655	1.019	.553	NAp	NAp
222.5-227.0	1,000	19,500	5,396	.836	.938	NAp	NAp
245.0-249.5	1,500	26,700	7,388	.956	1.135	NAp	NAp

NAp Not applicable, lateral deformation monitored for uniaxial tests only.
[1]Evaluated at one-half breaking load and corrected for deformation of steel platens.

Young's Modulus and Poisson's Ratio

These parameters were derived from plots of axial load versus deformation recorded continuously during the compression tests. Axial deformation was monitored for all tests, therefore, Young's modulus was calculated for each sample. Lateral deformation was monitored for only the uniaxial tests, therefore, only four samples were evaluated for Poisson's ratio. Both parameters were evaluated at one-half the breaking load and were corrected for deformation of the steel platens.

Uniaxial Compressive Strength

Since the uniaxial compressive strength test results were limited, it was necessary to determine an average uniaxial compressive strength for each rock type. Thus, an equivalent compressive strength was calculated for each triaxial sample. This was accomplished by fitting a straight line to the triaxial test data to determine the triaxial stress factor (slope of the fitted line). An equivalent uniaxial compressive strength was computed for each sample, using the following equation:

$$C_o = \sigma_1 - k\sigma_3 \qquad (1)$$

where C_o = uniaxial compressive strength, psi,

σ_1 = axial stress at failure (compressive strength), psi,

σ_3 = confining stress (lateral pressure), psi,

and k = slope of the fitted line (triaxial stress factor).

Figure 11 shows the axial stress versus confining stress plots of the triaxial test data for each rock type. Points 8, 9, 10, 14, and 17 were disregarded for the analysis due to slightly different rock characteristics near a shale parting and/or fracture in the rock sample. It was assumed that for each given rock type, the triaxial stress factor would remain relatively constant despite the variability in compressive strength between individual samples. Therefore, a line parallel to the fitted line was passed through each data point, and the intersection with the axial stress axis was determined to represent the equivalent uniaxial compressive strength for that sample.

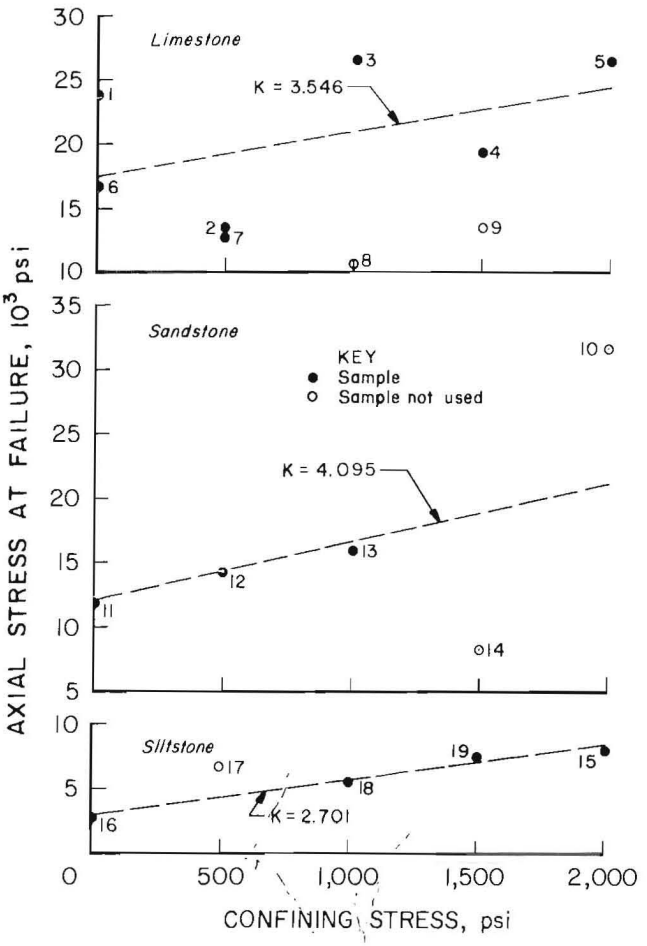

Figure 11.—Axial stress at failure versus confining stress.

Angle of Internal Friction

For each rock type, the angle of internal friction, ϕ, was calculated from the triaxial stress factor, k, using the relation:

$$\tan\phi = \frac{k - 1}{2\sqrt{k}}. \qquad (2)$$

Cohesion

The cohesion, S_o, was calculated from ϕ, and C_o, using the formula:

$$S_o = \frac{C_o\,(1-\sin\phi)}{2\cos\phi}. \qquad (3)$$

Table 5 lists the derived values of equivalent compressive strength and cohesion for each sample and the angle of internal friction for each rock type.

Table 5.—Derived physical properties

Sample	Equivalent uniaxial compressive strength (C_o), psi	Cohesion (S_o), psi
LIMESTONE—34.1° ANGLE OF INTERNAL FRICTION		
1	23,852	6,333
2	11,924	3,166
3	22,962	6,097
4	13,939	3,701
5	19,416	5,156
6	16,740	4,445
7	11,038	2,931
8	7,245	1,924
9	7,156	1,900
Average[1]	17,124	4,547
SANDSTONE—37.4° ANGLE OF INTERNAL FRICTION		
10	23,575	5,825
11	11,843	2,926
12	12,064	2,981
13	11,843	2,926
14	2,020	499
Average[2]	11,883	2,944
SILTSTONE—27.4° ANGLE OF INTERNAL FRICTION		
15	2,513	765
16	2,767	842
17	5,305	1,614
18	2,695	820
19	3,337	1,015
Average[3]	2,828	860

[1]Samples 8 and 9 not included.
[2]Samples 10 and 14 not included.
[3]Sample 17 not included.

GROUND PRESSURES

Mining-induced and in situ stresses were determined using BPC's-CPC's, HISC's, and the overcoring and undercoring techniques.

Hydraulic Borehole Pressure Cells

BPC's and CPC's were installed in the roof and pillars 1 week prior to intersection widening. An idealized representation of cell pressure from the time the cells were installed through the end of the monitoring period is shown in figure 12. The following four distinct stages were observed for all cells: (1) before the intersection was widened, (2) immediately after widening, when transient effects are present, (3) after widening, when transients

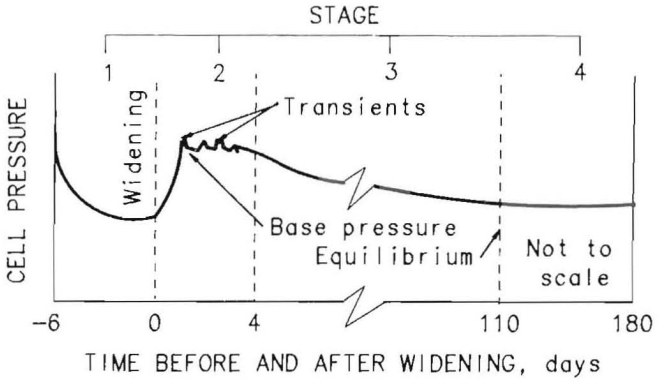

Figure 12.—Typical cell pressure record.

have disappeared, but before equilibrium is reached, and (4) after equilibrium. In general, the cell pressures showed a decreasing trend over time, which can be attributed to adjustments of the cells and the rock mass in reaching equilibrium. Immediately after widening, the cell pressures changed significantly from the stage 1 pressures and typically consisted of a base pressure with superimposed transient pressure increases. These transient changes were most common for the roof cells and generally varied less than 200 psi from the base pressure. The transient effects disappeared approximately 4 days after widening, when the four pillars surrounding the intersection were completely developed. The transient variations from the base pressure occurred over periods of less than 1 h to greater than 6 h. The longer transient periods generally occurred immediately after development when the active working faces were nearest the intersection. The shorter transient effects occurred near the end of stage 2.

It is thought that the transient behavior indicates the redistribution of stress around local failures, slips, etc., and is not representative of actual stress conditions. Therefore, subsequent analyses of stress changes ignore the transient effects and consider only the changes to the base pressures. The base pressures of the roof and pillar cells for stages 1 and 2, when the greatest changes occurred, are presented in figures 13 and 14. The cells measuring vertical ground pressures in the pillars recorded an increase in pressure after widening, whereas the horizontal pressures in the pillars and in the roof decreased.

Analysis of the pressure cell data involved calculation of the stress changes and the absolute stresses in the roof and pillars during intersection widening. The pressure convergence method (*45*) and the theory of inclusions (*50, 61*) were used to calculate the absolute stresses, and equations

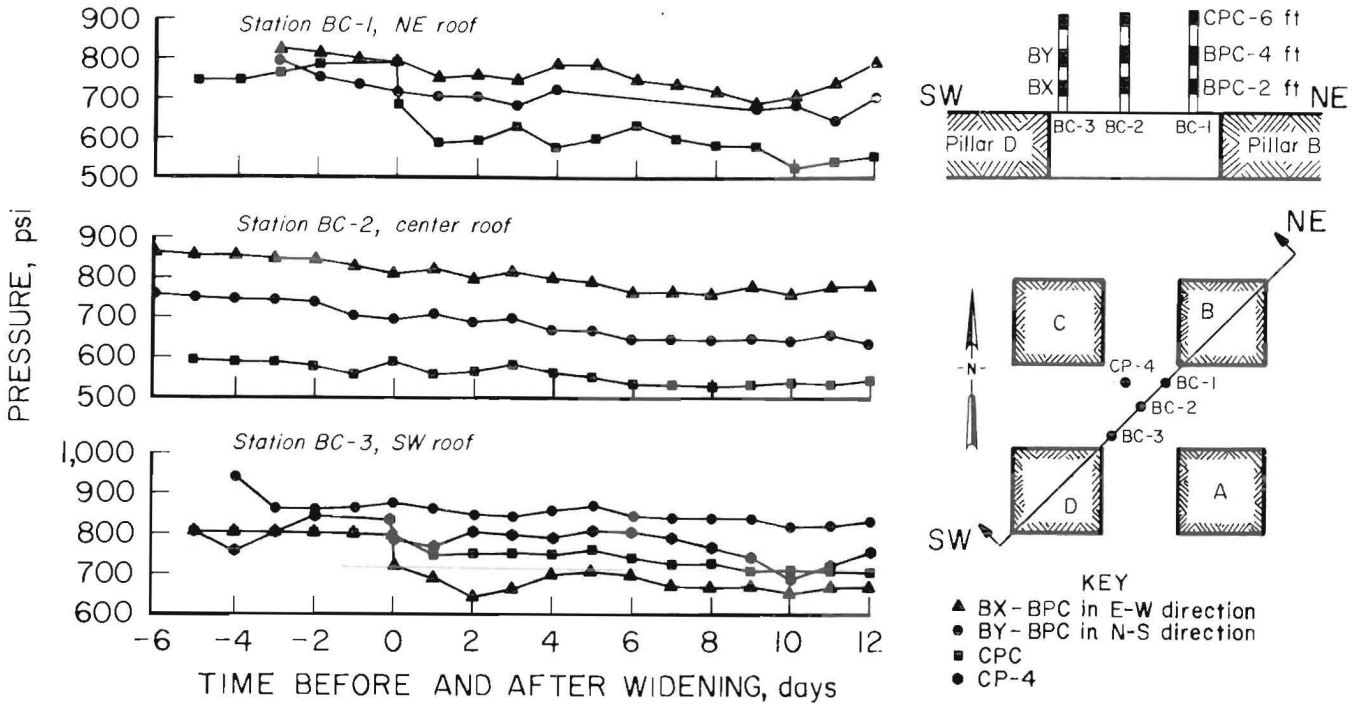

Figure 13.—BPC-CPC pressure profiles in intersection roof.

developed by Babcock (*4*) were utilized to obtain absolute stress changes. These methods are sufficient for analyzing pillar pressures; however, they do not provide for circumstances where the cells are installed in different materials or in a nonuniform stress field. Since the cells installed in the roof were located in both shale and limestone layers, the response of the two BPC's in each package may be significantly different. In addition, the stiffer limestone layer may carry a higher load than the softer shale layer, thereby imposing different stresses on each BPC. To account for these special conditions in the roof, the basic analysis equations were modified to use separate response factors and stress reduction factors for each cell. Details of the analysis procedure are discussed in appendix C. The resultant calculated stresses are presented in the following sections.

Pillar Stresses and Stress Changes

The calculations of pillar stresses and stress changes from the BPC data were simplified because all the cells were installed in the same rock type, coal. However, certain assumptions were required in analyzing the pillar data since not all measurement points contained the required number of cells for a complete analysis. These assumptions involved the distributions of both horizontal and vertical stresses within the pillars and the uniformity of the response factor in all pillars. The procedures used in determining pillar stresses and stress changes are detailed in appendix C.

Figure 15 shows the calculated absolute pillar stresses for each pillar throughout the monitoring period. The stresses shown before the time equilibrium was reached (110 days) are included only to show the relative behavior of the cells in reaching equilibrium. The stresses after equilibrium show little change, which is expected due to the lack of nearby mining activity. The distribution of vertical pillar stresses at the end of the monitoring period is shown by the solid lines in figure 16. The stress distributions are generally uniform, except pillar B, which may have been influenced by geologic conditions in the roof over the pillar.

The pillar stress changes accompanying intersection widening are shown in table 6. The stress changes were calculated using two methods as described in appendix C. Figure 17 shows the variation between the distribution of stress changes calculated using the two methods. The shapes of the distributions are similar; however, the magnitudes of the stress changes do not agree. The stress changes calculated using method 1 were used to estimate the premining absolute stresses shown by the dashed lines in figure 16.

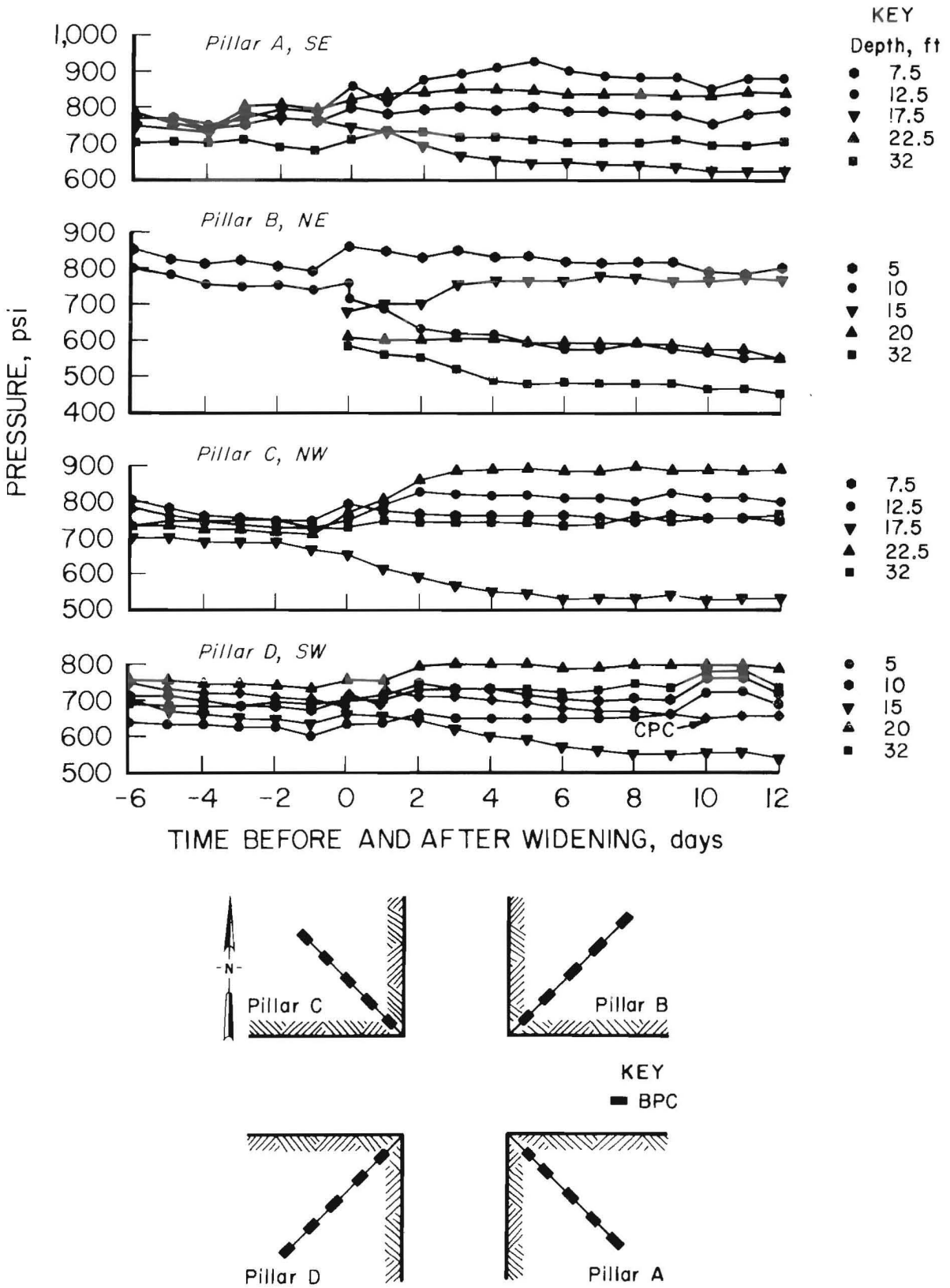

Figure 14.—BPC pressure profiles in pillars.

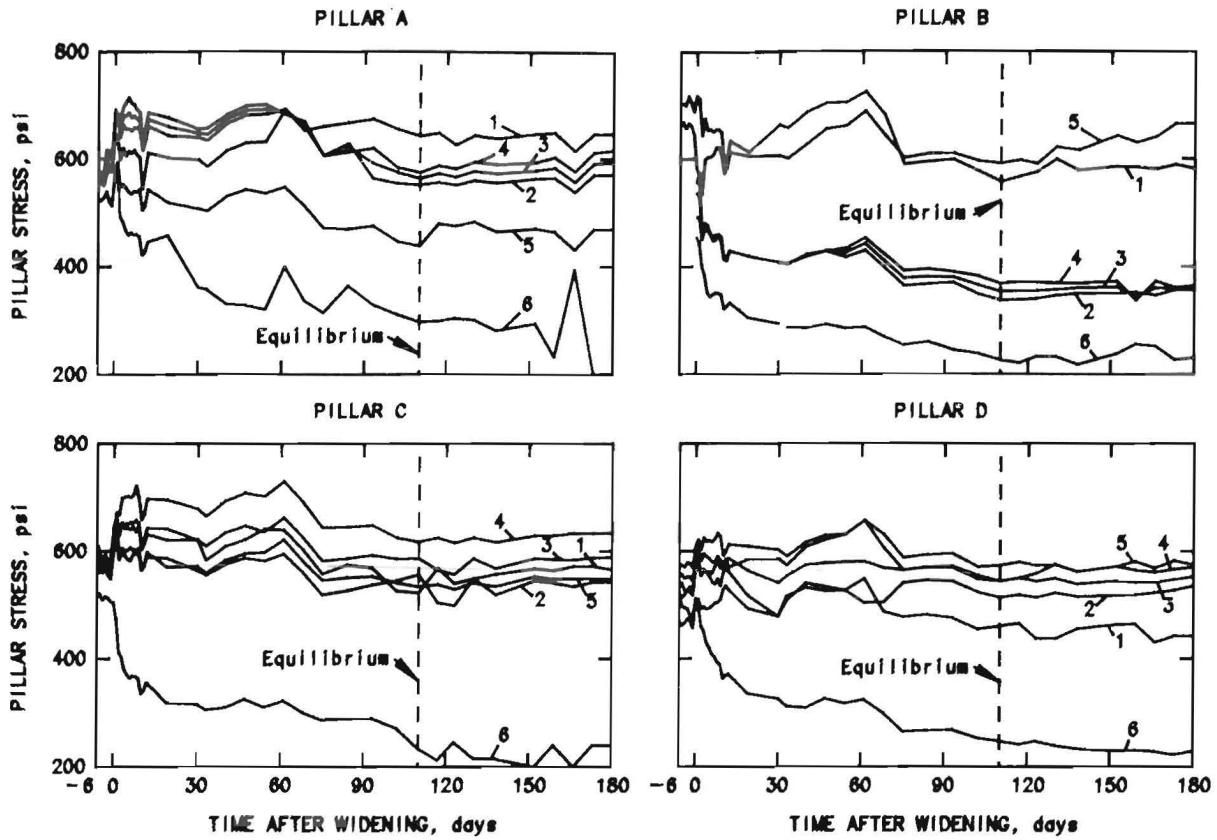

KEY

Curve	Stress component	Depth from pillar corner, ft			
		A	B	C	D
1	Nx	7.5	5.0	7.5	5.0
2	Nx	12.5	10.0	12.5	10.0
3	Nx	17.5	15.0	17.5	15.0
4	Nx	22.5	20.0	22.5	20.0
5	Nx	32.0	32.0	32.0	32.0
6	Ny	17.5	15.0	17.5	15.0

Figure 15.—Pillar stresses during monitoring period.

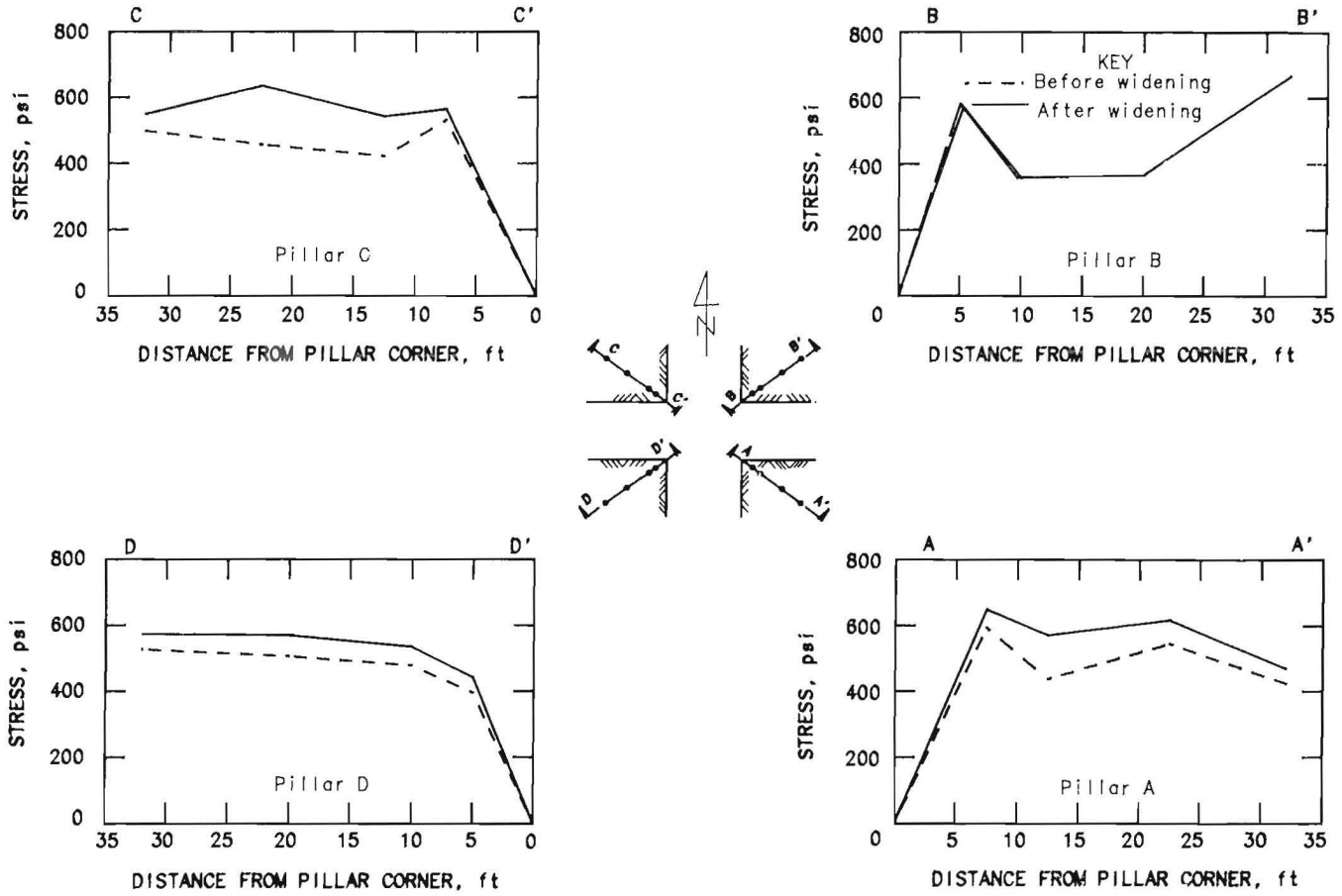

Figure 16.—Distribution of vertical pillar stress.

Table 6.—Pillar stress changes, pounds per square inch

Pillar and cell depth, ft	Pressure		Stress change	
	Initial	Final	Method 1[1]	Method 2[2]
A:				
7.5	750	800	55	26
12.5	770	910	133	109
17.5	750	660	-91	-78
22.5	780	850	72	44
32.0	680	720	46	20
B:				
7.5	750	770	34	-19
12.5	700	820	120	88
17.5	670	550	-123	-120
22.5	710	900	179	152
32.0	720	760	51	4
C:				
5	600	650	47	59
10	660	720	57	65
15	620	590	-33	-18
20	730	800	64	68
32	680	730	47	52

[1]Modified inclusion method (*50, 61*).
[2]Babcock method (*4*).

Roof Stresses and Stress Changes

Figure 18 shows the variation of absolute roof stresses over time in the limestone layer. The stresses in the shale layer assumed to be approximately 16% of the stresses in the limestone. The reduction of stress shown for package 3 near the end of the monitoring period corresponds to several small roof falls, which occurred between roof bolts near the cell package. The small stress changes indicated by the pressure cells are consistent with the lack of nearby mining activity. Table 7 lists the roof stress changes calculated using the two methods described in appendix C. The shapes of the stress change distributions are comparable for the two methods, except the north-south component at the southwest corner. The stress changes calculated for method 2 are also much larger magnitude than the stress changes determined using method 1. Method 2 is more sensitive to variations of input pressures and the large discrepancies may be the result of errors in digitizing the recorder charts or calibrating the pressure recorders.

Table 7.—Roof stress changes, pounds per square inch

Package location, strata, and cell type	Pressure		Stress change			
	Initial	Final	Method 1[1]		Method 2[2]	
			E-W	N-S	E-W	N-S
Northeast corner:						
Shale, borehole pressure	780	770	-2	1	-11	16
Limestone, borehole pressure	710	730	-13	6	-67	103
Limestone, cylindrical pressure	790	600	NAp	NAp	NAp	NAp
Center:						
Shale, borehole pressure	800	800	0	-1	-8	-24
Limestone, borehole pressure	690	670	1	-4	-50	-149
Limestone cylindrical pressure	550	550	NAp	NAp	NAp	NAp
Southwest corner:						
Shale, borehole pressure	800	700	-22	2	-184	-53
Limestone, borehole pressure	840	850	-141	14	-1,158	-333
Limestone, cylindrical pressure	790	740	NAp	NAp	NAp	NAp

NAp Not applicable.
[1]Modified inclusion method (*50, 61*).
[2]Babcock method (*4*).

Hollow Inclusion Strain Cells

The Commonwealth Scientific and Industrial Research Organization (CSIRO) hollow inclusion strain cells provided data regarding the stress changes during widening and the long-term absolute stresses in the roof. The cells were installed along the northeast-southwest intersection diagonal approximately 50 in above the roofline. One cell was installed near the center of the intersection and the other cell was placed approximately 4 ft from the southwest pillar corner. The cells were installed 2 days before the intersection was widened to allow measurement of the stress changes caused by widening. The cells were overcored approximately 8 months after installation to allow measurement of long-term absolute stresses and for comparison with stresses determined from the BPC-CPC packages and from overcoring tests using the Bureau's borehole deformation gauge.

The cells were monitored weekly after the initial development period until the cells were overcored to permit back calculation of absolute stresses throughout the monitoring period. However, calibration problems with the readout equipment prevented determination of the initial and short-term stresses and only the stress changes could be analyzed.

Overcoring was performed with a 6-in-diam thin-wall bit using established techniques. Strain readings were taken at 1-in intervals, and both cores were recovered intact for biaxial testing. The overcores were tested in the biaxial chamber at a pressure of 1,000 psi to determine the elastic constants. When the overcores were sawn in half to inspect the adequacy of the bonding, air bubbles were observed in the epoxy resin over the strain rosettes; however, it is not known to what extent the bubbles influenced the cell response. The strain logs obtained during overcoring and biaxial testing were normal, and the elastic constants determined from the biaxial test are consistent with the values obtained from laboratory tests of the NX core. Therefore, it is determined that the influence of the air bubbles is not significant, and that the calculated stresses are accurate.

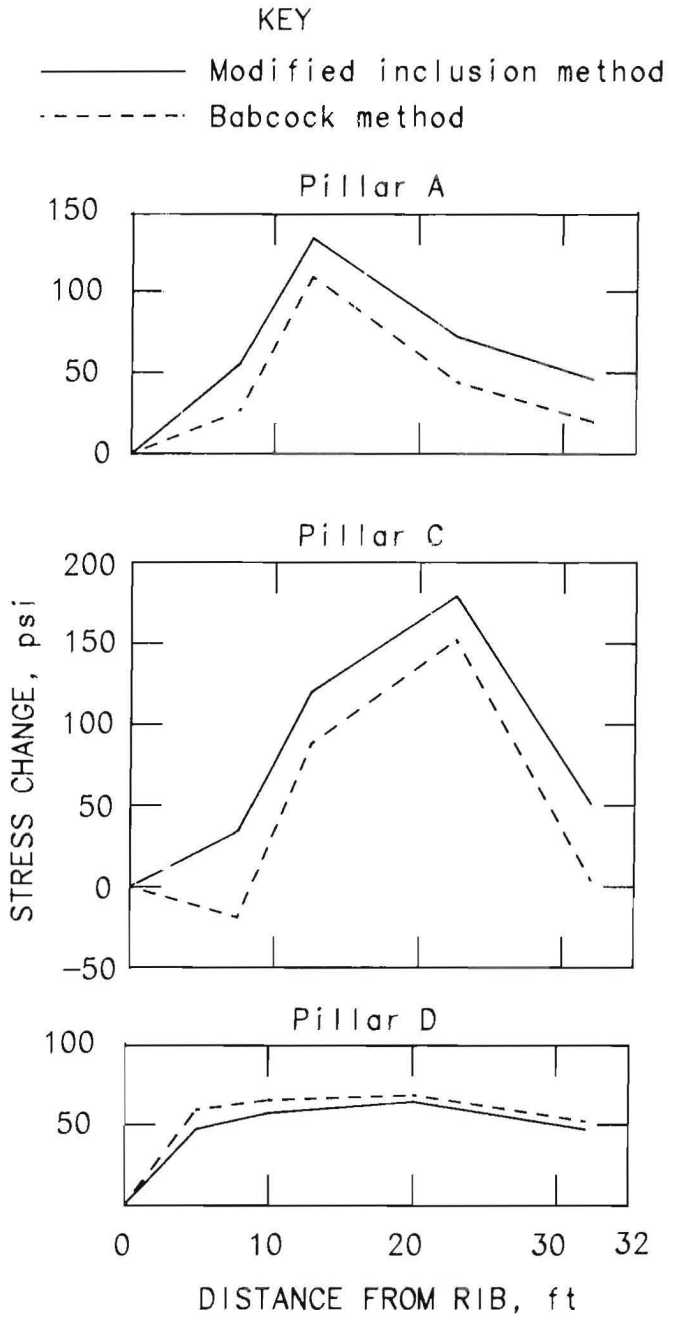

Figure 17.—Pillar stress changes.

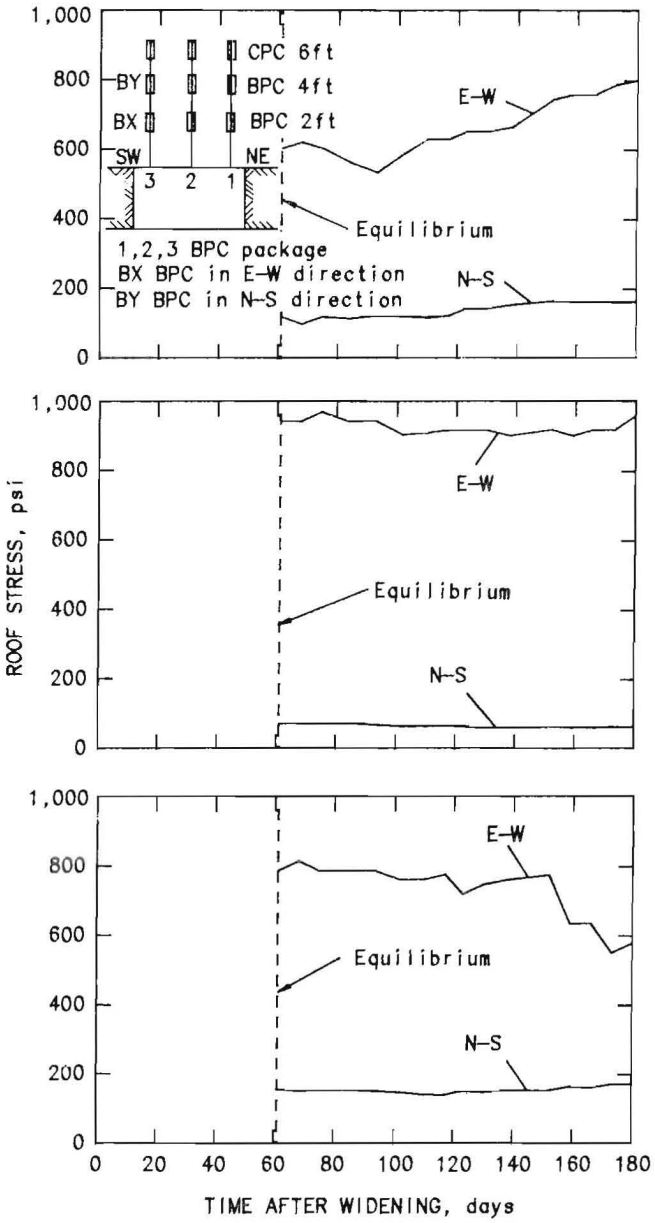

Figure 18.—Horizontal roof stresses measured by instrumentation packages. Top, package 1; middle, package 2; bottom, package 3.

The overcore data were analyzed statistically to determine the three-dimensional stress field around each cell. The magnitude and direction of the primary principal stresses for both cells are given in table 8. The magnitudes of the stresses determined from each cell are similar, while the stress directions are different. The principal stresses for cell 1, nearest the southwest pillar, are approximately aligned with the intersection diagonals, as expected; however, the principal stresses from cell 2, nearest the center, are more closely aligned with the entries.

Table 8.—Primary principal stresses in roof using hollow inclusion strain cells (Azimuth measured clockwise from north, dip measured from horizontal downward)

	Cell 1	*Cell 2*
Depth ..... in ...	50	53
Young's modulus (E) ..... 10^6 psi ...	5.21	5.31
Poisson's ratio (υ)	0.42	0.38
Stress field 1:		
Principal stress (compressive) ..... psi ...	-530	-1,654
Azimuth ..... deg ..	138	106
Dip ..... deg ..	9	4
Stress field 2:		
Principal stress (compressive) ..... psi ...	-1,964	-484
Azimuth ..... deg ..	229	198
Dip ..... deg ..	9	16
Stress field 3:		
Principal stress (compressive) ..... psi ...	-1,382	-355
Azimuth ..... deg ..	4	2
Dip ..... deg ..	77	73

For comparison with the BPC-CPC results, the component stresses aligned with the entries were calculated. The secondary principal stresses in the horizontal plane were also determined and are shown in figure 19.

Figure 20 shows the relative changes of the principal stresses for each cell from the time the cells were installed until overcoring. The large fluctuations in stress after approximately 3-1/2 months are caused by a weak battery in the readout box. The battery replacement resulted in a calibration change, which was provided for by adding a constant to the readings before battery changing. The stresses in the roof, before widening, increased (became less compressive) from 300 to 700 psi after mining the first two cuts. Further development had less significant effects and the stresses gradually became more compressive, indicating that the stresses were stabilizing.

Another possible cause of the stress fluctuation is horizontal shifting of the roof layers or other local failures. When the cells were overcored, significant offsets were observed in the 6-in-diam holes, which required redrilling

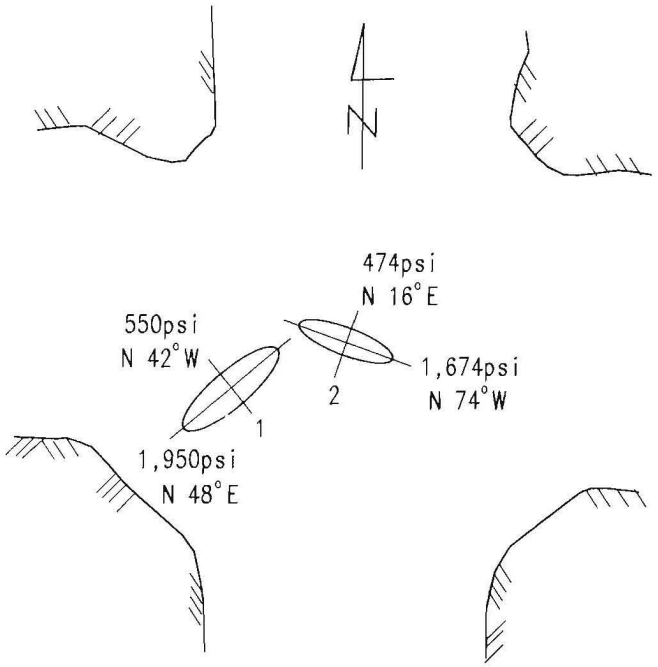

Figure 19.—Roof secondary principal stresses from HISC overcoring.

before overcoring could proceed. A small roof fall, observed during the monitoring period, coincided with a definite stress change. Thus, the stresses redistributed around local failures may cause significant stress changes at the cell locations.

The Bureau's Borehole Deformation Gauge

Overcoring tests, using the Bureau's three-component borehole deformation gauge, were conducted approximately 20 ft south of the center of the intersection in the roof of the entry. Nine tests were completed at approximately 1-ft intervals from 3 to 11 ft above the roofline. The 6-in-diam cores were tested at the test site in a biaxial chamber to determine the elastic constants of the roof rock in the plane perpendicular to the hole axis. The cores were tested in the laboratory to determine the elastic constants parallel to the core axis. The overcoring deformation data were analyzed using established techniques for orthotropic elastic conditions to determine the horizontal secondary principal stresses (*38*). Table 9 lists the secondary principal stresses, under plane strain conditions, at each depth tested and an average stress determined using a least-squares fitting technique (*15*).

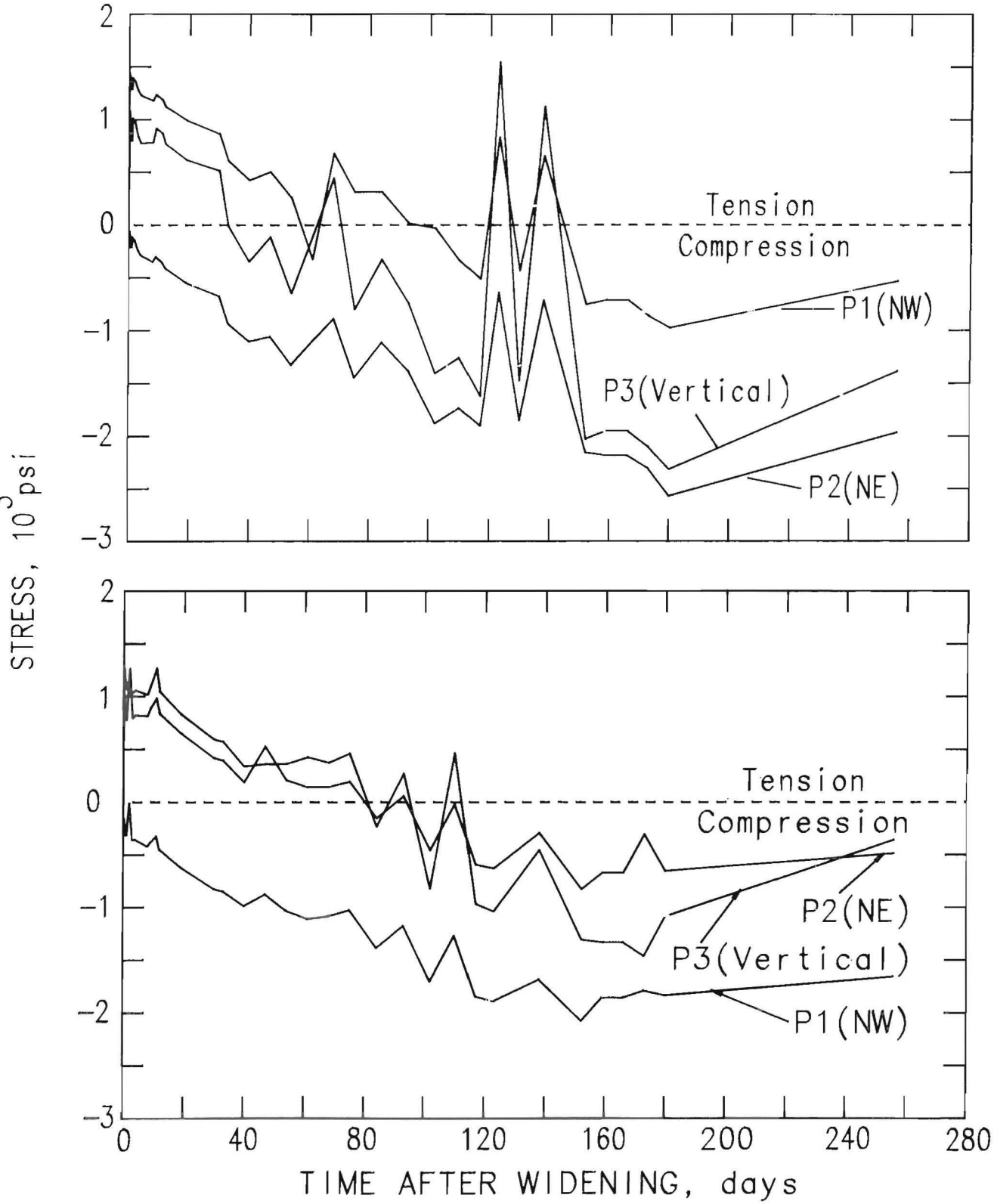

Figure 20.—Principal stresses. HISC No. 1 (top) and HISC No. 2 (bottom).

Table 9.—Secondary principal stresses in roof using Bureau's borehole deformation gauge

Test location above roofline, ft	Major stress[1]		Minor stress[1]		Av Young's modulus (E), 10^6 psi
	psi	Bearing	psi	Bearing	
3	-1,293	N 39° E	-409	N 51° W	5.52
4	-1,582	N 52° E	+24	N 38° W	9.00
5	-2,490	N 65° E	-46	N 25° W	5.46
6	-2,435	N 66° E	+458	N 24° W	6.62
7	-3,588	N 67° E	-371	N 23° W	7.37
8	-2,519	N 65° E	+85	N 25° W	5.64
9	-1,227	East	-1,041	North	1.56
10	-835	N 79° E	-518	N 11° W	1.28
11	-3,379	N 67° E	-749	N 23° W	5.70
Average[2]	-1,207	NAp	-686	NAp	NAp

NAp Not applicable.
[1]Negative values indicate compression, positive values indicate tension.
[2]Least squares average of all reliefs.

Figure 21 compares the magnitude and direction of the principal stresses with the roof lithology and the measured stiffnesses of the roof layers. The shapes of the major stress and stiffness curves suggest a possible correlation between stress and stiffness. Such a correlation should theoretically exist for the ideal condition of parallel loading of elastic layers of different stiffnesses. The analysis of BPC-CPC data also assumed a linear correlation between stress and stiffness. To evaluate the existence of this correlation, a least-squares analysis was performed for both the major and minor secondary principal stresses, and the transverse elastic moduli determined from each overcoring relief.

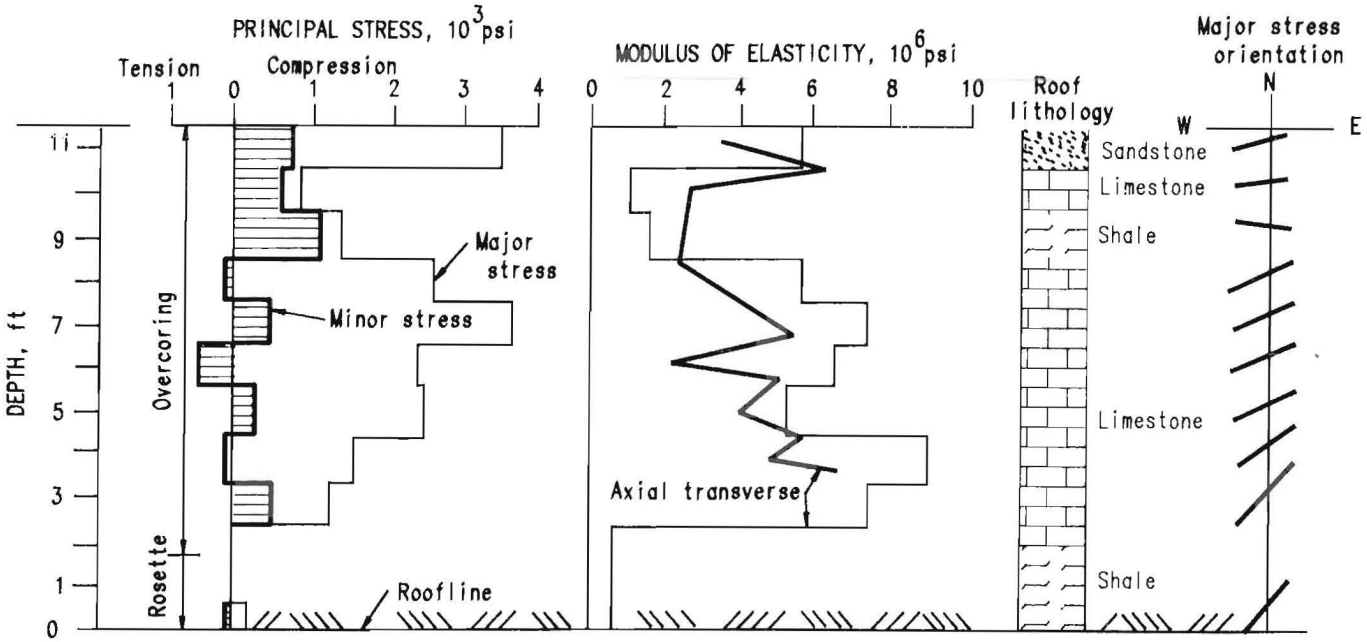

Figure 21.—Roof secondary principal stresses, modulus of elasticity, and lithology.

Figure 22 shows a plot of the principal stresses versus the elastic moduli. For the major principal stress, the data from the first two reliefs, at 3 and 4 ft, appear to be outliers and were not included in the least-squares analysis. The stresses at the lower reliefs may be influenced by stress concentrations around the entry and by roof bolting effects. The roof bolts at the overcoring site were 4 and 6 ft long and spaced approximately 2 ft from the overcoring hole. Figure 22 also shows the fitted lines for the major and minor stresses. The fitted lines have the form $y = ax$ to correspond to the theoretical relationship between stress and stiffness. The major stress data show reasonably good agreement with the theoretical curve; however, the minor stress data show little correlation with the theoretical curve. The minor stresses have relatively low magnitudes and are sometimes tensile; thus, the effect of local discontinuities and variations in rock properties may be great enough to obscure any correlation between stress and stiffness.

A linear correlation between roof stress and elastic modulus exists; however, the small number of tests and scatter of the data make the accuracy of this apparent correlation uncertain.

Undercoring

The undercoring rosette test, using the Whittemore type gauge, was conducted in the immediate roof of entry 2 about 40 ft south of the intersection. The diametral displacements resulting from undercoring are related to the secondary principal stresses in the plane of measurement (*14*).

The maximum horizontal secondary principal stress is 160 psi in compression at N 41° E, and the minimum horizontal secondary principal stress is 9 psi in tension at N 49° W.

The component horizontal stresses parallel to the entries are as follows:

Nx (north-south) = -87 psi (compressive),

Ny (east-west) = -64 psi (compressive),

and Nxy = +83 psi.

The directions of the secondary principal stresses are found to correlate closely with the direction of certain geological features in the mine. Slip zones near the test area have a bearing of N 60° E, approximately parallel to the maximum secondary principal stress. Other geologic features, including minor faults, fractures, mud slips, cleats, etc., have approximate bearings of N 55° E, N 36° E, N 45° W, and N 75° W. Figure 23 shows a close correlation between the orientation of the secondary principal stresses and coal cleats. The bearing of two distinct coal cleat planes are N 45° E and N 45° W, which compare closely with the calculated directions of horizontal stresses.

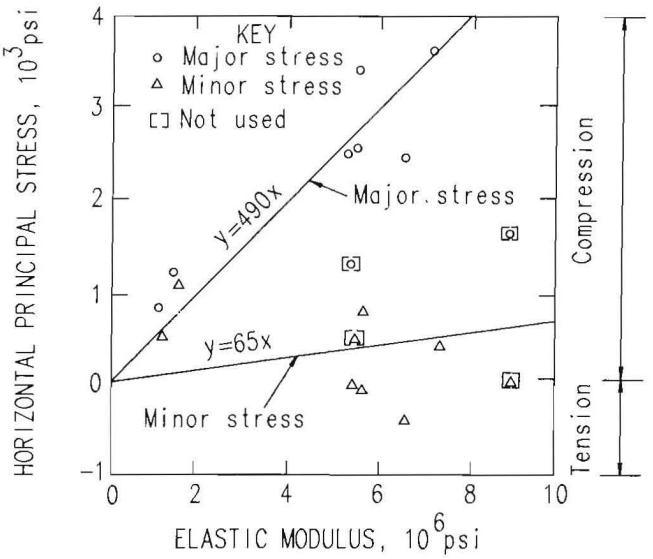

Figure 22.—Correlation of roof stress and layer stiffness.

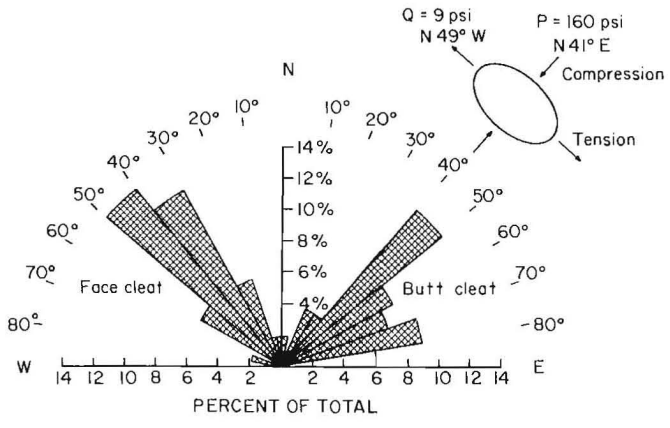

Figure 23.—Comparison between in situ stresses and cleat directions.

Discussion of Ground Pressure Analyses

To evaluate the significance of the ground pressure data analysis results, the stresses calculated using the above techniques were compared against common design theories. Additionally, in the roof, some duplication was incorporated into the instrumentation plan to permit cross-checking the results obtained from different instruments. The results of these comparisons, for pillar stresses and roof stresses, are discussed separately below.

Pillar Stresses

The average vertical stresses acting on the four instrumented pillars were calculated using the BPC-CPC results and the tributary-area method (*51*). Using the tributary-area method, the total load acting on a pillar is given by the product of the vertical overburden pressure and the sum of the pillar area plus the area extending one-half the distance into the adjacent openings. The average pillar stress is found by dividing the total load by the pillar area. The overburden pressure was estimated to be 1.1 times the depth (360 ft) or 400 psi. Average pillar stresses were calculated for the pillar and entry configurations that existed immediately before widening (premining) and those that existed after excavation of the entries was completed (postmining). The difference between these two average pillar stresses is the average stress change that occurred during widening.

Average pillar stresses and stress changes were also determined using the BPC-CPC results. Figure 16 shows the vertical stresses calculated from the BPC-CPC data and the estimated premining stresses. The stress distribution over the pillar was assumed to resemble a truncated pyramid, with zero stress at the ribs increasing to the calculated vertical stress at the shallowest BPC (5.0 or 7.5 ft on the diagonal). The distribution was assumed to vary linearly between adjacent cells and have a uniform stress over the pillar center equal to the calculated stress at the deepest cell (32.0 ft). The average pillar stress is found by dividing the volume under the assumed stress distribution by the pillar area. The postmining stress distribution was determined using the absolute stresses at each cell calculated at the end of the monitoring period after equilibrium was reached. The premining distribution was estimated by subtracting the stress changes (table 6), which were calculated using the modified inclusion method. The average stress changes were found by subtracting the average stress for the premining distribution from the average postmining stress. The average premining stress should not be considered representative of actual premining conditions and is calculated only as an intermediate step for determining the average stress change.

Table 10 shows the average pillar stresses and stress changes calculated using the tributary-area method and the BPC-CPC results. The stresses and stress changes calculated using the BPC-CPC results are significantly lower than the tributary-area predictions. The average postmining stresses using the BPC-CPC results, are approximately 60% of the stresses predicted by the tributary-area method. Similarly, the BPC-CPC stress changes are only 30% of the tributary-area estimates. To determine the reason(s) for the disagreement between the two methods, the potential effects of certain factors influencing each method were evaluated. Possible factors influencing the tributary-area results are uncertainties regarding the magnitude of the overburden pressure and the existence of a pressure arch over the test area. For agreement between the two methods, the overburden pressure would have to be 234 psi, corresponding to an average overburden specific gravity of 1.5. This low value is considered unrealistic, based on the average specific gravity, 2.6, of the roof rocks. The vertical stress on the instrumented areas of the pillars may also be reduced by the formation of a pressure arch. The existence of an arch is considered likely, since the site is situated adjacent to a barrier pillar, which may act as an abutment. The estimated width of the pressure arch (in feet) is given by (*10*):

$$W = 0.15 \times \text{depth} + 60 \qquad (4)$$

$$= 0.15 \times 360 + 60$$

$$= 114 \text{ ft.}$$

For a 114-ft-wide pressure arch with one abutment over the barrier pillar to the east of the test area, the other abutment will occur on the western portion of pillars C and D. The arch may relieve a portion of the load acting on pillars A and B and on the instrumented portion of pillars C and D. Thus, the actual stresses existing at the BPC-CPC locations may be less than those predicted using the tributary-area method.

Possible factors influencing the BPC-CPC calculations are uncertainties regarding the elastic constants of the coal and the shape of the assumed stress distribution. The equations used to determine ground stresses from cell pressures are sensitive to variations in the Poisson's ratio of the coal. Increasing the Poisson's ratio to the limiting value, 0.5, results in somewhat higher average stresses, but is insufficient to reach agreement with the tributary-area estimates. The existence of a pressure abutment near the pillar ribs, as described by the confined-core theory (*70*), is another possible explanation of the comparatively low stresses resulting from the BPC-CPC analyses.

Table 10.—Average vertical stresses for pillars A through D

	Pillar			
	A	B	C	D
Tributary area method:				
Overburden pressure ..... psi ..	400	400	400	400
Total loaded area ..... ft^2 ..	5,600	6,300	5,600	5,600
Premining pillar area ..... ft^2 ..	4,200	6,200	4,800	3,500
Postmining pillar area .... ft^2 ..	3,000	3,500	3,000	3,000
Premining pillar stress .... psi ..	533	406	467	640
Postmining pillar stress ... psi ..	747	720	747	747
Stress change ..... psi ..	214	314	280	107
BPC-CPC results:				
Premining stresses,[1] psi:				
At 5 and 7.5 ft	593	NA	531	395
At 10 and 12.5 ft	437	NA	422	478
At 20 and 22.5 ft	545	NA	456	506
At 32 ft	423	NA	498	527
Average	396	NA	359	377
Postmining stress, psi:				
At 5 and 7.5 ft	648	582	565	442
At 10 and 12.5 ft	570	357	542	535
At 20 and 22.5 ft	617	365	635	570
At 32 ft	469	667	549	574
Average	461	366	427	422
Average stress change ..... psi ..	65	NA	68	45

NA Not available.

[1]Estimated as difference between postmining stress and stress changes calculated using modified inclusion method (table 6).

The confined-core theory describes two zones within the pillar (fig. 24*A*). These two zones are the yield zone, at the pillar periphery, and the confined core, in the interior of the pillar. The vertical stress in the yield zone increases toward the pillar interior and reaches a maximum at the boundary between the yield zone and confined core given by the triaxial strength formula:

$$\sigma_m = C_o + k\sigma_3 \qquad (5)$$

where σ_m = maximum vertical stress, psi,

C_o = uniaxial strength of coal, psi,

σ_3 = horizontal confining stress, psi,

and k = triaxial stress factor.

The triaxial stress factor is related to the angle of internal friction, ϕ, by the following equation:

$$k = (1 + \sin \phi) / (1 - \sin \phi). \qquad (6)$$

The horizontal confining stress, σ_3, is assumed to increase exponentially from zero, at the rib, to a value equal to the overburden pressure at the confined core. The horizontal stress in the confined core is assumed to be equal to the overburden pressure, 400 psi; however, the average horizontal stress determined from the BPC-CPC data is only 225 psi. The confined-core theory assumes hydrostatic stress conditions in the pillar core; however, this assumption may not be valid at shallow depths. The expected horizontal stress, based on elastic theory, is equal to the product of the vertical stress and the passive pressure coefficient, $\nu/(1-\nu)$. The average pillar stress, 225 psi, is obtained using the assumed overburden pressure, 400 psi, when ν is equal to 0.36. This value, 0.36, is higher than the assumed value, 0.30, but is nearly within the range of values, 0.17 to 0.35, provided by the mine. The average measured vertical pillar stress is 560 psi, which corresponds to the average horizontal stress, 225 psi, for ν equal to 0.29. Thus, it appears that the elastic theory provides a better approximation of the horizontal stress than the assumption of hydrostatic stress conditions.

The maximum vertical stress is estimated by substituting the horizontal stress in the confined core for σ_3 in equation 5. The vertical stress is assumed to decrease exponentially from the stress peak toward the pillar interior and approach the overburden pressure asymptotically. The decay rate of the stress profile in the confined core depends on the magnitude of the load transferred from the adjacent entry. The vertical stress is assumed to increase exponentially from the uniaxial strength at the rib to the maximum stress at the yield zone-core boundary. The exponential distribution of vertical stress in both the yield zone and confined core can be approximated by linear distributions to simplify calculations. The use of a linear distribution subdivides the confined core into two secondary zones (fig. 24*A*): a tail zone adjacent to the yield zone and an undisturbed zone at the center of the pillar. The relative sizes of these two zones are determined such that the area under the linear distribution is equal to the area under the exponential distribution.

When an entry is excavated, the load initially carried by the unmined coal is transferred to the adjacent pillars (fig. 24*A*). A similar transfer of load occurs as the crosscuts are developed; however, a superposition of load occurs at the pillar corner. Since the yield zone cannot support additional load, the load transferred from the crosscut to the pillar corner must be carried by the confined core (fig. 24*B*).

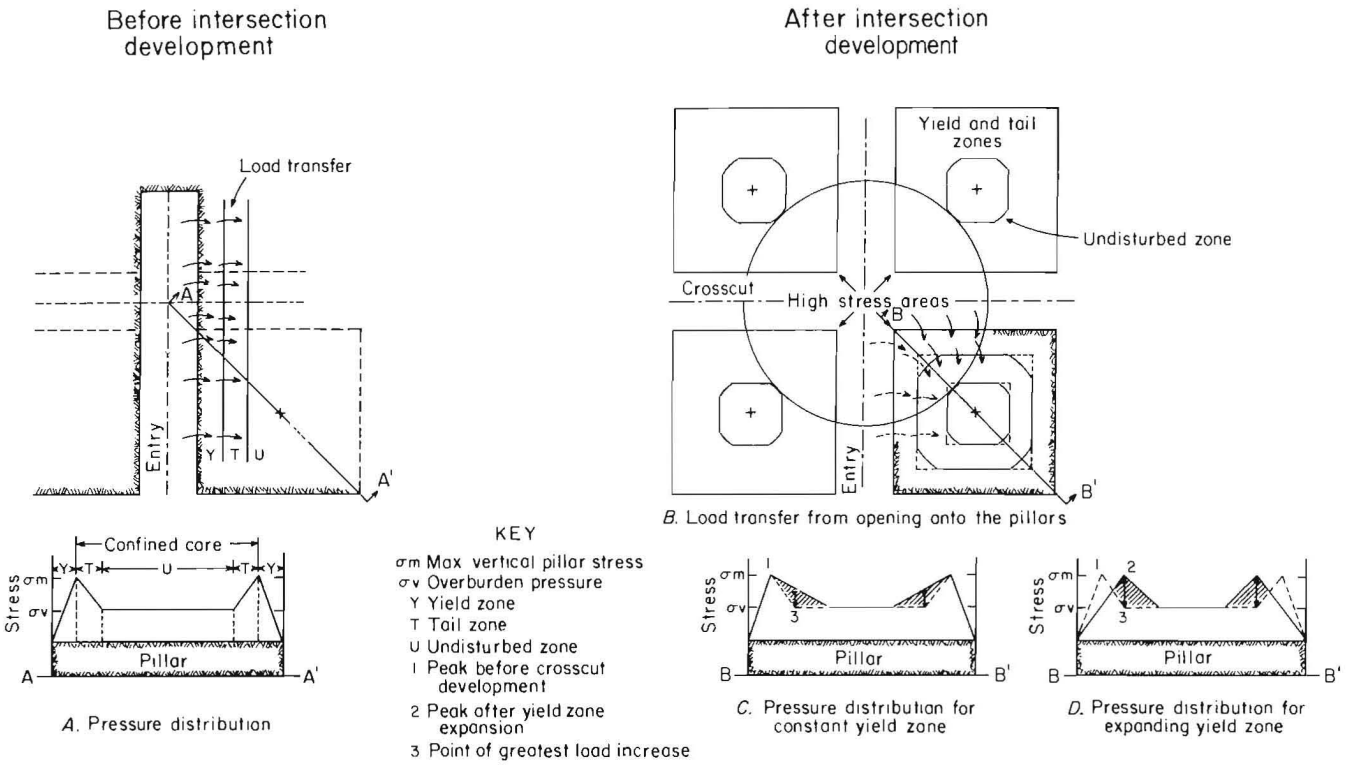

Figure 24.—Hypothetical and analytical pillar pressure distribution.

Figures 24*C* and 24*D* show possible stress distributions along a diagonal section through the pillar before and after the crosscut is mined to illustrate the expected stress transfer behavior. In figure 24*C*, the additional superimposed stresses result in an expansion of the tail zone near the pillar corner. Figure 24*D* shows an alternative distribution in which the reduced confinement on the pillar corner caused by widening results in an enlargement of the yield zone. For either case, the maximum increase in stress occurs within the confined core. The width of the yield zone is given by the following equation:

$$y = \frac{m}{\sqrt{k(k-1)}} \ln \left[\frac{C_o + k\sigma_3}{\sigma_o} \right] \qquad (7)$$

where y = width of yield zone, ft,

m = seam height, ft,

k = triaxial stress factor,

C_o = unconfined compressive strength, psi,

σ_3 = horizontal confining stress in confined core, psi,

and σ_o = unconfined strength of coal at the rib, psi.

The angle of friction for the coal is 30°, resulting in a triaxial stress factor of 3. The unconfined compressive strength of the coal is 2,900 psi, and the average confining stress, based on the BPC-CPC results, is 225 psi. A representative value for strength at the rib is more difficult to obtain. Various publications (*1, 71*) have used values ranging from 1 psi to the cohesion of the coal, approximately 840 psi. Another common approach is to reduce laboratory strength values by an adjustment factor to correspond to field conditions. Equation 7 is sensitive to the value selected for σ_o, and a wide range of values for y results, using a reasonable range of values for σ_o. Table 11 lists values of y for various values of σ_o and shows that the equation has limited usefulness for predicting the yield zone width.

Table 11.—Yield zone width (y) for different unconfined strength of coal at rib (σ_o)

	Strength reduction factor			
	1	2	3	4
Adjusted strength values:				
Unconfined compressive strength (C_o) . . . . . psi . .	2,900	1,450	580	290
Cohesion (S_o) . . . . . psi . .	840	420	168	84
Yield zone width (y) along diagonal[1], ft:				
$\sigma_o = S_o$	4.1	4.6	5.7	7.0
σ_o = 1 (70)	23.4	21.9	20.4	19.6

[1]From equation 7, with m = 7 ft, k = 3, and σ_3 = 225 psi.

The stress distributions in figure 16 show that the average postmining stress is approximately 560 psi and that the stresses are relatively uniform. It is expected that all cells were located within the confined core, thus a disagreement exists between the measured stresses, 560 psi, and the predicted core stress, 400 psi. Possible explanations of this disagreement are that the vertical stress over the measurement points is greater than the overburden pressure, or that the stresses are not transferred as expected into the tail zone, but are distributed uniformly throughout the core. Vertical stresses at the test site may have been redistributed around the slip zone, which extends through the intersection or around the sandstone channel over pillar B. This possible behavior might also explain the comparatively low stresses measured in pillar B. It is unlikely that the overburden pressure is significantly greater than expected. To generate an overburden pressure of 560 psi at a depth of 360 ft, the overburden material would be unrealistically dense, having a specific gravity of approximately 3.

A possible stress distribution, which provides agreement between the measured stresses and the tributary-area average stresses, is shown in figure 25. This distribution conforms to certain elements of the confined-core theory, but represents a substantial departure from the theory in other areas. The differences between this hybrid distribution and the distribution described by the confined-core theory are the values used for the horizontal and vertical stresses in the confined core. The vertical stress, which equals the average measured stress, is the stress required such that the areal average stress under the distribution equals the tributary-area average stress. The horizontal, confining, stress is related to the vertical stress by the passive pressure coefficient. The strength at the pillar edge is assumed to be the field value of the uniaxial compressive strength and the maximum stress is assumed to be the field value of the uniaxial compressive strength plus the product of the triaxial stress factor and the horizontal stress in the confined core.

Because of the uncertainties involved in determining the pillar stresses and specifying the yield zone parameters, particularly σ_o, the above comparison should be viewed with some skepticism. Although the hybrid distribution was made to fit the data through manipulation of certain parameters, the reverse procedure of predicting pillar loads and stress distributions is considerably more difficult and uncertain. Predictions may be possible, if sufficient field measurements are obtained to calibrate theoretical models of stress distribution and that predictions are limited to areas having similar conditions of load, geology, and geometry.

Roof Stresses

Roof stresses were determined using BPC-CPC packages, HISC, the Bureau's borehole deformation gauge, and an undercoring rosette. Measurements were obtained at various heights from 0 to 11 ft above the roofline. In addition, the changes in roof stress, which occurred while widening the intersection, were determined using the BPC-CPC packages and HISC's. Table 12 lists the component roof stresses at each height above the roofline at which measurements were obtained. Although the overcoring and undercoring techniques permit calculation of the horizontal secondary principal stresses, only the north-south and east-west component normal stresses are shown in table 12 for comparison with the BPC-CPC results.

Direct comparison of roof stresses is possible only at the level 4 ft above the roofline. Stresses at the 4-ft level were determined using the BPC-CPC packages, the HISC's, and the Bureau's gauge. The stresses calculated from the BPC-CPC data are significantly lower than those found using the other techniques. The mean of the component stresses, 1/2(Sx + Sy), was used for comparison, since this value is independent of the orientation of the principal stress axes. Table 12 also shows the mean stresses at each measurement location. The overcoring results, using both the HISC and Bureau gauges, are considered reasonably accurate owing to the calibration of both gauges against known stress conditions in the biaxial chamber. However, the BPC-CPC results were obtained using several unproven assumptions regarding rock-mass behavior, cell response, and stress distribution, and these results cannot be considered representative of actual stress conditions.

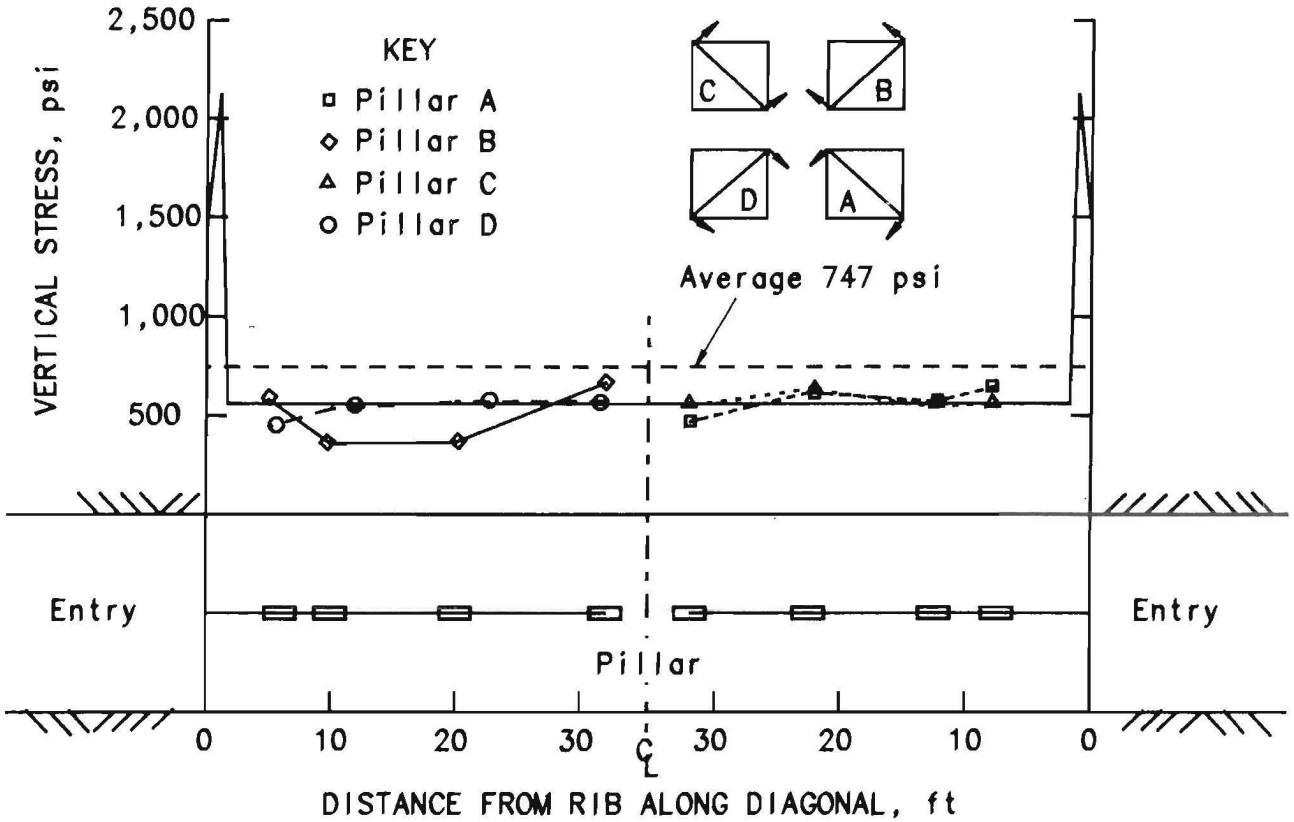

Compressive strength: Laboratory–2,900psi
Field–1,450psi

A measured core stress: Vertical–560psi
Horizontal–225psi

Strength at rib–1,450psi

Maximum stress–2,125psi

Width of yield zone–0.77ft(1.07ft diag)

Width of tail zone–0.44ft(0.62ft diag)

Figure 25.—Fitted stress distribution.

Table 12.—Horizontal roof stresses

Instrument and location	Test location above roofline, ft	Stress (S) component[1], psi		
		Sx	Sy	1/2(Sx + Sy)
Bureau deformation gauge:				
Entry	3	-759	-942	-850
	4	-973	-585	-779
	5	-2,053	-483	-1,268
	6	-1,956	-21	-988
	7	-3,097	-862	-1,980
	8	-2,054	-380	-1,217
	9	-1,227	-1,041	-1,134
	10	-823	-530	-676
	11	-2,977	-1,151	-2,064
Hollow inclusion strain cell:				
Southwest	4	-1,326	-1,174	-1,250
Center	4	-1,558	-570	-1,064
BPC-CPC package:				
Southwest	2	-92	-27	-60
	4	-579	-172	-375
Center	2	-153	-10	-82
	4	-961	-63	-512
Northeast	2	-127	-26	-76
	4	-801	-163	-482
Undercoring: Entry	0	-64	-84	-76

BPC Borehole pressure cell.
CPC Cylinder pressure cell.
x East.
y North.
[1]Negative values indicate compression.

Although the BPC-CPC stress results for the pillars appear reasonable, the analysis procedure may not apply to the roof conditions because of different rock characteristics and nonideal stress conditions. The assumptions regarding relative stress levels in different rock layers may not be valid in the interval where the cells were installed; however, this assumption primarily affects only the difference between the stress components, not the mean stress. Using the same principal stress orientation calculated using the HISC data, estimated principal stresses were calculated for the BPC-CPC data. The shapes of the resulting stress ellipses are quite different from those for the HISC and the Bureau gauge results. The shapes can be made similar by increasing the value used for the elastic modulus of shale at the lower BPC. An increased modulus effectively reduces the assumed stress ratio between the limestone and shale layers, consistent with the outlier points in figure 22 in which the stresses from the two lowest reliefs are nearly equal. The shale rock at the test site could not be tested, because of core breakage, and the value of the elastic modulus, 680,000 psi, supplied by mine personnel was based on samples taken elsewhere in the mine. To achieve similar stress ellipse shapes, the required modulus of the shale is approximately 2,000,000 psi. This value is consistent with the values for other shales, suggesting that the shale layer may be stiffer than originally assumed. Although a possibly incorrect value of the elastic modulus might explain variations in the shape of the stress ellipse, it cannot account for the low mean stress values. The calculated value of the mean stress is dependent primarily upon the assumed relation between the CPC pressure, the Poisson's ratio, and the sum of the biaxial ground stresses. Since the CPC pressure and Poisson's ratio are known with relatively high certainty, it is evident that the defining equation for the sum of the biaxial stresses does not apply to the assumed conditions in the roof at the time of measurement. A possible reason for the disagreement between CPC pressure and mean stress is that the stress levels in the roof rock are too low to induce the assumed viscoelastic behavior within the 6-month period during which measurements were collected.

Comparison of the stress changes accompanying development determined from the BPC-CPC packages and HISC's produces similar inconsistencies. Table 13 shows the calculated and mean stress changes 4 ft above the roofline. The stress changes calculated from the BPC-CPC data are lower than those found using the HISC's. The stress changes calculated using the pressure convergence method (*45*) are also lower than those which result from the Babcock method (*4*).

Table 13.—Comparison of roof stress changes

Instrument and location	Method[1]	Stress (s) component[2], psi		
		ΔSx	ΔSy	1/2(ΔSx + ΔSy)
BPC-CPC package:				
Southwest	1	-141	14	-64
Center	1	1	-4	-2
Northeast	1	-13	6	-4
BPC-CPC package:				
Southwest	2	-1,158	-333	-746
Center	2	50	-149	-100
Northeast	2	-67	103	18
HISC:				
Southwest	NAp	-331	-334	-333
Center	NAp	-317	-315	-316

NAp Not applicable.
[1]1, = pressure convergence method (*45*); 2, = Babcock method (*4*).
[2]Negative values indicate reduction in compressive stress.

STRATA MOVEMENTS

Roof bolt loads, roof strata displacement and bed separations, and roof-to-floor closure were monitored to evaluate both short-term and long-term failure behavior.

Roof Bolt Loading

The analysis of roof bolt loads was concerned primarily with the change in loads that occurred as the intersection was widened and the total load change that occurred over the long-term monitoring period. In addition, the distribution of the load changes was considered more informative than the magnitudes of the changes.

The field data were reduced using a linear equation obtained by calibrating the measuring rings in the laboratory. Data obtained from the pad manufacturer (*21*) indicated that a relaxation of the pads may occur resulting in a reduction of load for a constant ring reading. The expected load reduction is 15% of the initial load after 35 days and 20% after 1,000 days of installation. Since the pads were installed at approximately the same time, any relaxation behavior should affect all pads equally. Thus, trends in the distribution of bolt load changes should be unaffected by any uncertainty in the absolute bolt load.

Three types of loading behavior were observed. The most common behavior consisted of a sharp increase in load immediately after development with no further changes during the monitoring period. Other bolts indicated a similar sharp load increase after development, but a continuing increase or decrease thereafter. The third type of behavior consisted of a sharp decrease in load corresponding to a small roof fall adjacent to the bolt.

Contour plots of the corrected load changes for each monitoring interval were prepared and are shown in figure 26. The figure indicates a large load change at the center of the intersection and near pillar D in the entry. The shape of the load-change distributions remained relatively constant throughout the monitoring period; however, the magnitude of the changes generally increased. The load-change contours within the intersection are approximately aligned with the direction of the minor horizontal principal stress, suggesting that the bolt loads are influenced by the in situ stresses. The decrease in loads near pillar B corresponds to several small roof falls that occurred along the slip zone.

An analysis was performed to determine the maximum dead load on the bolts using the maximum thickness of a detached roof layer and the bolt spacing. The maximum roof thickness is 4 ft (length of bolts) and the bolt spacing about 4 by 4 ft. For a limestone density of 168 lb/ft^3, the maximum dead load is 168 $(4)^3$ = 10,752 lb. In the intact roof areas, where bolt loads increased, the measured bolt loads range from 11,300 to 21,600 lb. The observed roof separations indicate that the actual dead load on the bolts will be much less than the maximum load calculated above because the dead load will be calculated for a thinner layer. Furthermore, the bolt loads were increasing during the monitoring period, indicating that in addition to dead load, some other action, such as buckling or shearing, is responsible for bolt loading.

An additional analysis was performed, attempting to establish a relationship between torque and bolt load. Virtually no correlation is exhibited by the data; however, a linear regression analysis forced through the origin results in the equation: load (pound) = 54 × torque (foot pound).

Roof Strata Displacement and Bed Separation

The field data consisted of measurements of the distance between the sleeves clamped on each wire to the reference cap anchored at the roof surface. Analysis of the data was based on the assumption that the top anchor remains in a fixed position over time. Movements of the other anchors, including the roof surface, were calculated

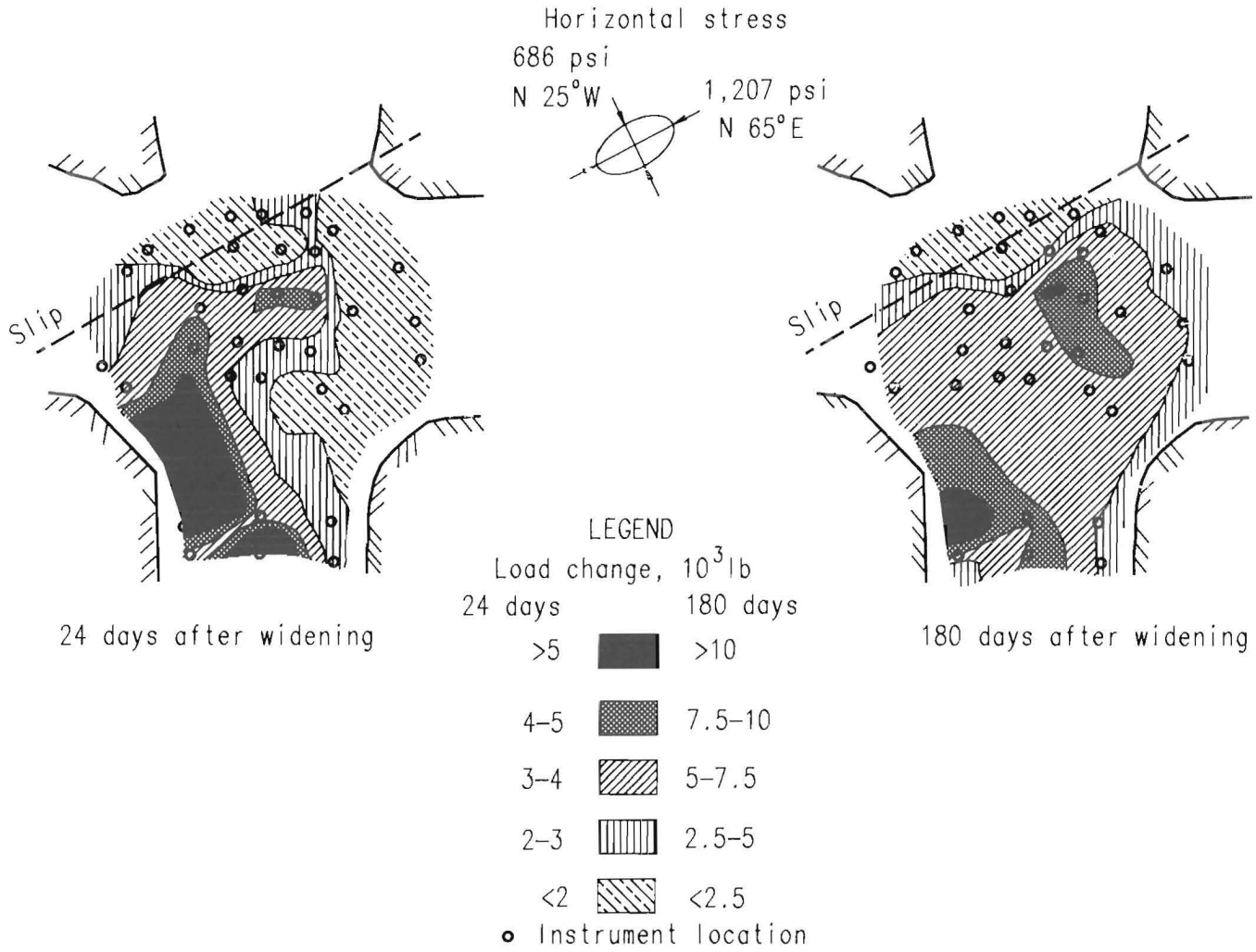

Figure 26.—Roof bolt load changes.

relative to the position of the top anchor. At each station, the data were used to calculate the downward movement of each anchor and the change in distance between anchors. The change in distance between anchors corresponds to the opening and closing of bed separations that occur between the anchors.

Because of a high corrosion rate, most of the anchor wires broke before the end of the monitoring period. Since all anchor movements are based on the data from the top anchor, analysis was restricted to the data obtained through 12 days after widening, when the top anchors for all stations were still intact.

Figure 27 shows plots of the downward movements of each anchor for the 13 extensometer stations. Some curves do not extend completely across the charts due to the loss of data resulting from wire breakage. Some of the curves show apparent upward movements. Upward movement of the roof layers may be possible; however, these upward movements are thought to result from downward movement of the top anchor. Minor upward fluctuations are likely caused by normal measurement error and may not represent actual movements.

Nearly all extensometer stations indicated a major separation between the roof surface and the first anchor at a depth of 1.5 ft. A few stations show an increased separation between anchor 1 and anchor 2 at a depth of 2.7 ft. Station X-1 also shows a separation between anchor 2 and anchor 3 at a depth of 4.5 ft. In addition, station X-12 shows a sudden large separation between anchor 3 and anchor 4 (8.5 ft) at the end of the monitoring period.

Figure 27 indicates that the roof deflections were highest near the center of the intersection and averaged 0.076 in. However, significantly larger deflections were

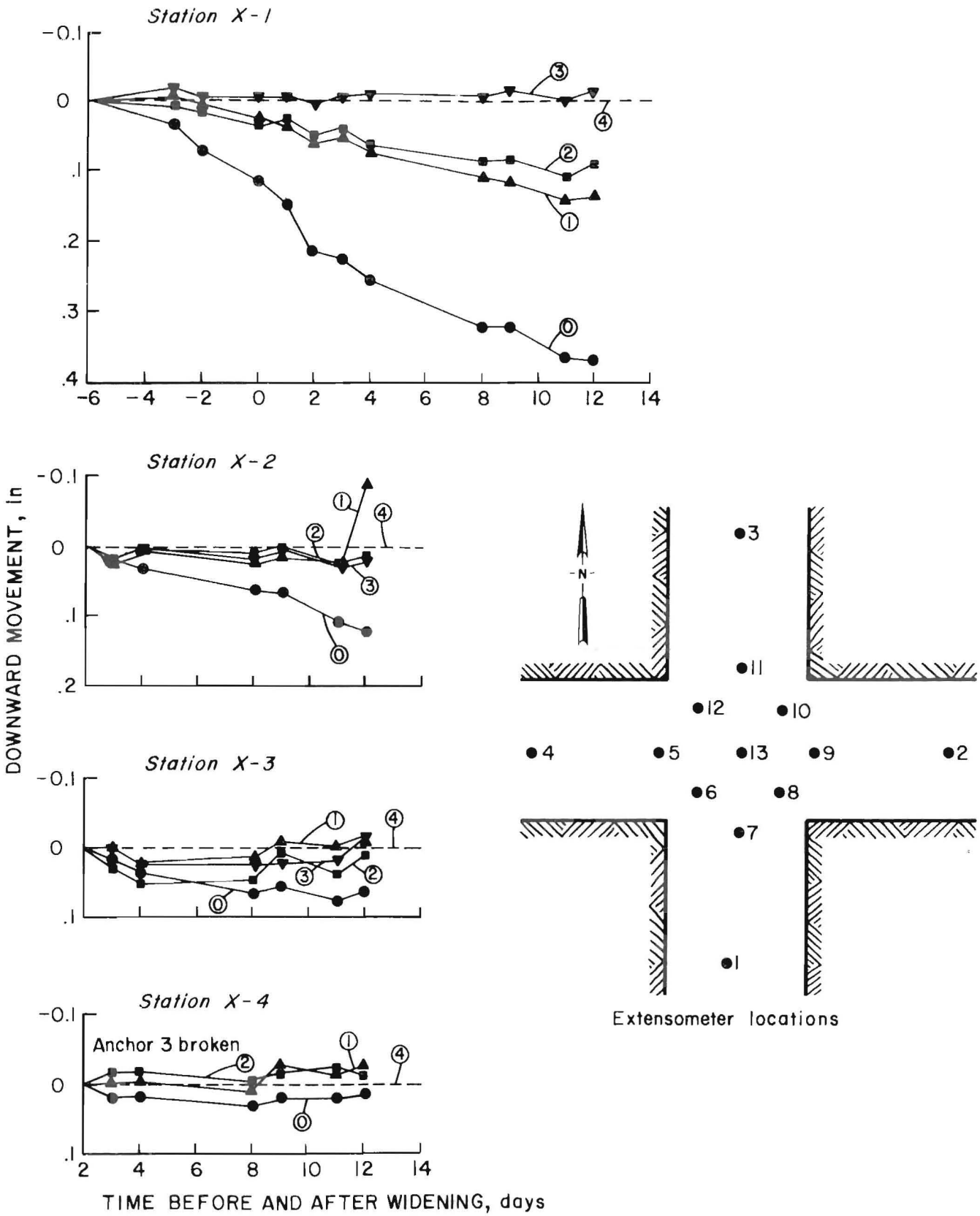

Figure 27.—Cumulative roof-strata movements.

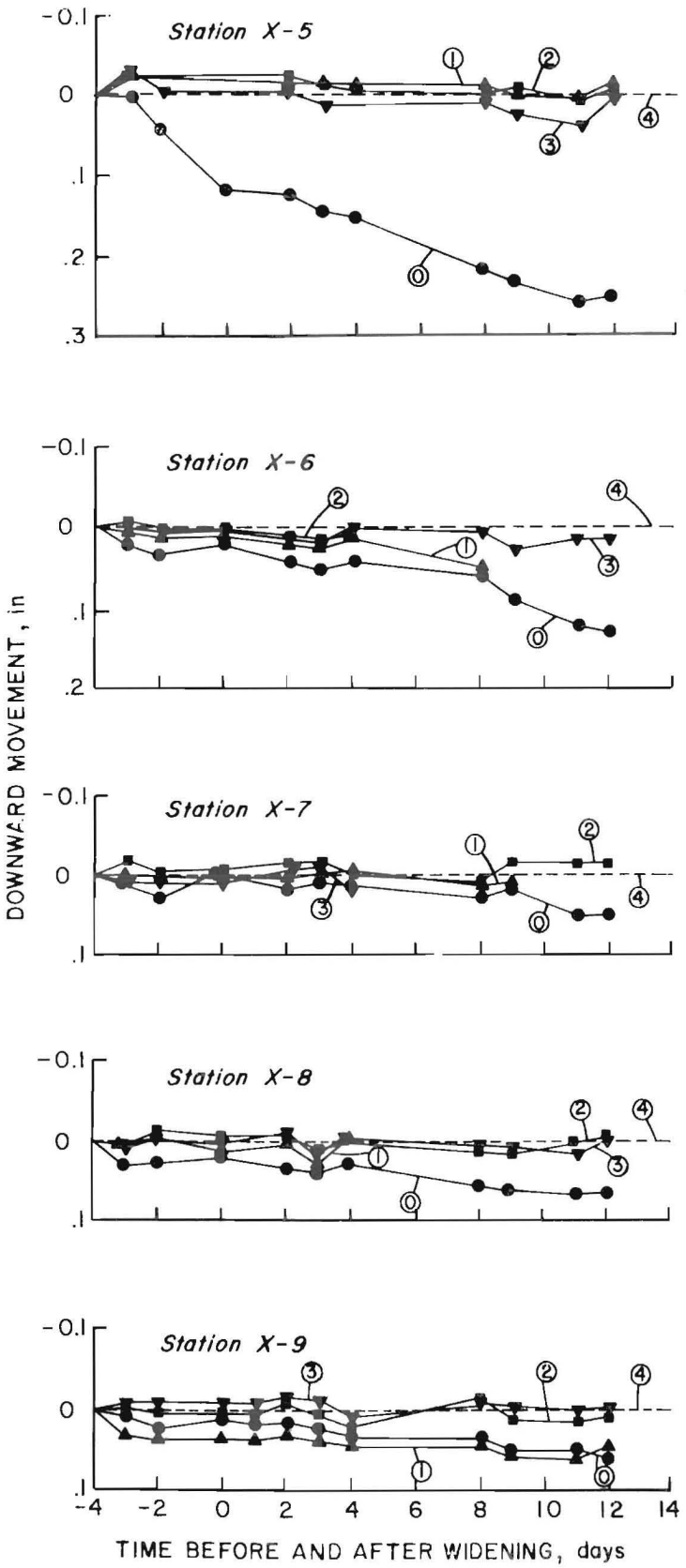

Figure 27.—Cumulative roof-strata movements—Continued.

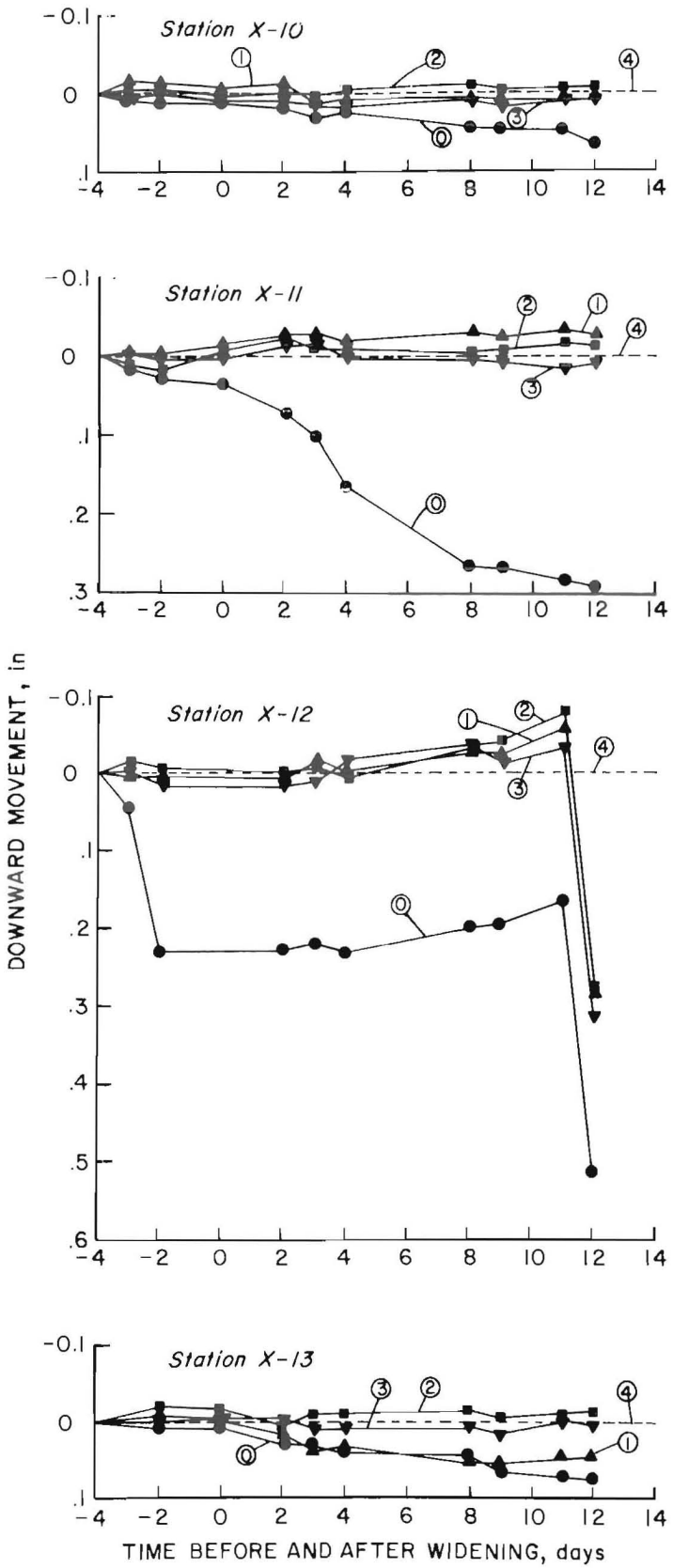

Figure 27.—Cumulative roof-strata movements—Continued.

measured near slip planes as shown in figure 28. Roof deflections at slip zones were approximately seven times greater than deflections measured in intact roof areas.

In general, intersection widening had almost no effect on measured roof strata movements. However, stations X-6 and X-13 (fig. 27) show a small increase in sag during mining, and stations X-1 and X-11 show an increased sag rate after mining was completed. These changes are small, however, and may not be significantly different from those expected for normal measurement variations.

The measured roof deflections are significantly greater than those predicted by elastic theory. Some of the larger measured deflections may be attributed to local movement along slip surfaces; however, the discrepancy still exists for those measurements taken in intact areas of the roof.

Elastic deflections were calculated for three behavior models: a square plate clamped on all sides, a continuous plate supported on equally spaced posts, and a clamped-end beam extending diagonally across the intersection. The plate (beam) was assumed to be 4 ft thick, corresponding to the 4-ft length of the rock bolts clamping the roof layers together. The deflections were calculated using the following formula (*51, 55, 65*):

$$n = \frac{a\gamma L^4}{12Et^2} \qquad (8)$$

where n = roof deflection at center of intersection, in,

a = constant depending upon model,

γ = specific weight of rock, 168 lb/ft^3,

L = room width, 20 ft,

E = Young's modulus, 0.68×10^6 psi,

and t = roof thickness, 4 ft.

The values of a and the resulting deflections for each model type are

	a	n, in
clamped-edge plate	0.0138	0.003
continuous plate	0.0634	0.013
clamped-end beam	0.1250	0.026

In comparison, the measured deflections at stations X-6 through X-10 and X-13 averaged 0.076 in. In addition, total deflection will be greater than the measured deflection because the extensometers were installed about 7 days after the intersection was mined. The discrepancy between the calculated and measured deflections may be attributed to the following factors:

- Horizontal stresses may impart an additional bending moment in the roof (column buckling).
- The measured deflections may be the result of inelastic creep.
- The roof may not behave as a 4-ft-thick unit, and deflections should be calculated for a thinner member.
- The in situ value of Young's modulus may be lower than that used for calculating the elastic deflection.

An estimate of the potential deflection caused by horizontal stresses was determined using the secant formula (*33*) for a clamped-end column:

$$n = e\left[\text{secant}\left(L\sqrt{72P/EI}\right) - 1\right] \qquad (9)$$

where n = roof deflection at center of beam, in,

P = load on ends, 160 psi $\times$ 48 in $\times$ 12 in = 92,160 lb,

I = moment of inertia, 110,600 in^4,

and e = eccentricity of load, 2.0 in.

The resulting deflection caused by buckling is 0.036 in; therefore, the horizontal stresses may cause significant roof movement.

The possibility of creep is indicated by the roughly logarithmic decrease in roof deflection. This behavior suggests that the roof is undergoing the secondary creep stage, which follows the initial elastic deflection.

The roof bolt data show an increase in loads, indicating that the roof layers should be clamped together; however, the extensometer data show that separations between roof layers are occurring throughout the intersection. If the roof layers are indeed separating, the elastic deflection of a thinner layer will more closely approximate the observed roof deflection. For example, the elastic deflection of a 10-in-thick clamped plate is 0.066 in—nearly equal to the average deflection shown by the extensometers placed in the intact roof.

A smaller value of Young's modulus will also increase the elastic deflection, although this factor cannot account entirely for the discrepancy between measured and calculated deflections. It is likely that the in situ modulus is lower than the value determined by laboratory tests because of fractures, bedding planes, moisture, etc.

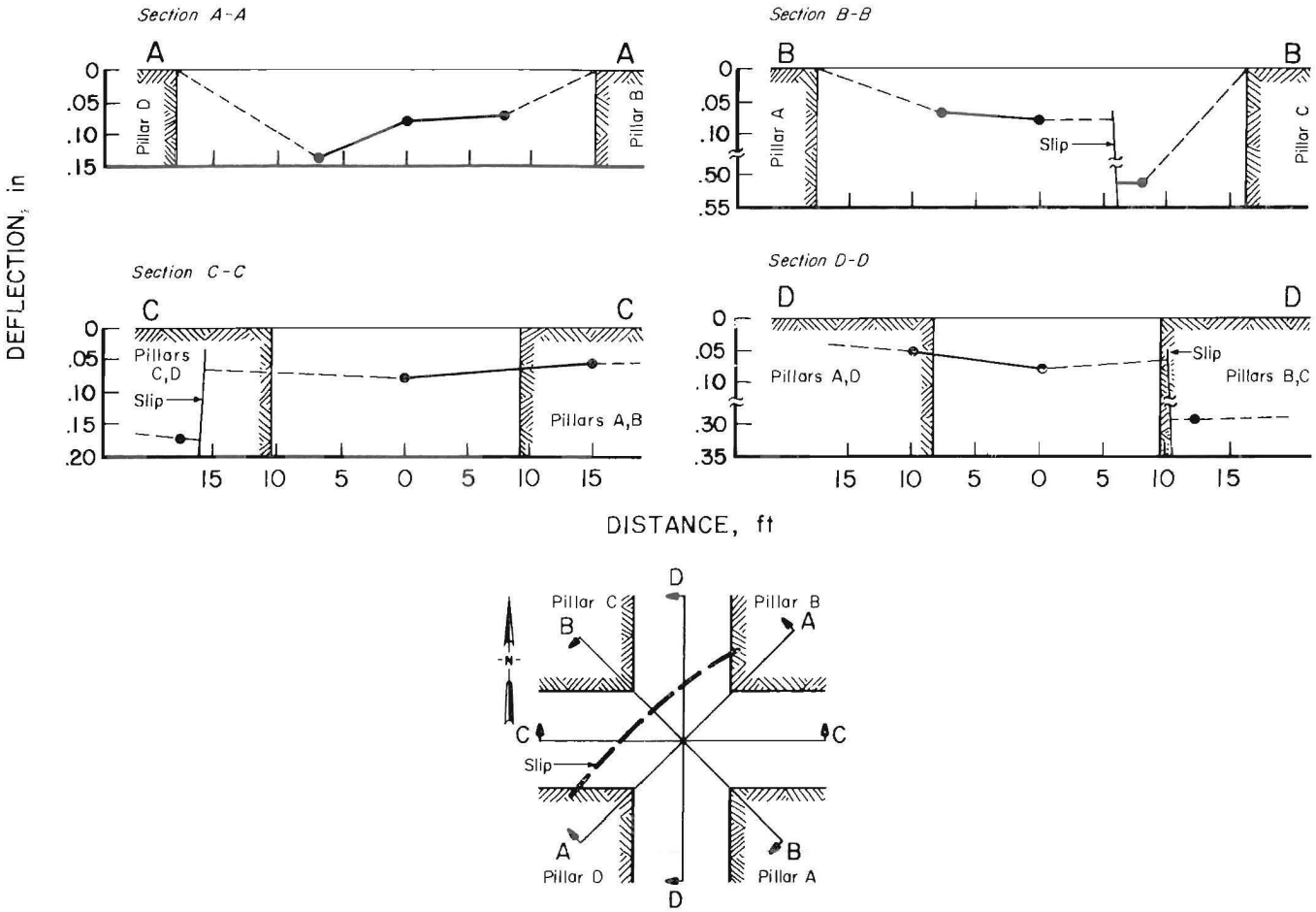

Figure 28.—Roof deflection along slip zone.

Roof-to-Floor Closure

Ten convergence stations were installed before widening to measure the roof-to-floor closure caused by mining. Figure 29 shows a typical plot of closure versus time and indicates that the shapes of the closure curves are approximately logarithmic. Except for obvious fluctuations caused by mining interference, the slope of the curve during widening remained relatively constant Therefore, the initial disturbed portion of the curve was replaced by a straight line matching the slope of the convergence curve at the time the area was barricaded, 6 days after widening, when mining interference ceased. The slope of the line represents an average convergence rate, which was used to estimate the total convergence that occurred from the time the opening was mined until the end of the initial monitoring period, approximately 6 days after the access to the area was restricted. The total convergence was calculated by adding the long-term convergence, which occurred after the initial monitoring period, to the estimated initial convergence. Figure 30 shows a composite contour diagram

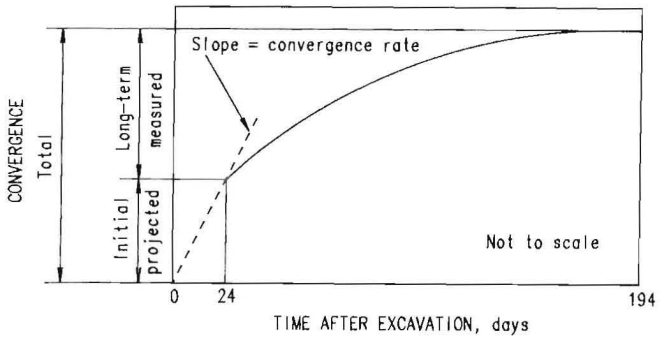

Figure 29.—Roof-to-floor convergence.

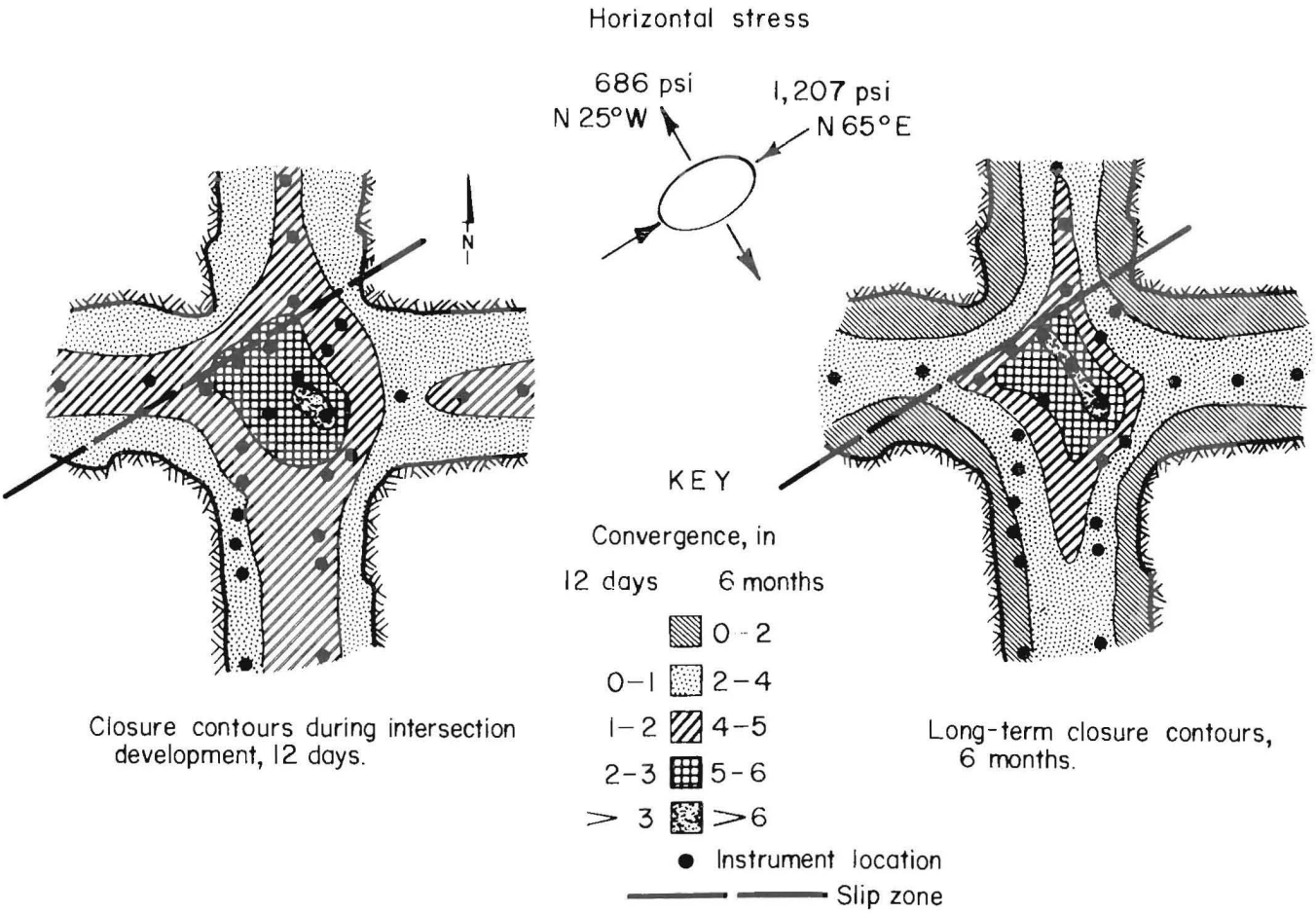

Figure 30.—Composite room closure contours.

of the estimated initial convergence at the end of the initial monitoring period. A maximum convergence of about 3.4 in occurs near the center of the intersection and a maximum of 1.5 in occurs in the center of the entries. Minimal closure is observed near the ribs indicating that pillar punching is not a significant factor. Figure 30 also shows contours of the total convergence at the end of the 6-month monitoring period. The maximum convergence in the center of the intersection is approximately 6.6 in, and the maximum in the center of the entries is about 4.5 in. The maximum closure is approximately 40 times greater than the roof sag, indicating that room closure is predominantly caused by floor heave.

The directional trend of the closure contours in figure 30 is approximately aligned with the directions of the horizontal secondary principal stresses. The shape of the closure contours suggests that the horizontal stresses are acting to deform the floor layer(s) by a bending or buckling mechanism.

A possible floor heave mechanism is that of strain relief associated with the horizontal stress field (*3*). This behavior is visualized by considering the floor layer as an elastic member, or spring, being compressed by the horizontal stresses. As the layer deforms or buckles into the opening, the length of the member increases resulting in a corresponding decrease of strain. The initial strain in the layer is equal to the maximum horizontal stress divided by the elastic modulus. The required increase in length of the floor member to achieve full strain relief is the product of the initial strain times the initial length of the member, or the room width. The maximum vertical deflection of the floor layer (maximum heave) depends on the shape of the deformed layer. Figure 31 shows a simplified floor heave model in which the shape of the deformed layer is approximated by a triangle. Since the stresses in the floor and the elastic modulus of the floor layer are unknown, the use of a more sophisticated model was considered inappropriate.

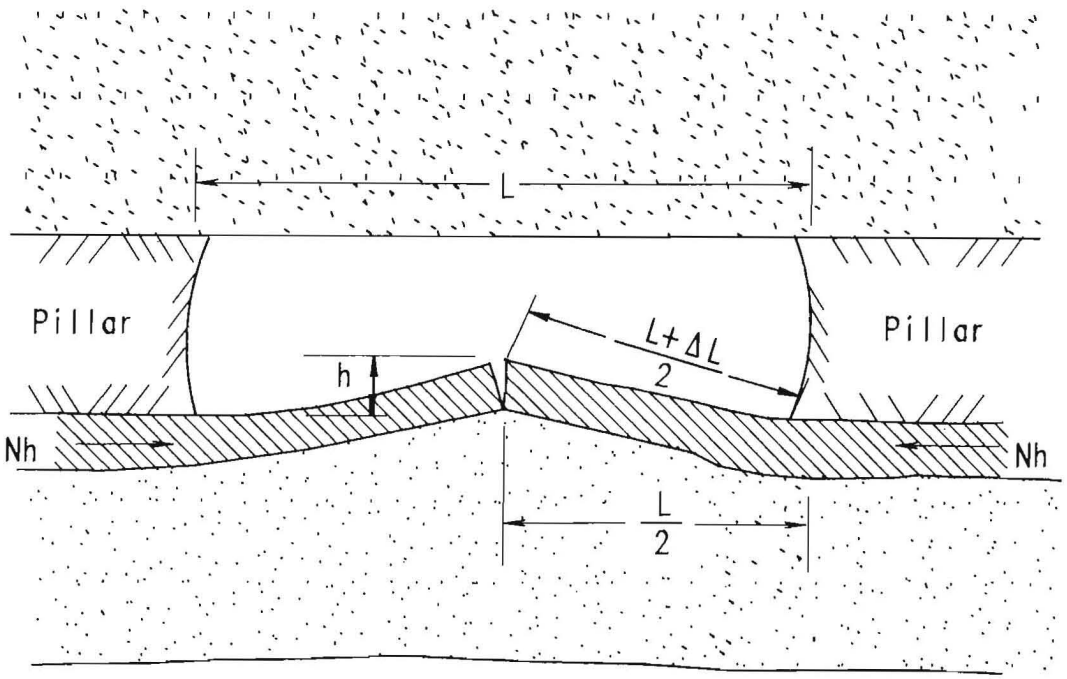

KEY

L Room width, in
ΔL Change in length of floor member, in
Nh Horizontal stress in floor member, psi
h Floor heave, in

Figure 31.—Floor heave model.

The change in length of the floor member to achieve full strain relief is given by the following equation:

$$\Delta L = \frac{NhL}{E} \quad (10)$$

where ΔL = change in length of floor member, in,

Nh = horizontal stress in member, psi,

L = room width, in,

and E = Young's modulus of floor member, psi.

The magnitude of the floor heave, using the simple model shown in figure 31, is given by

$$h^2 = \Delta L(2L + \Delta L)/4 \quad (11)$$

where h = floor heave, in.

The floor heave, h, was estimated to be equal to the maximum long-term closure, 6.6 in. The room width, L, was 240 in, and the horizontal stress, Nh, was estimated to be 1,207 psi from table 9. Substituting these values into equations 10 and 11 results in a value of 800,000 psi for the elastic modulus. This value is reasonable for the floor material, mudstone, indicating that strain relief may be a significant factor affecting floor heave.

SUMMARY AND CONCLUSIONS

The conclusions of this investigation can be grouped into two categories: design methods and field results. These categories are discussed.

DESIGN METHODS

Current design methods for determining roof and pillar dimensions rely on estimates of mining-induced stresses and rock mass strength and use safety factors based on experience. Stresses are estimated using theoretical equations, numerical modeling results, or empirical formulas. The beam and plate theories are commonly applied to the roof of entries and intersections, respectively. For pillars, the tributary-area method is typically employed, although more detailed approaches, such as the confined-core theory, are often considered.

Determination of rock and coal strengths is most commonly accomplished through laboratory testing of small samples. Many pillar-strength equations exist to scale laboratory tested strengths to field conditions. Such equations should be examined carefully to ensure that they provide reasonable results at extreme pillar sizes and that they correctly describe the nonlinear relationship between pillar strength and pillar width. In addition, most methods for determining rock and coal strength do not consider the effects of geologic discontinuities, such as joints and fractures, or environmental effects, such as groundwater and weathering.

Specification of roof support is generally based on either suspension or beam-building models of roof behavior. Support plans in intersections commonly specify additional or longer bolts. Applications using truss bolts are also common to maintain a roof arch across the intersection. The use of additional longer bolts at pillar corners appears advantageous, particularly when the pillar corners are rounded during development.

FIELD RESULTS

Analysis of the field observations and measurements provided results concerning both the structural behavior of the instrumented intersection and the performance of the various instruments that were installed.

Observed Intersection Behavior

The major instability in the roof was the result of movement along slips in a narrow zone extending diagonally across the intersection. The downthrown sections of the roof experienced minor roof falls between bolts and a loss of bolt tension. The slip zone was oriented perpendicular to the minor horizontal principal stress. The deflection of the upthrown, or intact, area of the intersection roof was consistent with the deflections predicted by the plate theory. The extensometer data indicated that separations occurred between roof layers presumably clamped by the roof bolts. In addition, the bolt loads were greater than those which would be expected by suspension loading. Therefore, it is believed that the horizontal stresses caused the roof to buckle, thereby increasing the bed separation and bolt loads. A similar strain-relief or buckling mechanism was observed in the floor. Contours of the roof bolt loads and room closure show directional trends which are aligned with the horizontal principal stresses. Thus, the in situ stresses appear to influence significantly the deformation behavior of the roof and floor.

The measured directions of the horizontal principal stresses agreed with the directions of several geological discontinuities including slips, joints, mud dikes, and coal cleats. The stresses were also aligned with several large-scale zones of instability, possibly faults, which occurred throughout the mine. The magnitude of the major principal stress is linearly related to the elastic modulus of the roof rock in the region above the roof bolted interval. The direction of the stresses varied considerably within the intersection, possibly due to slippage between roof layers or to the influence of a small roof fall.

The average pillar stresses calculated using hydraulic borehole pressure cell data are lower than the average stress predicted by the tributary-area theory. The distribution of stress does not indicate the presence of a stress abutment near the pillar rib and is greater than the expected overburden load in the pillar core. This disagreement with the tributary area and confined core theories may be explained by a large, narrow abutment near the rib, which was not detected by the pressure cells, or by an arch which formed over the test area. Similar inconsistencies accompanied the roof stress measurements. The general performance of all instruments will be addressed in the following section.

Instrument Performance

The theory of operation, installation procedure, and data analysis methods for each of the instruments has been discussed in previous sections and in appendix B. This section will summarize the performance of each instrument.

- Borehole Shear Tester—Although the data were consistent, the predicted strengths were unreasonable. A malfunctioning instrument or poor hole conditions may be the cause of the low cohesion values.
- Roof Bolt Compression Pads—Some uncertainty exists regarding the relaxation behavior claimed by the manufacturer, particularly under varying loads. However, the pads performed well for qualitative comparisons between bolts.
- Borehole Extensometers—Except a corrosion problem, the extensometers performed exceptionally well. The components of the instruments are inexpensive and simple to install yet yield repeatable measurements to within a few thousandths of an inch. Corrosion of the wires can most likely be controlled by using stainless steel or coated wire.
- Closure Meter—The closure meter performed well; however, the floor reference stations were easily disturbed by the passage of mining equipment. Below-grade installation or protective caps could eliminate the problem.
- Undercoring—The undercoring test was satisfactory; however, considerable effort is involved, and the results are of limited value. For moderate additional effort, overcoring could be performed to determine stresses outside the influence of the opening.
- Overcoring—The Bureau's three-component deformation gauge worked well; however, data could not be obtained from the floor. The 6-in-diam overcoring bit became stuck in a clay layer in the immediate floor. The stress results in the roof were inconsistent in the 4-ft interval that was bolted. This inconsistence may be the result of stress concentrations around the opening or by an arching effect induced by the roof bolts.

The HISC instruments performed reasonably well and produced stress results that were consistent with the other overcoring results. The cells offer the advantage of allowing determination of the three-dimensional stress field from a single overcore; however, the instruments are not recoverable. The measured variation of stress orientation in the intersection may be the result of bolting effects, roof layer shifting, or nearby roof falls. The instruments were sensitive to the condition of the battery used in the readout device. For long-term monitoring applications, the battery condition should be monitored, a dummy gauge should be used for calibration, or a more reliable power source should be substituted.

- Pressure Cells—The hydraulic borehole pressure cells (BPC's and CPC's) produced consistent pressure data; however, stresses calculated from the data do not agree with the results obtained from other methods such as the tributary area and confined-core methods. The equations used to determine ground stresses from cell pressures were found to be inadequate for installations involving varied rock types and nonuniform stress fields. In addition, the cell configuration provided information only on the normal stress components aligned with the cell measurement directions and did not permit determination of the principal stresses. Modified equations and techniques were developed to overcome these inadequacies.

The calculated pillar stresses were lower than those predicted using the tributary-area theory, but greater than those expected in the pillar core using the confined-core theory. The data did not indicate the presence of a stress abutment or a yielded zone at the pillar rib; however, the coarse spacing of the cells did not permit monitoring the behavior within 5 ft of the rib. The horizontal stress in the pillars corresponded to the passive pressure induced by overburden loading and was not equal to the vertical stress (hydrostatic) as assumed by the confined-core theory. A possible stress distribution, having a narrow abutment at the pillar rib and passive stresses in the pillar core, was developed to match the data. However, it is likely that the

pillar stresses were influenced by a possible ground arch and that the tributary-area theory does not apply. Because no instruments were installed to verify the pressure-cell results, it was difficult to determine whether the inconsistencies of the measured stresses were the result of anomalous ground conditions, or incorrect measurement technique. However, rough sensitivity analyses indicate that the calculated stresses are essentially correct, and that some other factor, or combination of factors, is responsible for the disagreement between measured and predicted stresses.

To minimize the number of instruments installed, only one horizontally oriented cell was installed in each pillar. This procedure required certain assumptions regarding the distribution of horizontal stress within the pillar. The analyses assumed the horizontal stress was uniform; however, calculations were repeated with various nonuniform distributions. The resulting vertical stresses varied less than 10%, indicating that the shape of the horizontal stress distribution is relatively unimportant.

In the roof, the horizontal stresses determined from the pressure-cell data were significantly lower than those determined from overcoring. Since the overcoring results were essentially verified by biaxial tests at known applied stresses, they are assumed to be correct. It is believed that the low stresses determined from the BPC's-CPC's are the result of incomplete adjustment of the cells in reaching equilibrium. The assumed viscoelastic behavior of the rock may not have been fully realized within the 6-month monitoring period. The modified equations, which account for cell installation in varying rock types, show that the calculated stresses are sensitive to the respective response factors of different rock types and the variation of stresses between cells. Stress changes were calculated using the pressure convergence method developed by Lu (*45*) and the stress change method developed by Babcock and produced widely varying results.

REFERENCES

1. Abel, J. F., and W. N. Hoskins. Confined Core Pillar Design for Colorado Oil Shale. Ninth Oil Shale Symp., CO Sch. Mines, May 1976, 26 pp.

2. Adler, L., and M. C. Sun. Ground Control in Bedded Formations. VA Polytech. Inst. State Univ., Bull. 28, Res. Div., Reprint Mar. 1976, pp. 42-49.

3. Aggson, J. R. Coal Mine Floor Heave in the Beckley Coalbed, An Analysis. BuMines RI 8274, 1978, 32 pp.

4. Babcock, C. O. Equations for the Analysis of Borehole Pressure Cell Data. Paper in Proceedings of the 27th U.S. Rock Mechanics Symposium, Univ. AL, Tuscaloosa, AL, June 1986, 8 pp.

5. ____. Effect of End Constraint on the Compressive Strength of Model Rock Pillars. SME/AIME Trans. v. 244, 1969, pp. 357-364.

6. Bickel, D. L. Overcoring Equipment and Techniques Used in Rock Stress Determination (An Update of IC 8618). BuMines IC 9013, 1985, 27 pp.

7. Bieniawski, Z. T. In Situ Strength and Deformation Characteristics of Coal. Eng. Geol., v. 2, 1968, pp. 325-340.

8. ____. In Situ Large-Scale Testing of Coal. Paper in Proceedings of Conference on In Situ Investigation on Solids and Rock. Br. Geotech. Soc., 1969, pp. 67-74.

9. Bryan, A., J. G. Bryan, and J. Fouche. Some Problems of Strata Control and Support in Pillar Workings. Min. Eng., v. 123, 1963, pp. 238-266.

10. Bunting, D. Chamber Pillars in Deep Anthracite Mines. Trans. AIME v. 42, 1911, pp. 236-245.

11. Campbell, J. L., L. J. Pelrovic, W. J. Mallio, and C. W. Schulties. How to Predict Coal Mine Roof Conditions Before Mining. Min. Eng., Oct. 1975, p. 37.

12. Damberger, H. H., and other members. Illinois. Paper in 1983 Keystone Coal Industry Manual, ed. by G. F. Nielson. McGraw-Hill, 1983, pp. 526-537.

13. Damberger, H. H., M. E. Hopkins, H. F. Krausse, and W. J. Nelson. Engineering Study of Structural Geologic Features of the Herrin (No. 6) Coal and Associated Rocks in Illinois (contract H0242017, IL State Geol. Surv.). Volume 1—Summary Report. BuMines OFR 96(1)-80, 1979, 67 pp.; NTIS PB 80-219454; Volume 2—Detailed Report. BuMines OFR 96(2)-80, 1979, 218 pp.; NTIS PB 80-219462.

14. Duvall, W. I. Stress Relief by Center Hole. Appendix in Improvements in the Three-Component Borehole Deformation Gage and Overcoring Techniques, by V. E. Hooker, J. R. Aggson, and D. L. Bickel. BuMines RI 7894, 1974, 29 pp.

15. Duvall, W. I., and J. R. Aggson. Least Squares Calculation of Horizontal Stresses From More Than Three Diametral Deformations in Vertical Boreholes. BuMines RI 8414, 1980, 12 pp.

16. Ealy, D. L., R. E. Mazuark, and E. L. Langrand. A Geological Approach for Predicting Unstable Roof and Floor Conditions in Advance of Mining. Min. Congr. J., Mar. 1979, pp. 17-22.

17. Evans, I., and C. D. Pomeroy. The Strength, Fracture, and Workability of Coal. Pergamon, New York, 1966, pp. 32-65.

18. Gaddy, F. L. A Study of the Ultimate Strength of Coal as Related to the Absolute Size of the Cubical Specimens Tested. Bull. 49, VA Polytech. Inst., 1954, pp. 1-27.

19. Gercek, H. Stability of Investigations in Room-and-Pillar Coal Mining. Ph.D. Thesis, PA State Univ., University Park, PA. 1982, 186 pp.

20. Gerdeen, J. C., V. W. Snyder, G. L. Viegelahn, and J. Parker. Design Criteria for Roof Bolting Plans Using Fully Resin-Grouted Nontensioned Bolts To Reinforce Bedded Mine Roof. Volume V. Synthesis and Design Criteria, BuMines OFR 46(5)-80, July 1977, pp. 100-109.; NTIS PB 80-180094.

21. Goodyear Tire and Rubber Company. Data Sheet, Roof Bolt Compression Pad, 4 pp.

22. Greenwald, H. P., H. C. Howarth, and I. Hartmann. Experiments on Strength of Small Pillar of Coal in the Pittsburgh Bed. BuMines TP 605, 1939, 22 pp.

23. ____. Progress Report: Experiments on Strength of Small Pillars of Coal in the Pittsburgh Bed. BuMines RI 3575, 1941, 6 pp.

24. Griffith, W., and E. T. Conner. Mining Conditions Under the City of Scranton, PA, BuMines B 25, 1912, 89 pp.

25. Grobbelaar, C. The Theoretical Strength of Mine Pillars. Paper in Proceedings of 2nd Int. Soc. Rock Mech., Belgrade, Yugoslavia, 1970, pp. 4-17.

26. Hanna, K., and D. Conover. Improved Design and Support Techniques for Coal Mine Entry Intersections. Paper in Proceedings of 8th International Strata Control Conference, Dusseldorf, Federal Republic of Germany, May 22-24, 1989, p. B15.

27. ____. Design of Coal Mine Entry Intersections. Soc. Min. Eng. AIME preprint 88-39, 1988, 11 pp.

28. Hanna, K., D. Conover, K. Haramy, and R. Kneisley. Structural Stability of Coal Mine Entry Intersections—Case Studies. Ch. 74 in Rock Mechanics: Key to Energy Production, ed. by H. L. Hartman. Soc. Min. Eng. AIME, 1986, pp. 512-519.

29. Hanna, K., K. Haramy, D. Conover, and D. Dopp. Effect of High Horizontal Stress on Coal Mine Entry Intersection Stability. Paper in Proceedings of Fifth Conference on Ground Control in Mining, ed. by A. W. Khair and S. S. Peng. WV Univ., 1986, pp. 167-182.

30. Hanna, K., K. Haramy, and D. Conover. Field Investigations of Roof and Pillar Stability in Coal Mine Intersections. Paper in Proceedings of Second Conference on Ground Control problems in the Illinois Coal Basin, Southern IL Univ., Carbondale, IL, May 29-31, 1985, pp. 77-83.

31. Haramy, K. Y. Borehole Shear Tester: Equipment and Technique. BuMines IC 8867, 1981, 19 pp.

32. Haramy, K. Y., and M. J. DeMarco. Use of the Borehole Shear Tester in Pillar Design. Paper in Proceedings of 24th U.S. Symposium on Rock Mechanics, College Station, TX, June 20-23, 1983, pp. 639-644.

33. Higdon, A., E. H. Olsen, W. B. Stiles, and J. A. Weese. Mechanics of Materials. Wiley, 2d ed., 1967, 591 pp.

34. Holland, C. T. The Design of Coal Pillars for Overburden Support-Part I and II. Min. Congr. J., Mar. 1962, pp. 24-32, and Apr. 1962, pp. 66-71.

35. ____. The Strength of Coal in Mine Pillars. Paper in Proceedings of 6th Symposium on Rock Mechanics, Univ. MO, Rolla, MO, Apr. 1964, pp. 450-456.

36. ____. Factors in the Design of Barrier Pillars in Coal Mines. Paper in Proceedings of W. Va. Coal Mining Institute, WV Univ., 1965, pp. 109-126.

37. Hooker, V. E., J. R. Aggson, and D. L. Bickel. Improvements in the Three-Component Borehole Deformation Gage and Overcoring Techniques. BuMines RI 7894, 1974, 29 pp.

38. Hooker, V. E., and C. F. Johnson. Near-Surface Horizontal Stresses Including the Effects of Rock Anisotropy. BuMines RI 7224, 1969, 29 pp.

39. Horino, F. G., and M. L. Ellickson. A Method for Estimating Strength of Rock Containing Planes of Weakness. BuMines RI 7449, 1970, 29 pp.

40. Hustrulid, W. A. A Review of Coal Pillar Strength Formula. Rock Mech. 8, 1976, pp. 115-145.

41. Kmetz, W. J. Roof Trusses Support Problem Strata. Coal Age, v. 75, No. 1, Jan. 1970, pp. 64-68.

42. Krausse, H. F., H. H. Damberger, W. J. Nelson, S. R. Hunt, C. T. Ledvina, C. G. Treworgy, and W. A. White. Roof Strata of the Herrin (No. 6) Coal Member in Mines of Illinois: Their Geology and Stability. IL State Geologic Surv. Mineral Note 72, May 1979, 54 pp.

43. Lama, R. D. A Comparison of the In Situ Mechanical Properties of Coal Seams. Colliery Eng., v. 1, 1966, pp. 20-25.

44. Lama, R. D. In Situ and Laboratory Strength of Coal. Paper in Proceedings of 12th Symposium Rock Mechanics, Univ. MO, AIME, (NY), 1971, pp. 265-300.

45. Lu, P. H. Mining-Induced Stress Measurement with Hydraulic Borehole Pressure Cells. Paper in Proceedings of the 25th U.S. Symposium on Rock Mechanics, Evanston, IL, June 25-27, 1984, SME/AIME, Ch. 22, pp. 204-211.

46. ____. Stability Evaluation of Retreating Longwall Chain Pillars with Regressive Integrity Factors. Paper in Proceedings of 5th Congress on Rock Mechanics, Int. Soc. Rock Mechan., Melbourne, Australia, Apr. 1983, A. A. Balkema, Netherlands, pp. E37-E40.

47. ____. Determination of Ground Pressure Existing in A Viscoelastic Rock Mass by Use of Hydraulic Borehole Pressure Cells. Paper in Proceedings of International Symposium on Weak Rock. Tokyo, Japan, Sept. 1981, v. 1, pp. 459-465.

48. ____. Rock Mechanics Instrumentation and Monitoring for Ground Control Around Longwall Panels. Paper in Proceedings, International Symposium on State-of-the-Art of Ground Control in Longwall Mining and Mining Subsidence, Hawaii, U.S.A., Sept. 1982, SME/AIME, pp. 159-166.

49. McCulloch, C. M., M. Deul, and P. W. Jeran. Cleat in Bituminous Coalbeds. BuMines RI 7910, 1974, 25 pp.

50. Muskhelishvili, N. I. Some Basic Problems of the Mathematical Theory of Elasticity. P. Noordhoff Ltd., 1953, 704 pp.

51. Obert, L., and W. I. Duvall. Rock Mechanics and the Design of Structures in Rock. Wiley, 1967, 650 pp.

52. Overbey, W. K. Jr., C. A. Komar, and J. Pasini. Predicting Probable Roof Fall Areas in Advance of Mining by Geological Analysis. BuMines TPR 70, May 1973, 17 pp.

53. Panek, L. A. Estimating Mine Pillar Strength from Compression Tests. SME/AIME Trans., v. 268, 1980, pp. 1749-1761.

54. Panek, L. A., and J. A. Stock. Development of a Rock Stress Monitoring Station Based on the Flat Slot Method of Measuring Existing Rock Stress. BuMines RI 6537, 1964, 61 pp.

55. Peng, S. S. Coal Mine Ground Control. Wiley, 1978, 431 pp.

56. ____. Roof Falls in Underground Coal Mines. Dep. Min. Eng., WV Univ., Morgantown, WV, Tech. Rep. No. TR 80-4, Sept. 1980, 44 pp.

57. Reed, J. J. Case History in Pillar Recovery. Min. Eng., July 1959, pp. 701-705.

58. Salamon, M. D. G. Stability, Instability and the Design of Pillar Workings. Int. Rock Mech. and Min. Sci., v. 7, 1970, pp. 613-631.

59. Salamon, M. D. G., and A. H. Munro. A Study of the Strength of Coal Pillars. J. S. Afr. Inst. Min. and Metall., v. 68, Sept. 1967, pp. 55-67.

60. Western Support Systems. Data Sheet, Intersection Truss Bolt, 2 pp.

61. Sellers, J. B. The Measurement of Rock Stress Changes Using Hydraulic Borehole Gages. Int. J. Rock Mech. Min. Sci., v. 7, 1970, pp. 423-435.

62. Skelly, W. A., J. Wolgamott, and F. Wang. Coal Mine Pillar Strength and Deformation Prediction Through Laboratory Sample Testing. Paper in Proceedings of 18th Symposium Rock on Mechanics, CO Sch. Mines, Keystone, CO, 1977, pp. 2B5-1—2B5-5.

63. Stahl, R. W. Survey of Practices in Controlling Roof at Intersections and Junctions in Underground Coal Mines. BuMines IC 8113, 1962, 13 pp.

64. Steart, F. A. Strength and Stability of Pillars in Coal Mines. Chem. Met. Min. Soc. (S. Africa), v. 54, 1954, pp. 307-325.

65. Timoshenko, S., and S. Woinowsky-Krieger. Theory of Plates and Shells. McGraw-Hill, 2d ed., 1959, 580 pp.

66. Unal, E. Development of Design Guidelines and Roof-Control Standards for Coal-Mine Roofs. Ph.D. Thesis, PA State Univ., University Park, PA, 1983, 355 pp.

67. Wagner, H. Determination of Complete Load Deformation Characteristics of Coal Pillars. Paper in Proceedings of 3d International Conference on Rock Mechanics, Denver, CO, v. 11-B, 1974, pp. 1076-1082.

68. Wardell, K. Guidelines for Mining Under Surface Water (contract H0252021). BuMines OFR 30-77, 1976, 67 pp.

69. Westgate, L. M., and T. F. Anderson. Isotropic Evidence for the Origin of Sulfur in the Herrin (No. 6) Coal Member of Illinois. Int. J. Coal Geology 4, 1984, pp. 1-20.

70. Wilson, A. H., and D. P. Ashwin. Research Into the Determination of Pillar Size. Part I. An Hypothesis Concerning Pillar Stability. Min. Eng., Inst. Min. Eng., June 1972, pp. 409-417.

71. Worotnitki, G., and R. Walton. Triaxial "Hollow Inclusion" Gauge for Determination of Rock Mass In Situ. Paper in Proceedings of Symposium on Investigation of Stress in Rock-Advances in Stress Measurements. Sydney, Australia, 1976, pp. 1-18.

72. Wright, F. D. Roof Control Through Beam Action and Arching. SME Mining Engineering Handbook, v. 1, Section 13.7, AIME, 1973, pp. 13-80 and 13-96.

APPENDIX A.—CRITICAL LITERATURE REVIEW

The structural behavior of intersections has been addressed by previous studies in roof and pillar design, failure behavior, and support techniques. The studies generally involve only one aspect of the intersection structure, such as the roof or pillars, or treat intersections as a special case of the more general single-entry mine openings. The following sections discuss some of the relevant technical background regarding intersection design theories, failure behavior, and support methods.

ROOF DESIGN THEORIES

In underground coal mine openings, the roof is the most important structural element because of the severe safety hazards and operational difficulties associated with roof falls. Coal mine roof is typically composed of bedded rock characterized by smooth and flat bedding planes, with weak bonding between beds. When the coal is mined, the roof separates into distinct layers, or plates, which are loaded uniformly by their own weight and the weight of any thinner or less stiff overlying layers. Thus, rock mechanics investigations of coal mine roof problems are commonly based on two fundamental theories: the beam theory and the plate theory. Application of these theories is limited to relatively thin roof layers having properties that can be approximated by a homogeneous, linearly elastic material.

Beam theory:—The beam theory is an approximation of the plate theory and is generally used to analyze roof conditions in entries, where the ratio of entry length to room width is greater than two. The theory is also limited to cases where the ratio of room width to roof layer thickness is greater than eight. Each roof layer is idealized as a transversely loaded beam spanning the entry. The ends of the beam, over the pillar ribs, are commonly considered fixed, although simply supported end conditions are sometimes applied.

For a uniformly loaded, fixed-end beam, the maximum shear and tensile stresses occur at the ends and the maximum deflection occurs at the center of the beam. The maximum stresses and deflection are calculated as follows (*2*):[1]

$$\tau_{max} = \frac{3qW}{4t}, \qquad \text{(A-1)}$$

$$\sigma_{max} = \frac{qW^2}{2t^2}, \qquad \text{(A-2)}$$

and

$$D_{max} = \frac{qW^4}{32Et^3}, \qquad \text{(A-3)}$$

where τ_{max} = maximum shear stress, psi,

σ_{max} = maximum tensile stress, psi,

D_{max} = maximum deflection, in,

q = uniform load per unit length, lb/in,

W = room width, in,

t = roof layer thickness, in,

and E = Young's modulus, psi.

Plate theory:—The plate theory is used when the ratio of the longer lateral dimension (length) of the plate to the shorter dimension (width) is less than two. This situation occurs at intersections where the length and width are usually equal. The plate theory is limited to cases where the ratio of the plate width to the plate thickness is greater than four. The edges of the plate are commonly assumed to be fixed, and the maximum stresses and deflection occur at the center of the plate. The following equations are used to determine the maximum tensile stress and deflection for a uniformly loaded, clamped edge plate (*2*):

$$D_{max} = \frac{A\acute{q}W^4}{Et^2} \qquad \text{(A-4)}$$

and

$$\sigma_{max} = \frac{6B\acute{q}W^2}{t} \qquad \text{(A-5)}$$

where D_{max} = maximum deflection, in,

σ_{max} = maximum tensile stress, psi,

W = shorter lateral dimension (width), in,

$\acute{q}$ = uniform load per unit area, psi,

E = Young's modulus, psi,

t = thickness, in,

and A and B = constants given in table A-1.

[1]Italic numbers in parentheses refer to items in the list of references preceding the appendix.

Table A-1.—Constants for use in plate equations (for Poisson's Ratio = 0.3) (2)

L/W	A	B
1.0	0.0138	0.0513
1.1	.0164	.0581
1.2	.0188	.0639
1.3	.0209	.0687
1.4	.0226	.0726
1.5	.0240	.0757
1.6	.0251	.0780
1.7	.0260	.0799
1.8	.0267	.0812
1.9	.0272	.0822
2.0	.0277	.0829

L/W Length-width ratio of plate.

PILLAR DESIGN THEORIES

Pillar stability influences the stability of adjacent intersections in many ways. Rib failures may result in increased entry spans leading to roof or floor failures. Redistribution of stresses caused by pillar failures may disrupt arch structures in the roof or promote slippage along discontinuities. The deformations and changes in geomechanical properties accompanying pillar failure may also adversely influence the stresses and deformations in surrounding strata.

In deciding the appropriate size of mine pillars, an effort should be made to achieve maximum extraction under safe working conditions. Hence, pillars should be made as small as possible while maintaining pillar stability or subsidence requirements. The design of pillars is basically approached by the traditional material strength equation

$$\sigma_p > (SF)\ (\sigma_v) \qquad (A\text{-}6)$$

where σ_p = pillar strength, psi,

σ_v = stress imposed on the pillar, psi,

and SF = safety factor, depends on rock conditions and mining requirements.

Since the late 1800's, many investigators have studied the effect of sample shape and size on the compressive strength of small samples of coal and rock (*10, 18, 34-35, 40, 46, 62*). Other researchers suggested that if strength results are to be applied to full-size pillar design, they should originate from large-scale in situ data. The first large-scale in situ tests were conducted by Greenwald (*22-23*) between 1939 and 1940 in the Pittsburgh coal seam. The tests, conducted on 10 square pillars, resulted in the following equation:

$$\sigma_p = 2800w^{1/2}/h^{5/6} \qquad (A\text{-}7)$$

where σ_p = pillar strength, psi,

w = pillar width, in,

and h = pillar height, in.

Numerous investigators have adopted similar approaches (*7-8, 25, 44, 67*), while others have based their work on statistical methods (*17, 25, 57-58*). Salamon (*59*) researched 125 case studies of mine pillars in South African collieries and derived the following empirical formula which defines the strength of coal pillars as a function of pillar height and width:

$$\sigma_p = 1322h^{0.66}/w^{0.46} \qquad (A\text{-}8)$$

where σ_p = pillar strength, psi,

w = pillar width, ft,

and h = pillar height, ft.

Bryan (*9*), Panek (*53*), and others (*36, 39-40, 43, 64*) used theoretical approaches for the design of mine pillars based on Mohr's failure criterion, the theory of elasticity, or other similar criteria.

In 1972, Wilson (*70*) presented the confined core theory which states that within a typical pillar two regions exist: a confined core region and a yield zone. The yield zone occurs along the pillar ribs and surrounds the confined core in the pillar interior. The coal strength ranges from nearly zero at the ribs to full strength in the confined core. Excavation of adjoining entries causes the pillar to fail from the rib inward, until the confined strength of the coal exceeds the imposed load. The vertical stress at this location is termed the peak abutment stress and occurs at the boundary between the yield zone and the confined core. Wilson's equations for estimating the depth of the yield zone and the peak abutment stress are listed below:

$$y = \frac{h}{\sqrt{K(K-1)}} \cdot \ln(\sigma_v/\sigma_o), \qquad (A\text{-}9)$$

$$\sigma_v = K\,\sigma_H + \sigma_o, \qquad (A\text{-}10)$$

and

$$K = \frac{1 + \sin\phi}{1 - \sin\phi}, \qquad (A\text{-}11)$$

where y = depth of yield zone, ft,

σ_v = peak abutment stress, psi,

σ_o = unconfined compressive strength, psi,

σ_H = lateral confining stress, psi,

h = mining height, ft,

and ϕ = angle of internal friction, deg.

In 1983, Lu (*46*) of the Bureau proposed a novel approach to evaluate the stability of conventionally designed pillars using the regressive integrity factor. He defined the integrity factor as the ratio of the integrated total strength to the integrated total load across the pillar profile. Both strength and load were derived from in situ horizontal and vertical pillar stresses, determined using Bureau hydraulic borehole pressure cells.

Most existing pillar design equations are based on experimentally derived curves for specific coal types, sample sizes, and sample geometries. Much confusion exists in the mining industry in selecting the appropriate equation(s) to use for a particular coal seam and mining plan. To reduce this confusion and simplify the task of selecting a design equation, the existing pillar design equations were evaluated to identify similarities and inconsistencies between equations. The evaluation resulted in the following requirements, which a design equation must meet to be considered for practical application:

1. Constraint within the pillar is an important factor, and must be included in a pillar design equation (*5*). Field tests proved that the relationship between constraint and the distance from the pillar rib is nonlinear. Constraint is commonly included in design equations as a width-to-height ratio term.

2. The function described by the design equation should have a shape similar to curve *A* in figure A-1. Curve *B* is inappropriate because it represents a linear relationship between strength and constraint. Curve *C* is not valid because the pillar should become infinitely strong as the pillar width is increased. Curve *D* is not valid because it predicts a nonzero strength as the pillar width approaches zero.

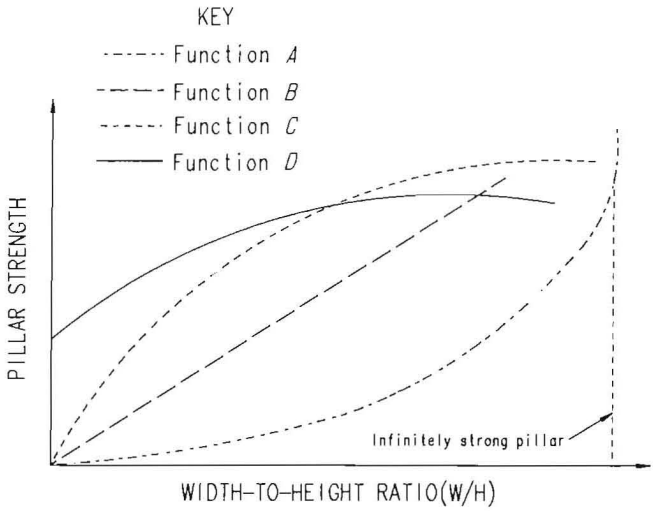

Figure A-1.—Pillar strength versus width.

Equations that meet the above criteria have the form

$$\sigma_p / \sigma_c = A + B \frac{W^{\alpha}}{H^{\beta}} \qquad \text{(A-12)}$$

where A, B, α, β = experimentally derived constants,

W = pillar width, ft,

H = pillar height, ft,

σ_p = pillar strength, psi,

and σ_c = unconfined compressive strength of a 1-in coal cube, psi.

Table A-2 summarizes the existing design equations that have the form of equation A-12. Example plots of equation A-12 using various values for the constants A, B, σ, and β are shown in figure A-2. These plots will allow design engineers to determine values for the constants, which are most appropriate for a particular application.

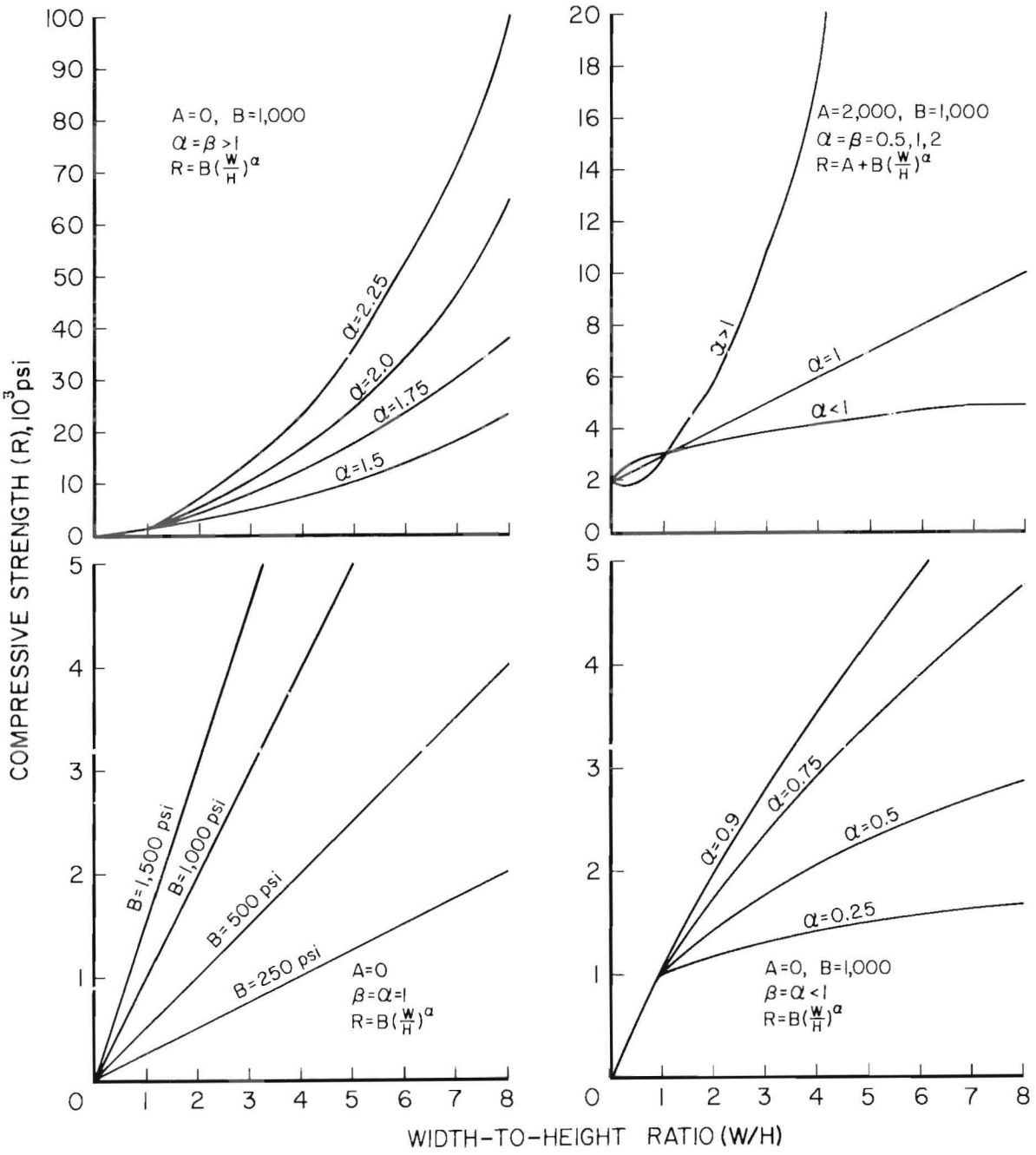

Figure A-2.—Relationships between compressive strength of pillar and W/H ratio for different forms of equation. A, B, α, and β are constants.

Table A-2.—Pillar design formulas of form $\sigma_p/\sigma_c = A + B (W^{\alpha}/H^{\beta})$

Year	Investigator	Constants				Sample size	Coal or seam tested	Country
		A	B	α	β			
1911	Bunting (*10*)	1,750	750	1	1	Small	Anthracite	United States.
1911	Bunting (*10*)	700	300	1	1	do.	do[2].	Do.
1912	Griffith (*24*)	0	(3)	1	0.5	Large	Pittsburgh	Do.
1939	Greenwald (*22*)	0	700	0.5	0.5	do.	do.	Do.
1941	Greenwald (*23*)	0	2,800	0.5	0.85	do.	do.	Do.
1954	Steart[1] (*65*)	0	1.04	1	1	Small	Natal	Rep. South Africa.
1956	Gaddy (*18*)	0	(3)	0.5	1	do.	Beckley and Pittsburgh.	United States.
1964	Holland (*35*)	0	(3)	0.5	0.5	do.	do.	Do.
1966	Evans (*17*)	0	(3)	-0.32	0	do.	Deep Dufryn	England.
1966	Evans (*17*)	0	(3)	-0.17	0	do.	Barnsly Hards	Do.
1967	Salamon (*60*)	0	1,322	0.46	0.66	Large	Bituminous	Rep. South Africa.
1968	Bieniawski (*7*)	0	1,100	0.16	0.55	do.	Witbank	Do.
1969	Bieniawski (*8*)	400	220	1	1	do.	do.	Do.
1972	Wilson (*71*)	0	448	1	1	do.	Not available	England.
1974	Wagner (*68*)	1,000	580	1	1	do.	Ustua	Rep. South Africa.
1974	do.	0	1,600	0.5	0.5	do.	do.	Do.
1976	Hustrulid (*40*)	0	(3)	1	0.5	Small	Existing data	Not applicable.
1976	Wardell (*69*)	1,000	20	2	2	Large	Newcastle	England.
1977	Skelly[1] (*63*)	0.78	0.22	1	1	do.	Pocahontas	United States.

[1]Used σ_c as cubical strength, while all other used σ_c = 1.
[2]From a different mine.
[3]Constant that changes with different seams.
σ_p Pillar strength, psi.
σ_c Pillar strength of 1-in cube, psi.
W Pillar width, ft.
H Pillar height, ft.

INTERSECTION FAILURE BEHAVIOR

The failure modes surrounding an entry intersection are significantly more complex than those for a single entry primarily because of the three-dimensional nature of the intersection geometry. Results from investigations conducted at two underground mines in the Illinois coal basin have identified four major parameters (fig. A-3) that characterize the structural behavior of coal mine entry intersections (*29-30*):

(1) in situ stress,
(2) geologic discontinuities and physical properties,
(3) mine geometry, and
(4) large roof span.

The first two parameters cannot be altered and designs must include provisions to mitigate their effects. The last two parameters are specified by the designer, who should be aware of the structural implications of various design alternatives. The following sections describe the complex nature of these two classes of parameters, their interaction in evaluating the intersection failure mechanism, and their importance in entry system design.

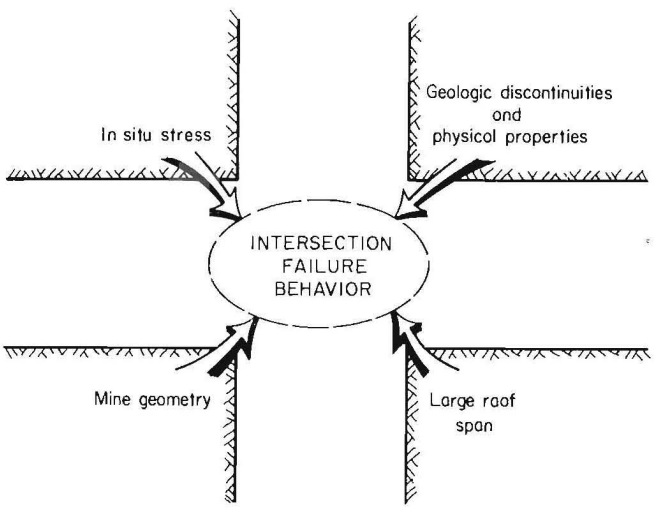

Figure A-3.—Parameters affecting behavior of entry-intersection system.

1. In situ stress and geologic conditions—Ground control problems in many U.S. coal mines are caused by high horizontal tectonic stresses and variable geology, particularly in the roof and floor. Mining practice and research show that mining-induced stresses and existing horizontal tectonic stresses influence entry stability. Most mine design studies regarding stress-related ground control problems are based primarily on mining-induced stresses; very few studies have addressed entry orientation to accommodate high horizontal tectonic stresses, geologic conditions, and rock physical properties (*28*). In a study of mines in the Beckley coalfield, Aggson (*3*) concluded that cutter roof and floor heave are caused by high horizontal stresses. He suggested that altering the mine geometry and entry orientation would reduce ground control problems.

Although much research has shown that horizontal stress commonly follows a consistent pattern within a coalfield (*3, 49*), site-specific geologic conditions, including discontinuities and rock physical properties, need to be considered to improve the stability of mine entry systems. Ground control measures that perform satisfactorily in one portion of a mine may be inappropriate in other areas. When the geologic conditions vary, ground control usually becomes more difficult until the changing geologic conditions are recognized and adjustments are made to the ground support system or mine design. In many mines, certain geologic structures, such as sandstone channels, faults, and dikes, form distinct patterns when viewed on a mine-wide scale (*11, 16, 52*). Based on the orientation of geologic structures and tectonic stresses, entry designs can be modified, roof control plans changed, and entries can be reoriented to improve ground stability.

Entry systems located in pronounced zones of heaving floor or rapidly deteriorating roof are difficult and expensive to maintain safely during the projected life of the entry system. Aggson (*3*) demonstrated that high horizontal stresses can lead to buckling floor heave. Presumably the same behavior could occur in the roof if the immediate roof is soft or moderately weak.

Coal mine entry intersections are particularly susceptible to ground control problems from high horizontal stresses because of wide roof spans and variable intersection geometry. In addition, stresses induced during intersection development may result in a high incidence of roof and rib failures.

A numerical modeling study (*19*) that addressed the intersection problem through three-dimensional finite-element analysis identified the area of influence surrounding intersections. The study indicated that a high horizontal stress field is advantageous for the stability of pillars, but is detrimental to roof stability over entries and inter sections. The study further indicated that in situ stress is a major factor controlling the extent of potentially unstable roof zones.

During the Bureau's study, various types of roof falls associated with entry intersections in high horizontal stress fields were observed. Figures A-4—A-5 show typical roof failures caused by high in situ stresses and by geological features. In one mine, major roof falls occurred while mining perpendicular to the maximum horizontal stress direction; however, the entries mined parallel to the maximum stress remained stable. Typically, the roof falls initiated at intersections and progressed along the entries mined perpendicular to the maximum horizontal stress direction. The height of these falls ranged from 6 to 20 ft into the roof forming a dome-type roof fall.

Industry experience has shown that reorienting mine entries oblique to the maximum horizontal principal stress is effective in reducing the severity of roof falls. However, regardless of entry orientation with respect to the direction of the maximum horizontal principal stress, a mine may experience difficult ground control problems (*29*). At the

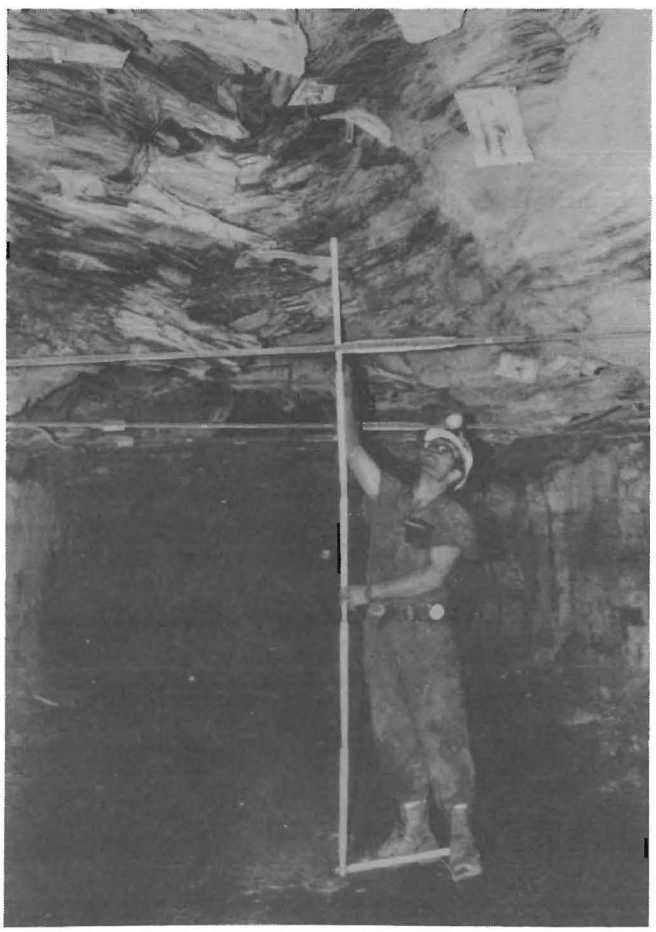

Figure A-4.—Typical intersection roof fall exhibiting stress-related shear failure.

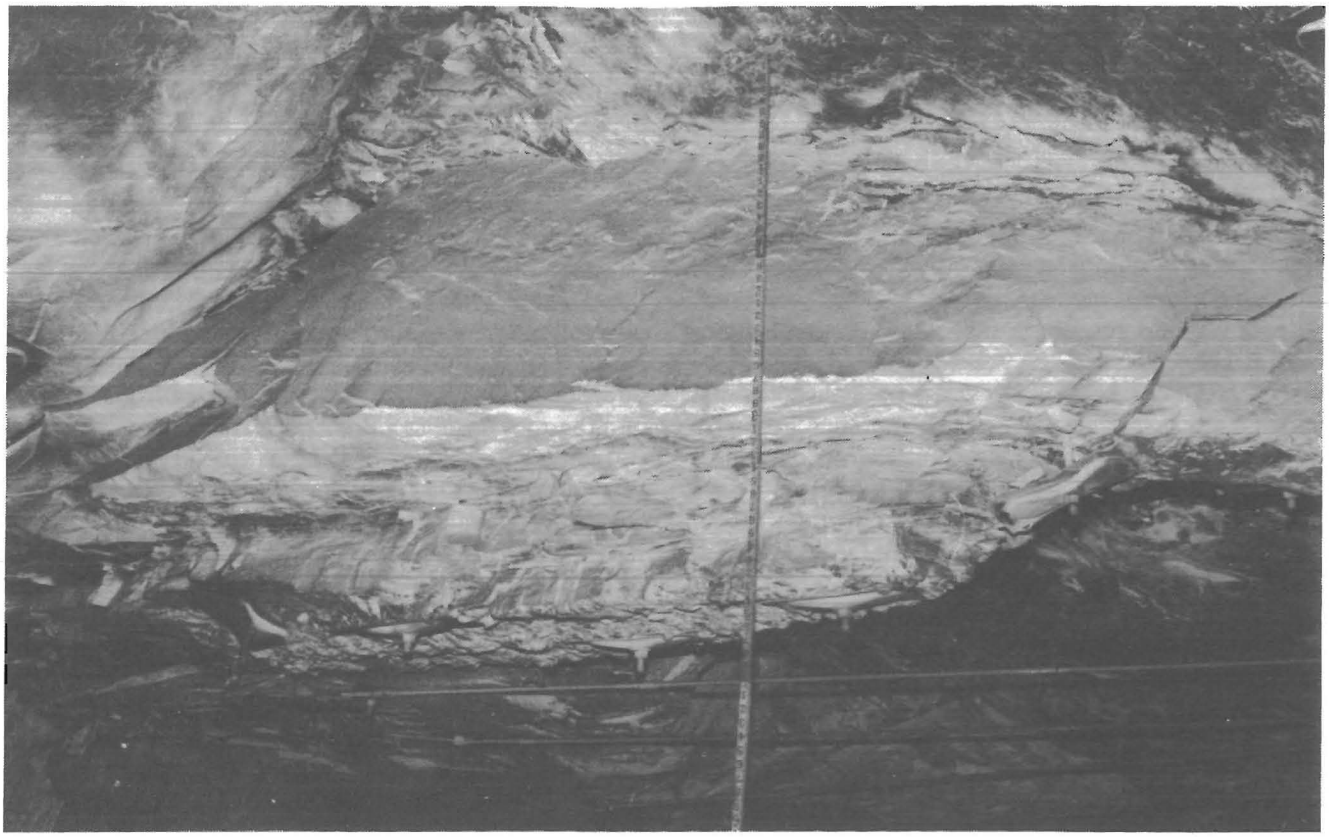

Figure A-5.—Typical roof failure caused by geologic feature.

above test site, reorienting the entries significantly improved face mining conditions. The total number of roof falls outby the working areas did not change; however, these falls were usually confined within the intersections. Figure A-4 shows a cutter roof failure pattern at a four-way intersection caused by high horizontal stress. Falls occurred during development or several hours or days after development, often with little or no warning.

Both the local and mine-wide geological characteristics are important factors influencing intersection stability. Rock strength is the most common characteristic considered in designing underground openings. Many design methods are based on the compressive or tensile strength of laboratory samples; however, the wide variation of rock properties and the occurrence of discontinuities require special consideration. Because underground coal mines generally extend over large areas, samples obtained in one section of a mine may not be representative of other areas. Laboratory tests also may be biased because the weaker samples may not survive the necessary preparation for testing, particularly for the typically weak rocks found in coal mines.

Geological discontinuities have significant influence on intersection stability and present many design difficulties. Discontinuities generally represent planes of weakness that influence the initiation and progression of failure. These discontinuities include joints, slips, faults, dikes, inclusions, partings, bedding planes, and coal cleats. The strength across discontinuities or on the contact surface between the host rock and inclusions is commonly low. Thus, stresses that are too low to fracture the intact rock may cause separation or slippage along discontinuities leading to instability. In addition, failures that initiate in intact rock may intercept and propagate along discontinuities. For example, the boundaries of roof falls generally coincide with bedding planes and joint surfaces. Figure A-5 shows the influence of a mudstone inclusion on a small roof fall.

The orientations of discontinuity surfaces often coincide with the directions of the horizontal principal stresses. However, orientations that do not coincide with the principal stress directions are also common. A comparison of the directions of measured principal stresses and certain geologic discontinuities will be presented in a later section.

Control of failures associated with geological discontinuities is accomplished through modification of the standard support plan, installation of additional supports, and alteration of entry dimensions and orientation. The support plan may be modified by changing the bolt length, spacing, or angle; using different bolt types; or installing

header blocks, straps, or crossbars. Often, additional bolts are installed through discontinuity surfaces or extra supports, such as sets, props, or cribs are installed. When passing through large-scale features which occur infrequently, the entry width and the number of entries are commonly reduced to minimize exposure to adverse ground conditions.

Generally, orientations where the entries are driven oblique to the directions of principal stresses and discontinuities provide the greatest overall stability. However, because of the complex interaction between stresses and discontinuities, the optimum orientation is difficult to determine. The final mine plan must reach a compromise between the stability of long-term openings, such as mains and haulageways, and short-term openings, such as room-and-pillar production sections and longwall panels. For example, an orientation, which provides stable development openings, may inhibit roof caving in production sections, and an orientation designed for the production sections may require excessive support and maintenance of haulageways. Similar difficulties can arise in a particular entry system. For example, an orientation based on the stress direction may be inappropriate for the direction of joints. In some cases, pillars may be offset to minimize the exposure of roof joints, or crosscuts may be angled to reduce the effects of horizontal stresses. Reorientation of local areas is seldom practical, and reorienting the entire mine once development has started is difficult, costly, and wastes resources. Thus, recognition of the relative importance of geological discontinuities on entry stability is of critical importance in the design and evaluation of underground openings.

2. Mine geometry and large roof span—The geometry around intersections contributes to higher roof stresses compared with the stresses in entry roof layers due to inherently wide (diagonal) roof spans and variable intersection shapes (*30*). As discussed previously, the beam solution used to determine stresses and deflections in the roof spanning an entry is not applicable to analyzing intersection roof conditions; however, it can be used to analyze stresses and deformations in adjacent entries and to provide an improved understanding of stress changes and displacements as the intersection is developed.

Wright (*72*) provided a method to evaluate stress conditions in intersection roof layers based on three multiplying factors, which modify the beam equations at abutment and center-of-beam locations. Analyses using this method and site-specific data indicated that the magnitude of the intersection roof stresses are nearly two times greater than those in the entries, particularly at the abutment (*28*). Consequently, the large roof span and excessive stresses at an intersection promotes a high incidence of roof and rib failure causing major ground control problems.

The numerical analysis carried out by Gercek (*19*) evaluated the effect of roof span, pillar size, and staggered pillar patterns on the stability of intersections through analysis of local stress-related safety factors. The results of the analysis are summarized below:

1. The vertical roof sag in all four-way intersection geometries is maximum at the center of the intersection. However, the maximum displacement in three-way intersections occurs near the junction of the intersection and the middle entry. For most four-way intersection geometries, the vertical roof displacement is larger than that which occurs in three-way intersections.

2. For a given roof span and pillar size, the maximum vertical stress occurs at the pillar corners, and the maximum stress at four-way intersections is larger than that at three-way intersections.

3. The critical stress concentrations in the roof of a typical intersection are much greater than in an individual opening due to sudden changes in geometry.

4. The large roof span in intersections results in a shorter stand up time than other openings having the same rock mass classification rating.

5. The distressed region that exists as an arch over an entry becomes a dome of increased height over the intersection.

6. The safety factors (SF) in the roof and floor of intersections decrease as the horizontal in situ stresses increase.

According to these results, Gercek evaluated the effect of horizontal in situ stresses on the failure behavior of a typical intersection geometry using different K ratios of S_h (horizontal stress) to S_v (vertical stress), as shown in figure A-6. For $S_h = 0$ (or, $K = \frac{S_h}{S_v} = 0$), the major roof failure mode is tensile failure at the center of the span (fig. A-6*A*). In addition, the extent of the unstable zone is largest when K = 0. The unstable zone decreases with increasing horizontal stress until K = 0.8 (fig. A-6*B* and *C*). As the horizontal stress increases further (K = 2.0), the dominant failure mode becomes that of shear (fig. A-6*D*). Figure A-7 shows the variation, for different K ratios, of a specific local SF contour in the vertical plane passing diagonally through the center of the intersection. The plots show that for the given SF of four (this value was selected for illustration only) the contour shifts upward as the horizontal stress increases. Thus, the dome failure height corresponding to a given SF is expected to increase in height as the horizontal stress increases.

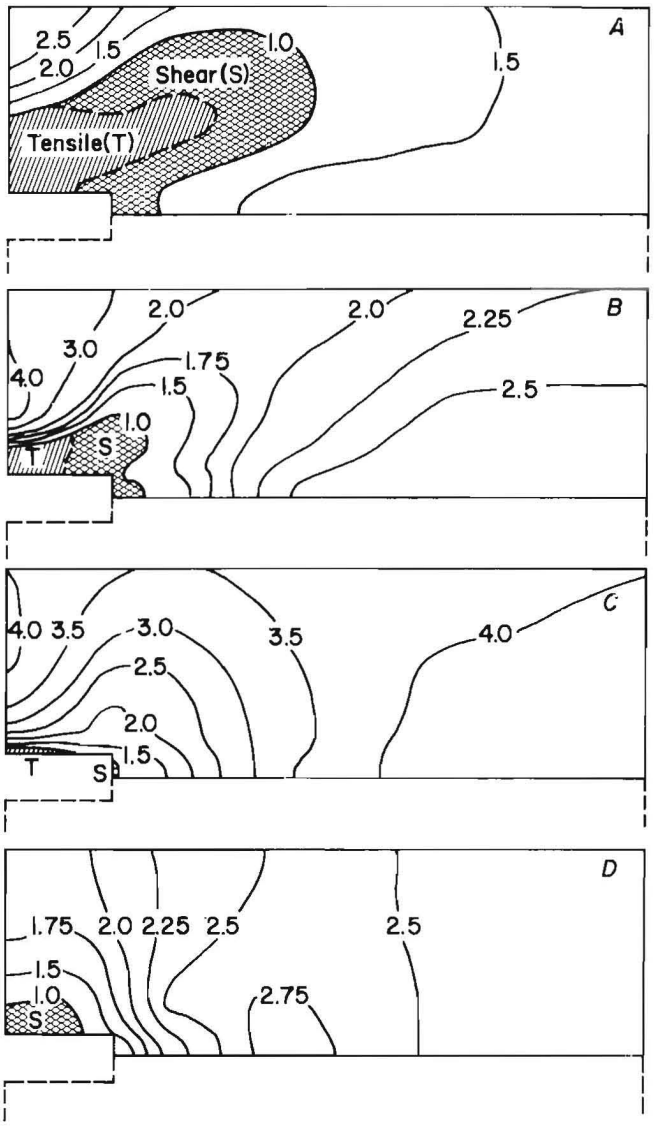

Figure A-6.—Effect of horizontal in situ stresses on local stability of four-way intersection. *A*, K = P_h/P_v = 0.0; *B*, K = P_h/P_v = 0.3; *C*, K = P_h/P_v = 0.8; *D*, K = P_h/P_v = 2.0.

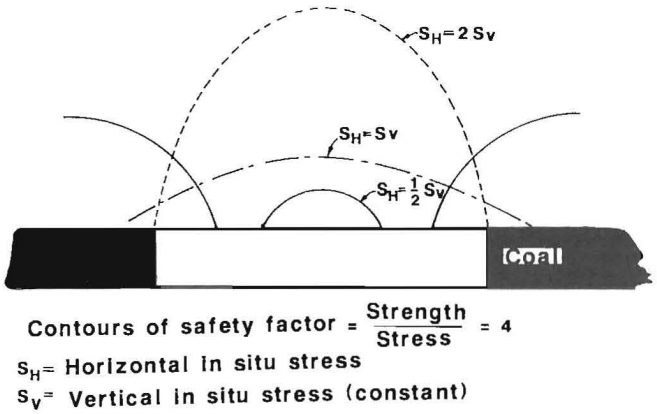

Figure A-7.—Contours of safety factor at varying horizontal in situ stress.

It is important to indicate that, in the above study, only cases where the horizontal stresses were equal in magnitude and aligned with the entries were analyzed. In addition, the influences from the actual roof failure mechanism, bed separation, intersection development sequence, and roof bolting were not considered.

INTERSECTION SUPPORT METHODS

Support of coal mine intersections is accomplished using the same basic techniques as for rooms and entries. Because of the larger roof spans and corresponding greater frequency of roof control problems existing in intersections, standard control practices have been either modified or supplemented to provide adequate support. Some design considerations, which apply to intersection support, include entry and pillar widths, orientation of openings with respect to principal stresses, development sequence to prevent abnormally high stress concentrations, leaving a thin layer of coal as the immediate roof (top coal), and utilizing a stepped face development cycle to minimize the unsupported roof span. Although application of these design factors can alleviate roof control problems, some type of artificial support will still be required.

Current support methods used to maintain the stability of entry intersections may be grouped into three general categories: roof bolts, props, and linings. Intersections are sometimes lined with concrete or shotcrete, either as the sole means of support or with steel sets and roof bolts for an ultimate strength design; however, this practice is usually reserved for long-term, permanent openings such as main haulageways or shaft stations. Because of its special application, no further discussion will be given.

For each of the roof bolts and props categories, several related support techniques are available depending upon the severity of the roof conditions and the expected lifetime for a specific opening. The roof bolting category consists of standard roof bolting techniques (mechanical bolts, resin bolts, resin and mechanical bolts, and friction type bolts, etc.), truss bolts, and the use of header boards, crossbars, and wire mesh, etc. The props category consists of either rigid or yielding steel sets, timber sets (full or partial), timber posts, hydraulic or mechanical steel posts (jacks), and wooden cribs. Cribs are used in areas of bad roof conditions and where clear access is not important. This system is also used at the entrance or the center of unused intersections, or as bridging between steel or timber sets and high roof.

The roof support pattern may be modified at intersections by installing additional, longer, or angled bolts, by decreasing the bolt spacing, or by a combination of these techniques. In an early Bureau study conducted to evaluate the support problems associated with intersections, Stahl (*63*) suggested some control measures regarding intersection support systems. These measures included (1) the use of extra bolts at intersection corners that have been trimmed; (2) the installation of posts near the entrance and cribs at the center of unused intersections; and (3) the use of steel sets under extremely bad ground conditions. Stahl also proposed the use of longer bolts (1 to 2 ft longer than regular bolts) near and at the center of intersections, and angled bolts over the pillars. Figure A-8 shows some of the special intersection-support plans that were practiced at a number of mines examined during this survey.

Another support method substitutes three-way intersections for four-way intersections using a staggered pillar pattern to reduce the effect of the large roof span on roof failure behavior. Obert and Duvall (*51*) recommended the use of a staggered pillar system as a control measure to prevent roof failures that tend to progress in a given direction.

Peng (*55*) indicated that installation of longer bolts, reduction of bolt spacing, or the employment of three-way intersections may be adequate for some areas of the mines, but may be inadequate in other areas, particularly in areas having weak roof conditions. Based on numerous case analyses conducted in the Pittsburgh coal seam, Peng (*56*) devised several roof support patterns designed to control the unstable zone above intersections. For four-way and three-way intersections, the suspension effect is provided with a bolt length longer than at least half of the entry width.

Gerdeen (*20*) conducted an extensive study involving the development of design criteria for roof bolting plans using fully resin-grouted nontensioned bolts to reinforce bedded mine roof. Roof control problems at entry intersections were also investigated. The results of the study indicate that, in the case of high in situ horizontal stress, the compressive zone is expected to move higher into the roof, and a greater bolt density or larger roof bolts are required over the intersections to prevent buckling of thin plates of roof rock. Furthermore, if there is a predominant slip direction in the intersection roof, the planks and roof bolts should be installed across the slips to prevent local roof falls. Other suggestions included:

1. If vertical bolts and/or angled bolting patterns are adequate suspension support methods for ordinary entries, the same plans can be used with (a) longer vertical bolts near the center of intersection; and (b) angled bolts extended diagonally over the pillar corners to suspend the unstable zone from intact rock.

2. When the in situ horizontal stress is low in one direction and high in other direction, the predominate arch will form in the direction of the low lateral stress. At an intersection, this arch disappears (fig. A-9 top). The formation of the arch over the intersection may be accomplished if additional bolts are installed along the edge of the intersection (fig. A-9 bottom).

A recent boundary element study (*66*) considered the rock mass rating to develop support guidelines and roof control plan standards for coal mine roofs including those in entry intersections. The study includes an empirical equation to determine the rock-load height, which the author defines as the height of the potentially unstable zone that should be controlled by support. Once the rock-load height is calculated, step-by-step procedures are provided to determine support specifications and patterns for mechanical and resin bolts in combination with planks and wood posts.

Truss bolts have been utilized for many years, and have been shown to be effective in bad roof conditions. Generally, a truss bolt consists of two steel rods anchored in inclined holes drilled into the roof over the riblines and connected by a tensioning mechanism. The application of truss support systems in intersections requires special techniques because of the wide roof span and variable intersection geometry. Various truss patterns have been devised for supporting three-way and four-way intersections, as shown in figure A-10 (*41*). Trusses may be overlapped to support wider openings, or may be installed diagonally across the intersection forming an "x" type arrangement. The carrying trusses should be installed before widening the crosscuts (fig. A-10).

Recently, Seegmiller (*60*) developed a new concept of truss bolt systems to support underground openings, particularly intersections. The system consists of angled and vertical roof bolts, brackets and tie rods (fig. A-11). The four-way bracket located in the center of the intersection roof allows the forces from each diagonal section to interact, providing continuous support. Various truss plans have been developed for supporting three-and-four-way intersection geometries (fig. A-11). One unique feature of this truss system is that the central vertical bolt reduces the large roof span and stress concentration in the center area of intersection roof.

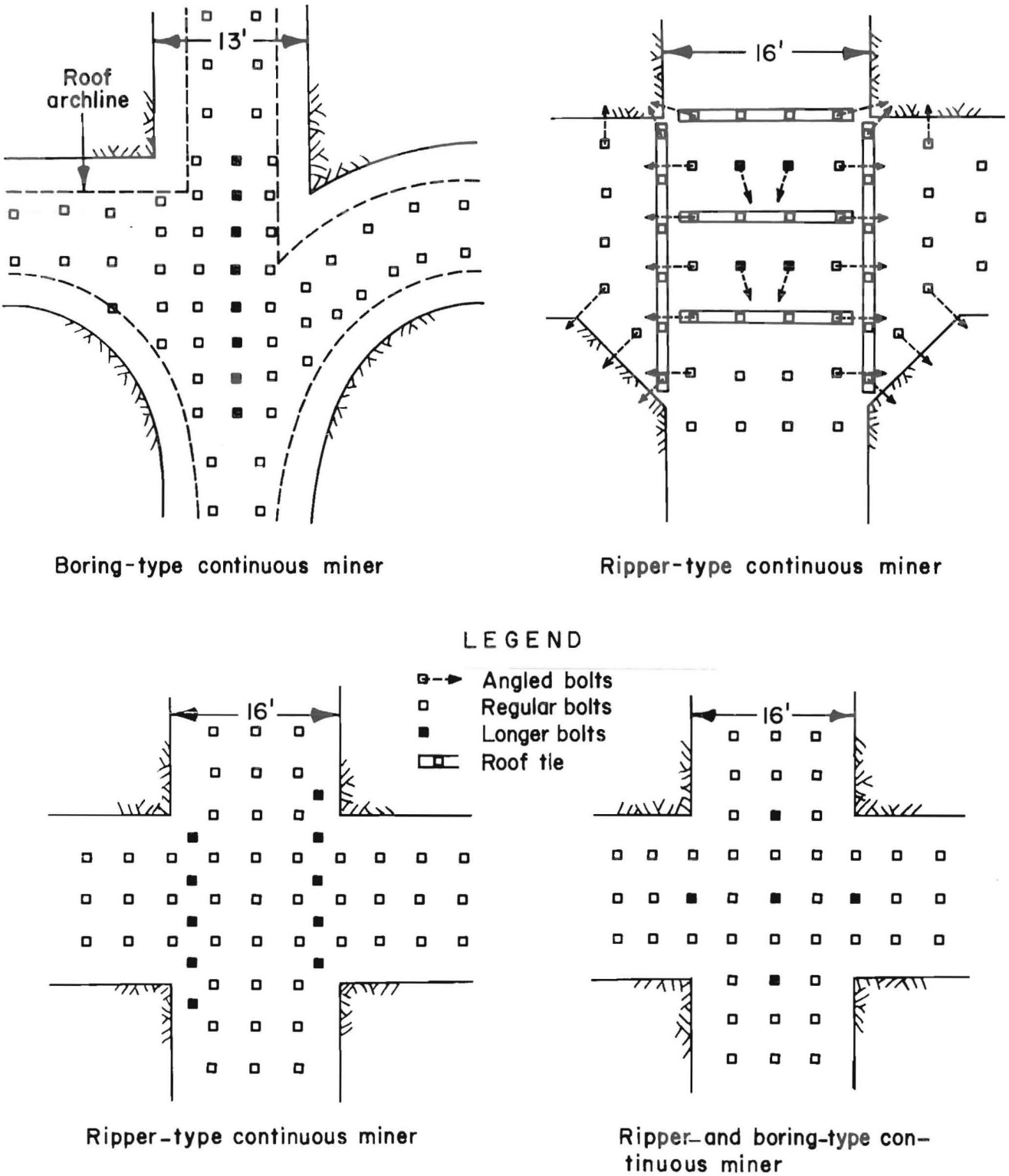

Boring-type continuous miner

Ripper-type continuous miner

Ripper-type continuous miner

Ripper- and boring-type continuous miner

Figure A-8.—Special intersection-support plans using rock bolts (*63*).

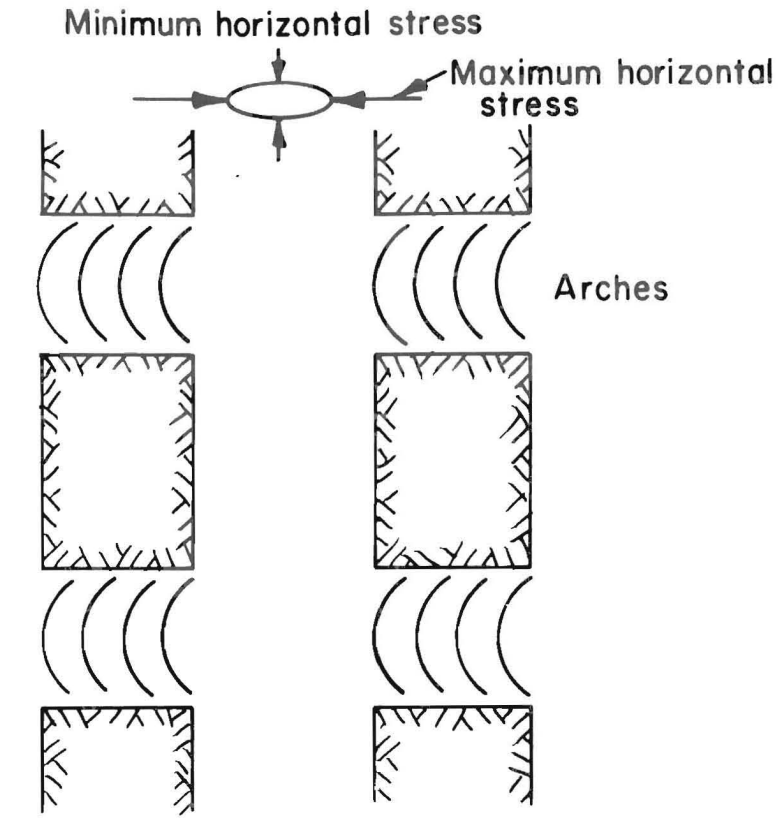

Discontinuous ground arch at an intersection

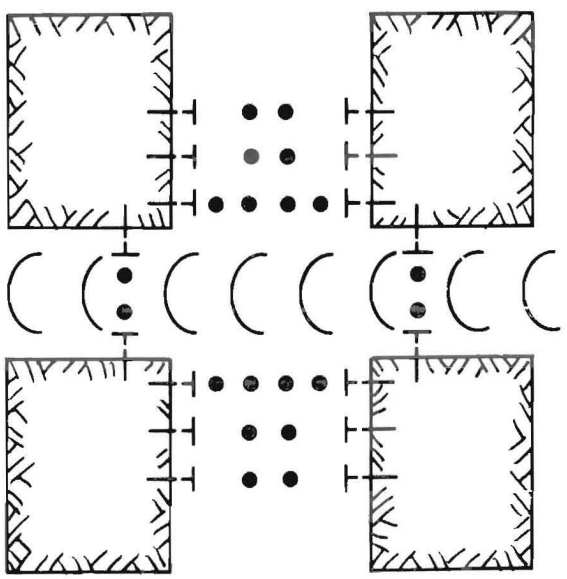

Additional bolts along the edges of an intersection

Figure A-9.—Formation of continuous ground arch over intersection (*20*).

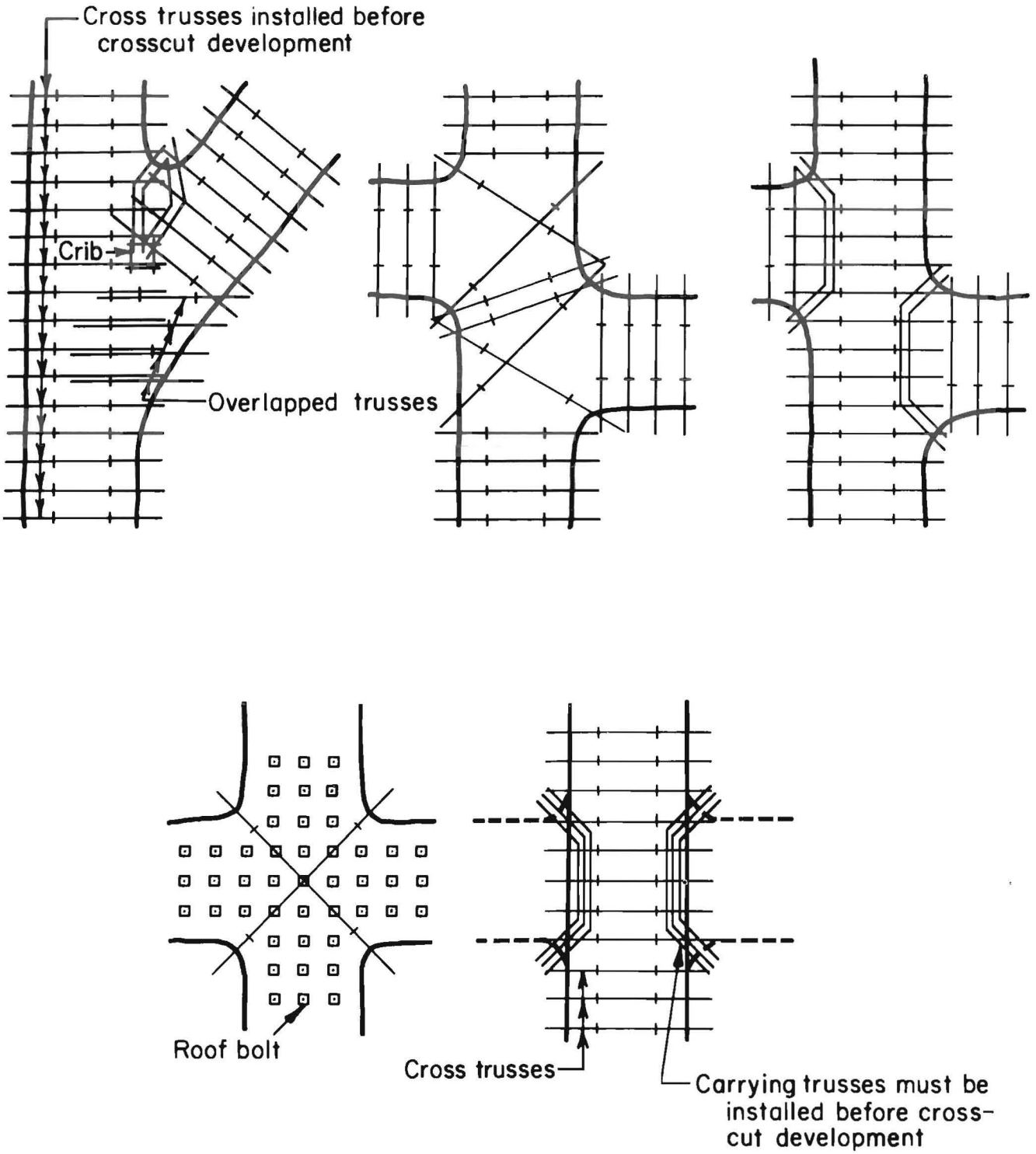

Figure A-10.—Truss bolt patterns for three-way (top) and four-way (bottom) intersection support (*41*). (Courtesy Coal Age, January 1970).

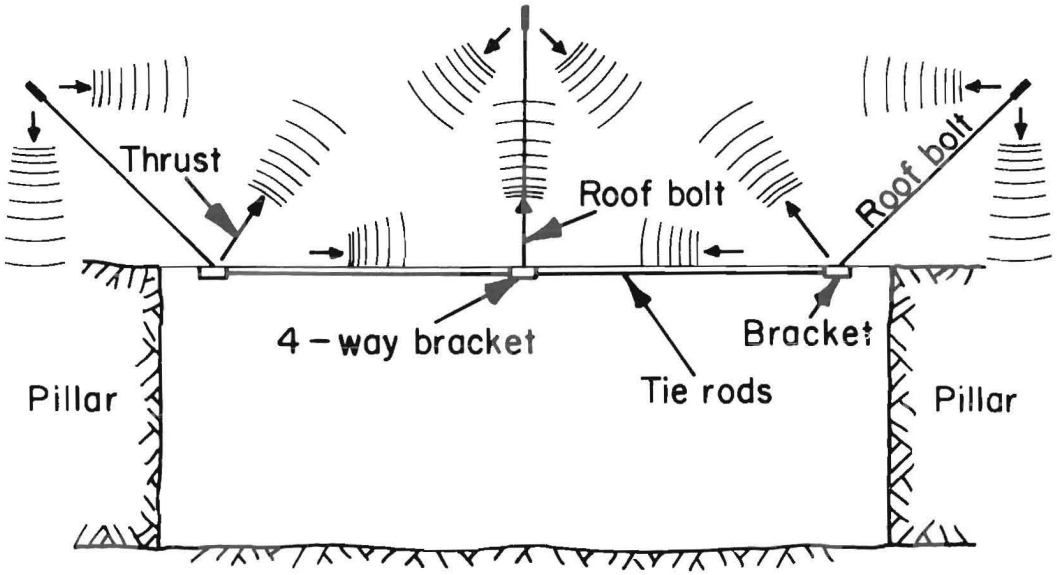

Intersection truss assembly and force distribution

3–way intersections

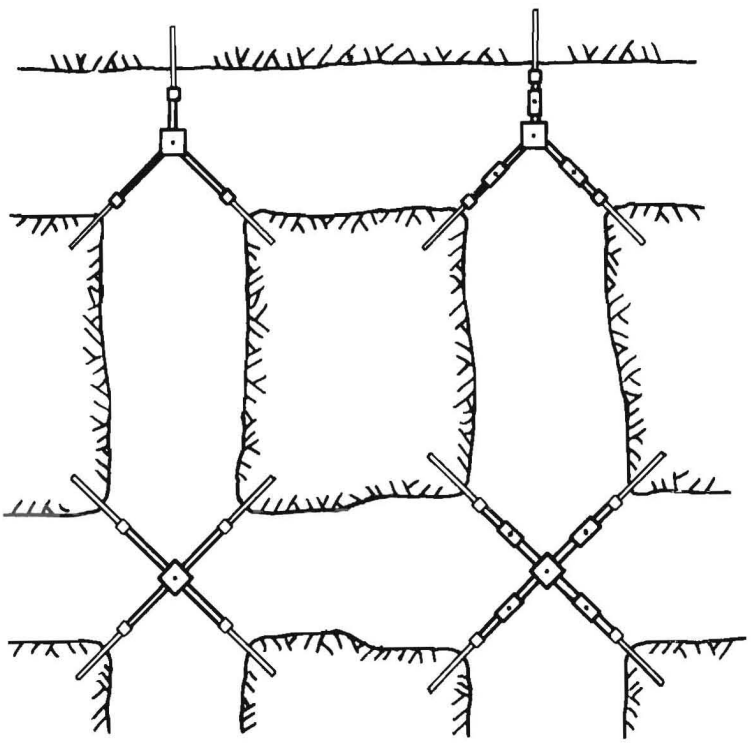

4–way intersections

Figure A-11.—Intersection Truss® bolt system (*60*).

APPENDIX B.—INSTRUMENT DESCRIPTIONS AND INSTALLATION PROCEDURES

Many types of instruments have been designed for rock mechanics measurements, ranging from simple to very complex and from those suitable for specialized applications to those that can be used under a variety of conditions.

These instruments can generally be grouped into three categories:

- instruments that measure ground stress (in situ stress and stress changes),
- instruments that measure deformations within the mine opening, and,
- instruments that measure the physical properties of the rocks—both in situ and in the laboratory.

The in situ stress instruments include strain gage arrays bonded in boreholes, borehole deformation instruments, flat jacks, hydraulic borehole pressure cells, photo-elastic instruments, vibrating wire stress meters, etc. Many of these techniques require knowledge of elastic properties of the rocks and can be used only in relatively competent rock.

Another class of instruments in this category are those which measure the loads and pressures in supports, roof bolts, gob areas, etc. These instruments are generally designed for a particular purpose and include strain gage, vibrating wire and hydraulic load cells, deformation reference points on supports, and roof bolt compression pads.

The instruments, which measure deformations in the mine opening, are quite diverse and many specially designed instruments are currently in use. The techniques usually involve measuring the change in distance between anchors or reference points mounted at the surface or at various depths in boreholes drilled into the roof, floor, and pillars. The instruments consist of conventional deformation gauges (dial gauges, verniers, strain gages, etc.), which measure the movement of rods or wires stretched between reference points. Readout can be measured manually or can be connected to continuous recording equipment.

The physical properties of rocks are generally measured in the laboratory by performing standardized failure tests (uniaxial, triaxial, flexural, etc.) on core samples obtained from the mine. The properties thus obtained are not usually representative of field conditions due to the requirement of competent samples for laboratory testing and the influence of joints, fractures, and partings on the properties of the entire rock mass. Several instruments and methods have been developed to measure the in situ physical properties of the rock mass, such as the borehole shear test, borehole dilatation technique, point load test, Schmidt hammer, penetrometer, and in situ shear bed compression test. These in situ techniques can be quite elaborate, especially when large volumes of rock are tested; however, some of the borehole techniques are simple and effective.

Selection of instruments for a specific application must consider the capability of the instrument to measure the expected level and range of pressure or deformation changes as well as the ruggedness of the unit with regard to the typically hostile mine environment. An additional consideration is the cost of the instruments, including the costs of conducting tests, taking periodic measurements, and data analysis, because several measurement stations are usually desirable for greater accuracy and for a better understanding of the stress and deformation behavior.

The following sections will discuss the function, purpose, use, installation, and measurement procedures for each instrument selected for this field study.

UNDERCORING

The undercoring method, surface rosette, determines the horizontal secondary principal stresses on a free surface by measuring the diametral displacement of the rock surface caused by drilling a stress-relief borehole. Six reference pins are installed at a constant radius from the borehole and are oriented to measure three diameters spaced 60° apart. By using stress-displacement relations derived from the elastic theory and the stress-strain properties of the rock mass, the in situ stress in the plane of measurement can be determined (*37*).

In practice, six 3/8-in-diam measurement pins are grouted in holes drilled on a 10-in-diam circle, and spaced 60° apart (fig. B-1). To ensure proper spacing of the pins and concentricity of the measuring circle and the stress relief borehole, a predrilled metal plate is used to layout the locations. After the rock surface is marked through the plate, six 3/8-in diam holes are drilled to a depth of about 1/2 in with a carbide-tipped masonry drill. The length of the measurement pins varies from 1/2 to 1 in to accommodate rock surface irregularities. Several grooves are machined on the side of the pins, and a reference hole is drilled on one end. The measurement pins are then cemented into the predrilled holes using quicksetting epoxy glue. After the glue sets, the reference holes in the top of the pins are countersunk until repeatable measurements are obtained. A Whittemore gauge (fig. B-1), having a nominal 10-in length and a resolution of 0.0001 in, is used to measure the distance between the reference holes drilled in the pins. Three readings are taken on each of the three diameters of the rosette to compensate for positioning errors. In addition, a set of three readings is taken on a calibration bar to correct for temperature effects.

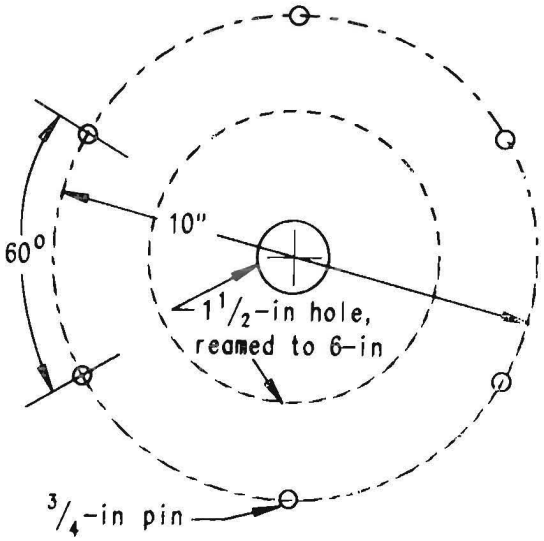

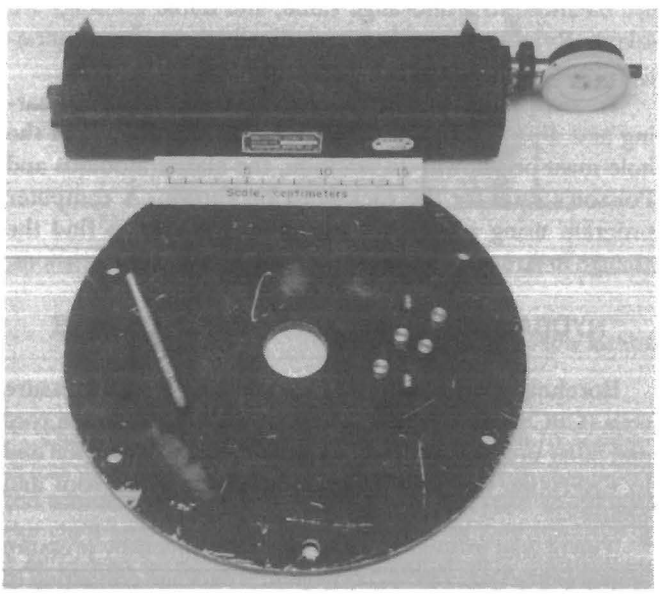

Figure B-1.—Undercoring stress-relief method. Top, surface rosette configuration; bottom, undercoring equipment—Whitemore gauge, calibration bar, metal plate and measurement pins.

After the initial readings have been taken, the 1.5-in-diam (EX) pilot hole is drilled in the center of the rosette and overcored with a 6-in-diam, thin-walled masonry bit. The 6-in-diam borehole is drilled to a depth of 9 in, and a final set of readings, including the calibration bar, are taken with the Whittemore gauge and recorded. The final readings are averaged, corrected for temperature change, and subtracted from the average initial readings to determine the diametral displacements resulting from the stress relief.

The resulting diametral displacements are the in situ deformation measurements that are used to calculate the stress distribution using elastic theory for a circular hole in an infinite medium subjected to a three-dimensional stress field.

OVERCORING

Overcoring stress-relief measurements were performed at the end of the long-term monitoring period to determine the horizontal secondary principal stresses in the roof. Two instruments were used to obtain the overcoring measurements: the three-component borehole deformation gauge, developed by the Bureau, and the hollow inclusion strain cell developed by the Commonwealth Scientific and Industrial Research Organization (CSIRO) of Australia. Overcoring, using the Bureau's borehole deformation gauge, was performed at nine depths in a borehole drilled in the roof of the entry approximately 20 ft south of the intersection. The two CSIRO strain cells were installed along the northeast-southwest intersection diagonal, and each cell collected data at a single depth. For each overcore, the following general procedure was followed:

1) A 1.5-in-diam (EX) pilot hole was drilled to the required testing depth.

2) A 6-in-diam hole was drilled, using the thin-wall overcoring bit, to the starting depth of the overcore, approximately 1 ft below the measurement plane of the deformation gauge or strain cell.

3) The gauge was connected to an appropriate readout device, and the gauge was overcored. Data were collected at 1/2-in-depth increments until overcoring had progressed approximately 1 ft past the gauge.

4) The overcore was retrieved from the hole and placed in a Bureau-developed biaxial pressure cell to determine the elastic constants of the core in the plane normal to the borehole axis. The data were reduced using a computer program, developed by the Bureau, which accounts for the anisotropic properties of the rock.

5) The overcores were returned to a Bureau laboratory for further testing to determine the elastic constants of the core in the direction parallel to the borehole.

The horizontal secondary principal stresses were calculated from the overcoring deformation or strain data and the measured elastic properties of the cores using computer programs developed by the Bureau and by the CSIRO. Techniques and procedures specific to each gauge will be discussed in the following sections.

The Bureau's Borehole Deformation Gauge

The Bureau's borehole deformation gauge measured the diametral deformation, or change in diameter, of the borehole during overcoring on three diameters oriented 60° apart (*6*). The gauge consists of six pistons that contact the borehole wall. The gauge is calibrated such that the change in strain resulting from deflections of the cantilevers provides a direct readout of the diametral deformation in microinches. The deformation data are analyzed by assuming the borehole acts as a circular hole in a linearly elastic, anisotropic plate under plane strain conditions.

Overcoring measurements, using the borehole deformation gauge, were conducted in the roof from approximately 3 ft above the roofline to 11 ft at 1-ft intervals. The range of depth covered by these measurements enabled comparisons to be made with analysis results from the HISC, installed 3 ft above the roofline, and the BPC-CPC packages, installed at depths of 2, 4, and 6 ft. In addition, the stress-relief measurements conducted furthest from the opening provided stresses outside the influence of the opening.

The overcoring technique using the Bureau's borehole deformation gauge has been well documented in previous Bureau publications (*6, 37, 50*), and the reader is referred to these references for a more complete discussion of the procedures, equipment, and data analysis techniques.

Hollow Inclusion Strain Cells (HISC)

The CSIRO HISC consists of three 3-component strain gage rosettes embedded in the wall of a hollow plastic tube (fig. B-2). The tube is bonded to the walls of an EX borehole by an epoxy cement. The strain gage rosettes are oriented in a configuration which provides sufficient data to calculate the complete three-dimensional change in stress (*71*). The in situ state of stress is determined by overcoring the cell, using the procedures discussed above.

The cells are installed in an EX corehole, extending about 2 ft from the center of the bottom of a 6-in diam borehole (fig. B-2, schematic). The strain rosettes are positioned from 6 to 18 in past the end of the 6-in hole to reduce the influence of stress concentrations on the cell. The EX core is inspected to locate an unfractured zone in which to place the cell that would most likely remain intact during overcoring.

The gage location in the EX hole is thoroughly dried and cleaned using freon and chlorinated degreasers. Any grease, oil, or water remaining in the walls of the borehole will prevent adequate bonding of the cell to the rock. During installation, the cell is filled with epoxy cement, and a piston with an extension rod is positioned inside the end of the cell using shear pins (fig. B-2, before setting). As the cell is inserted into the hole, the extension rod contacts the end of the hole forcing the piston into the cell and extruding the epoxy through several radial holes into the annular area surrounding the cell (fig. B-2, after setting). The epoxy is confined to the area covering the rosettes by rubber seals at each end of the cell body. Prior to installation, the cell body is roughened and degreased to improve bonding, and slits are cut in the seals to permit entrapped air to escape.

To determine when the cell is completely seated, breakage of a trip wire in the cell body is monitored with an ohmmeter, or alternatively, movement of the installation rods after the shear pins fail is compared with the length of the piston. Once the cell is fully inserted, it is propped in position overnight to allow the epoxy to set. After the epoxy cement has hardened, the lead wires are connected to a strain indicator through a switching unit, the channels are balanced to a midrange value, and initial readings are taken. Readings are taken periodically thereafter to monitor the change in stress.

To analyze the data, the orientation of the hole (bearing and dip) and the orientation of the strain gage in the hole must be known. In addition, the elastic modulus and Poisson's ratio for the rock must be known. A computer program using a statistical technique is used to find the change in stresses (normal and shear) in three dimensions.

HYDRAULIC BOREHOLE PRESSURE CELLS

Borehole pressure cells (BPC's) and cylindrical pressure cells (CPC's) were installed to measure the change in roof and pillar pressure caused by widening the intersection and to determine the in situ biaxial stresses in the roof and pillars.

The biaxial ground stresses are determined by pressure convergence tests (*45, 47-48*), using a package consisting of two flat BPC's and one CPC installed in a single borehole (fig. B-3). The BPC's are oriented to measure ground pressures, in the direction perpendicular to the plane of the cell, and oriented parallel to the expected direction of the secondary principal stresses. Once the in situ stresses have been determined using the BPC-CPC package, a pressure response ratio is determined, relating cell pressure to ground pressure. Using the pressure response ratio, ground pressures at other locations may be determined using only the BPC's.

Detailed descriptions of the CPC-BPC system components have been presented in previous Bureau publications (*47-48, 54*) and are briefly summarized below:

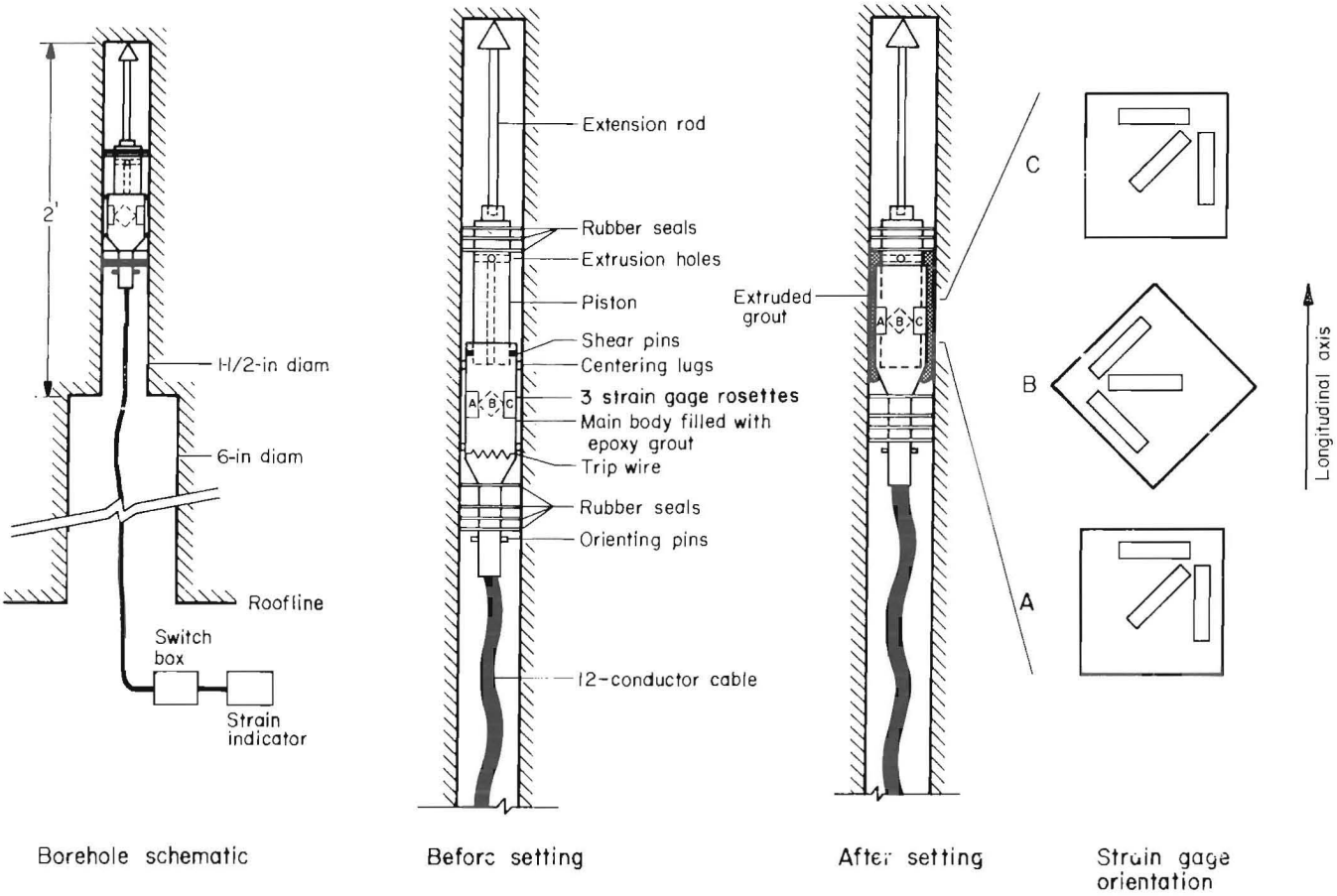

Figure B-2.—CSIRO hollow inclusion strain cell (HISC) installation layout.

The CPC consists of a copper shell brazed to a cylindrical steel core. Glycerine or hydraulic oil is pumped into the annular space between the shell and core to expand the shell against the borehole wall. The cell diameter is 1.48-in and is designed to be installed in a 1.5-in-diam drillhole. The assembled cell is 8-in long, with an effective length of 7 in. The cell measures the sum of the biaxial ground pressures.

The BPC consists of a flat mild steel cell encapsulated in a 2.34-in diam by 8.75-in-long grout cylinder. The steel cell is 2-in wide by 8-in long by 0.35-in thick. The cell is pressurized with hydraulic fluid to expand the cell against the cement jacket which bears against the borehole walls. The BPC measures pressure in the direction perpendicular to the plane of the steel cell. Two longitudinal holes are normally cast in the cement jacket to permit passage of hydraulic lines when several cells are installed in a single hole.

The cells are pressurized through steel tubing with a special pump meter utilizing a threaded piston to measure the volume of fluid injected into the cell. Once pressurized, the cells are connected by the steel tubing to individual pressure gauges or to continuous multichannel pressure recorders.

During installation, the steel tubing from the cells was routed along the roof and pillars to circular chart recorders mounted on panels installed along the ribs. The recorders accommodate two or three channels, have a range of either 5,000 or 10,000 psi, and are driven by 7-day, manually wound clock-drives. Entrapped air was bled from the tubes before the cells were initially pressurized to about 800 psi.

MULTIPLE POINT BOREHOLE EXTENSOMETER (MPBX)

Multiple point borehole extensometers were installed in the roof to measure roof sag and bed separation between four anchorages. Four spring-type anchors were installed (fig. B-4) using calibrated installation rods having a slotted

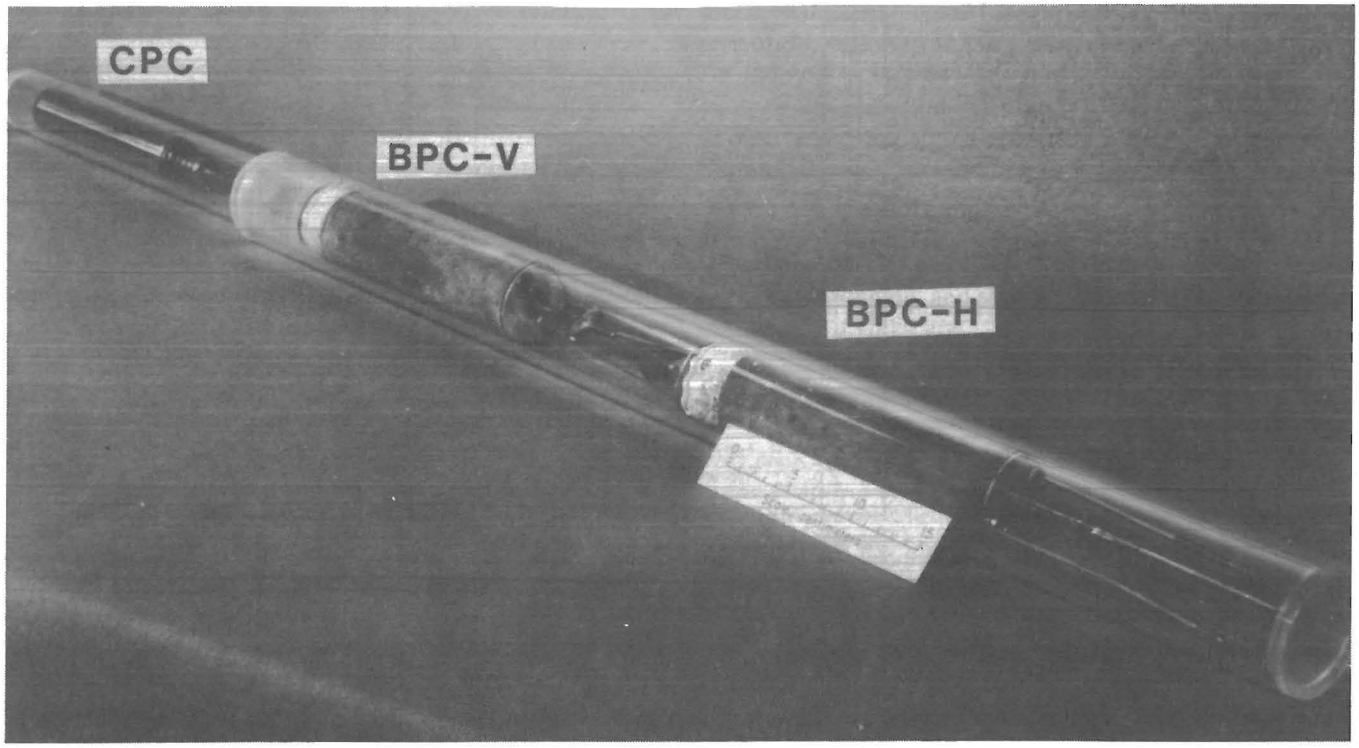

Figure B-3.—Pressure-cell package consisting of one CPC and two BPC's (*45*).

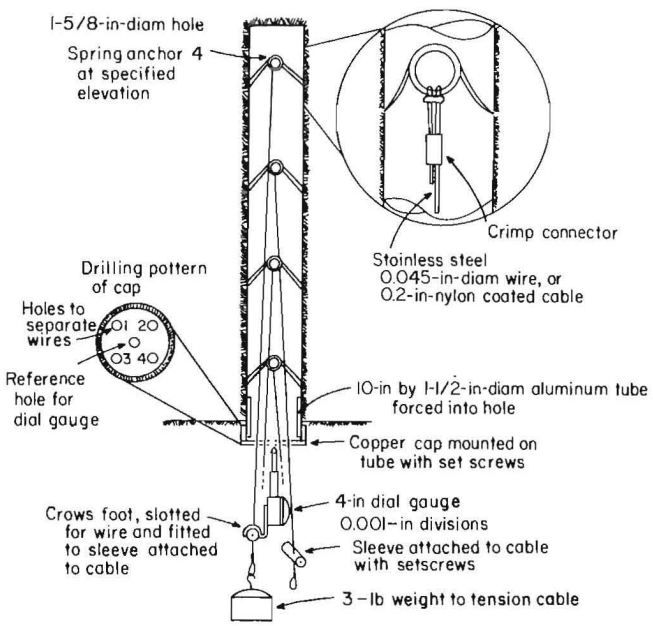

Figure B-4.—Roof extensometer installation detail—MSHA-style differential sag indicator.

tip. Prior to insertion into the 1-5/8-in-diam hole, the anchors were attached to 3/16-in-diam stranded-steel measuring cable with crimped connectors. The four cables were threaded through holes drilled in a 1-1/2-in copper cap attached to a 1-1/2-in-diam by 10-in-long aluminum pipe. The cap and pipe assembly was driven into the collar of the borehole using a special adapter to protect the cables. Brass reference sleeves were threaded over each cable and clamped such that a midrange reading was obtained on a dial gauge positioned between the sleeve and a center hole in the copper cap. The spring-type dial gauge has a resolution of 0.001 in and a measuring range of 2 in. The lower end of the cable was formed into a loop, that supported a 3-lb tensioning weight when taking measurements.

A major problem encountered with the extensometers was the loss of measuring cables due to corrosion. Water accumulation around the holes in the measuring cap initiated rusting of the cables, which then broke when the tensioning weight was applied. The corrosive water also damaged the dial gauge, necessitating periodic replacement of the spring.

A less severe problem involved the disturbance of the measuring cap or the brass sleeves due to small roof falls, which required resetting the station.

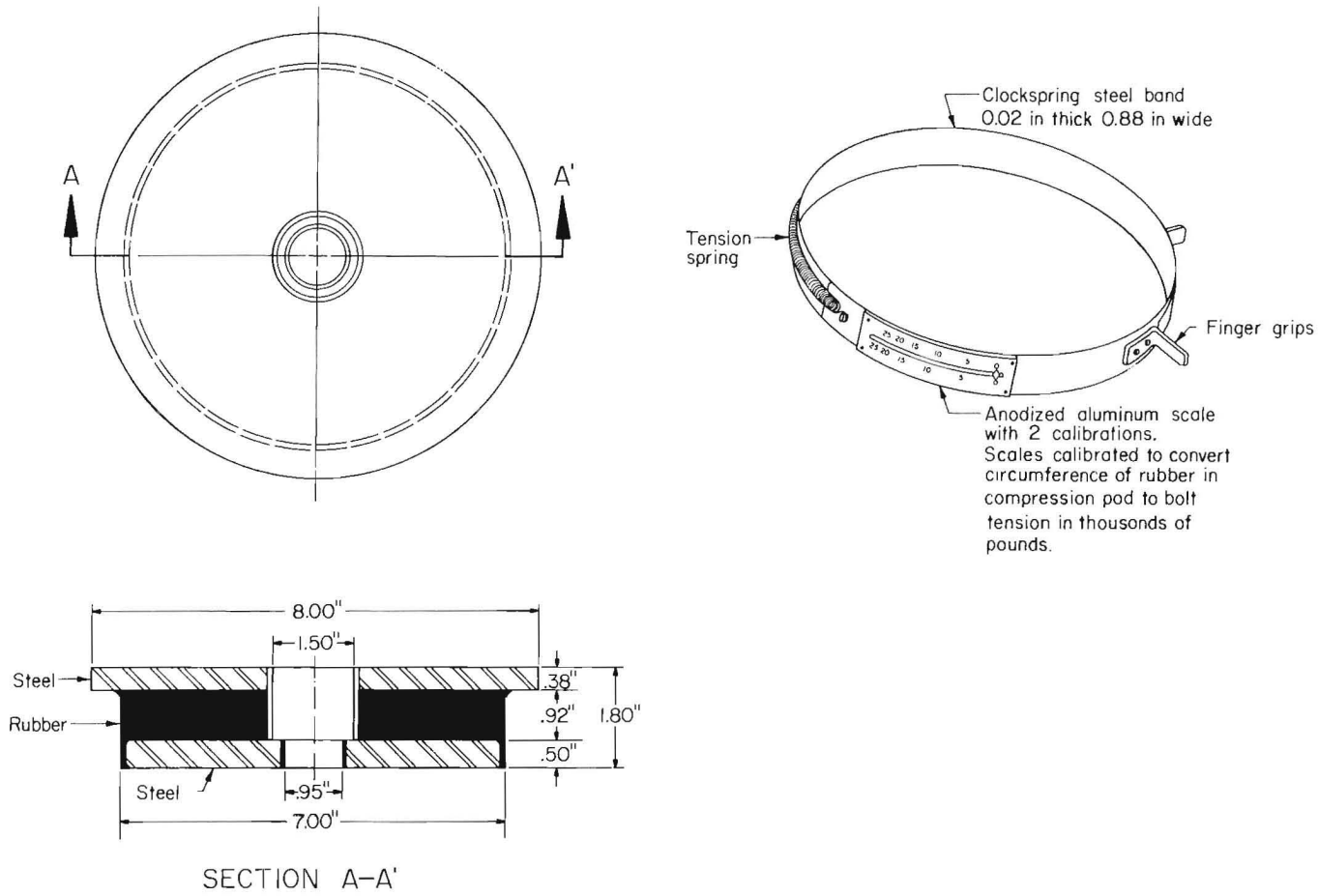

Figure B-5.—Roof bolt compression pad detail.

ROOF BOLT COMPRESSION PADS

Roof bolt compression pads were installed to measure the load on the roof bolts and to determine the change in bolt load over time. The pad consists of a 7-in-diam by 0.92-in-thick rubber slab, bonded between two steel disks, with a central hole through the entire assembly (fig. B-5). A roof bolt is threaded through the pad and installed in a standard manner. As ground pressure is transmitted to the head of the bolt, the pad is compressed and the rubber insert expands. The circumference of the pad is measured using a calibrated ring (fig. B-5), having graduations proportional to the applied load. Prior to use, the pads and ring are calibrated, using a laboratory testing machine to determine the relationship between the applied load and the ring reading. Accuracy of the compression pads is estimated to be within ±500 pounds.

ROOM CLOSURE

Each convergence station consisted of a 3/4-in-diam by 22-in-long steel reinforcing rod grouted in a 1-5/8-in-diam borehole drilled in the floor directly beneath a selected roof bolt. A rod-type extensometer (telescoping closure meter) was used to measure the distance between the bolt head and the rod in the floor. The extensometer reads directly to 0.01 in using a vernier scale and has accessory extensions to accommodate different entry heights. A special head was fabricated to fit over the bolt heads, and a conical hole was drilled in the floor rods to accommodate the lower end of the extensometer. The floor rods were installed at a depth of about 20 in to provide a solid anchorage beneath the immediate floor.

BOREHOLE SHEAR TESTER

The borehole shear tester (BST) is a device used to determine the in situ cohesion angle of internal friction of a rock mass (*31-32*). The BST consists of two hydraulic jacks. One of the jacks is inserted into a NX-size (3-in) borehole and exerts a radial pressure against the borehole walls (fig. B-6). The second jack is installed against the rock surface at the collar of the borehole and applies an axial pressure on the first jack (fig. B-7 top). The jacks are connected to a pressure monitoring and pumping unit (fig. B-7 bottom). The radial and axial pressures are linearly related to the normal and shearing stresses, respectively, in the rock as determined from calibration tests.

In practice, the axial pressure (shear stress) at failure is measured for a series of increasing radial pressures (normal stress). The shear stress data are plotted against the normal stress, and a line fitted through the data points corresponds to Mohr's failure envelope. The slope of the line determines the angle of internal friction, and the cohesion is found from the intercept of the line with shear stress axis.

The BST is mounted on RW-size (1-1/8-in) drill rod and may be supported manually to depths of about 20 feet in upholes or downholes. For longer holes, additional support apparatus is required. To conduct tests at a specific horizon, the BST is inserted to the desired depth, a preselected radial pressure is applied, and axial pressure is increased until failure occurs. The radial and axial pressures at failure are recorded, and the BST is rotated about 45° before testing at the next radial pressure increment. Before plotting, the pressure data are converted to stresses and corrected for the weight of the test assembly.

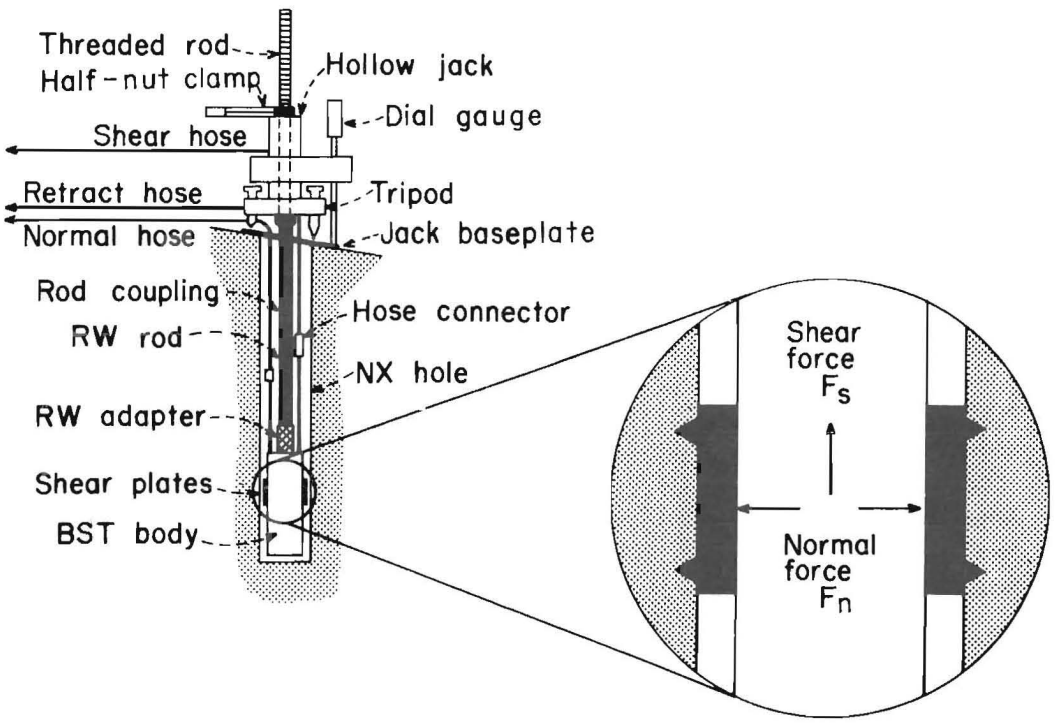

Figure B-6.—Schematic of borehole shear tester (BST) in borehole (32).

Figure B-7.—Borehole shear tester (BST). Top, installation in roof borehole; bottom, control console.

APPENDIX C.—DETERMINATION OF STRESS AND STRESS CHANGES FROM HYDRAULIC BOREHOLE PRESSURE CELL DATA

The following sections describe the derivation of equations for determining absolute ground stresses and stress changes from borehole pressure cell (BPC) and cylindrical pressure cell (CPC) data. The calculation procedures for the instrumentation configuration described in the main text are also presented.

ABSOLUTE STRESSES

The equations describing the pressure convergence method are inadequate for determining stresses from cells installed in various rock types. The inclusion theory includes the elastic properties of the cell-grout materials to determine the stress within an inclusion and results in equations of the same general form as those for the pressure convergence method. It is not required that the BPC unit behaves exactly as an elastic inclusion; therefore, additional factors were included to calibrate the BPC's with the CPC. Thus, the material factors from the inclusion theory are used to determine the relative response of cells in different rock types, while additional response factors account for non-ideal and inelastic behavior of the rock-cell system. The following derivation details the steps taken in developing the equations which were used for subsequent analyses.

Because the BPC's are directional (fig. 13),[1] the subscripts x and y will be employed to qualify certain parameters. The x subscript will denote those parameters associated with the BPC's oriented to measure vertical pillar pressures or roof pressures in the east-west direction (2-ft depth). The y subscript will denote the parameters associated with the BPC's measuring horizontal pillar pressures or roof pressures in the north-south direction (4-ft depth). The subscripts are applied to the cell pressure, the material factor for specific rock types, and the ground stress corresponding to the cell orientation. Additionally, the subscript c will be used to denote parameters associated with the CPC's.

The pressure convergence method enables determination of absolute stresses once the cell pressures have established equilibrium with the stresses in the rock mass. The cell pressures and ground stresses are related through the following equations (*45*):

$$Px = w\,(Nx + R \cdot Ny) \qquad \text{(C-1)}$$

$$P_y = w\,(N_y + R \cdot Nx) \qquad \text{(C-2)}$$

$$Nx + Ny = Pc \,/\, (1-\nu_c) \qquad \text{(C-3)}$$

where Px, Py = BPC cell pressures at equilibrium,

Nx, Ny = ground stresses,

w = response factor,

R = geometry factor (= 0.185 for current cell),

Pc = CPC cell pressure at equilibrium,

and ν_c = Poisson ratio of rock at CPC location.

When all cells, both BPC's and the CPC, are installed in the same rock type, the response factor, w, can be determined from the three cell pressures and used to determine stresses using packages consisting only of the two BPC's. These equations are inadequate if the rock type and response factor for each cell are different. When the cells are installed in different rock types, the response factors and ground stress cannot be determined from the cell pressures alone. To overcome this difficulty, the pressure convergence method was modified, using the elements of inclusion theory to determine the response factors.

The modified method assumes that in reaching equilibrium, the plastic deformation of the borehole results in a configuration in which the BPC behaves as a solid inclusion. However, the presence and geometry of the flat jack in the cell may not result in a direct correspondence between the inclusion stresses and the cell pressure. Therefore, two additional response factors were added to the inclusion theory to account for imperfect response of the flat jack to the inclusion stresses. The derivations of the equations, which define this modified inclusion method, are given below.

The relationships between the ground stresses and the inclusion stresses, at equilibrium, are as follows:

$$Ix = K(Nx + S \cdot Ny) \qquad \text{(C-4)}$$

$$Iy = K(Ny + S \cdot Nx) \qquad \text{(C-5)}$$

where Ix, Iy = stresses in the inclusion, psi,

Nx, Ny = ground stresses, psi,

and K, S = material factors.

[1]Figure numbers without a C- prefix refer to figures in the main text.

The material factors K and S are given by the following equations (*61*):

$$K = (D + A) / 2 \qquad \text{(C-6)}$$

$$S = (D - A) / (D + A) \qquad \text{(C-7)}$$

where D and A are functions of the elastic properties of the rock and inclusion as shown below for plane strain conditions:

$$D = 2\mu_i(1-\nu_r) / ((1-2\nu_i)\mu_r + \mu_i) \qquad \text{(C-8)}$$

$$A = 4\mu_i(1-\nu_r) / (\mu_r + (3-4\nu_r)\mu_i) \qquad \text{(C-9)}$$

where μ_i, μ_r = modulus of rigidity of inclusion and rock materials,

$\mu = E / 2(1 + \nu)$, psi,

and ν_i, ν_r = Poisson's ratio of inclusion and rock materials.

It is assumed that the response of the flat jack to the inclusion stresses will be proportional to the weighted sum of the inclusion stresses. The stresses are weighted by the respective cross-sectional areas of the flat jack which are normal to each stress. Thus, the flat jack pressure (cell pressure) is given by the following equation:

$$Px = z(Ix \cdot Ap + Iy \cdot Ae) \qquad \text{(C-10)}$$

$$Py = z(Iy \cdot Ap + Ix \cdot Ae) \qquad \text{(C-11)}$$

where Px, Py = BPC cell pressures, psi,

z = proportionality factor,

Ap = area in plane of flat jack, in^2,

and Ae = area of edge of flat jack, in^2.

By dividing equations C-10 and C-11 by Ap, the following equations are obtained:

$$Px = Z(Ix + R \cdot Iy) \qquad \text{(C-12)}$$

$$Py = Z(Iy + R \cdot Ix) \qquad \text{(C-13)}$$

where Z = response factor,

and R = geometry factor = Ae/Ap = 0.185 for current cell.

Since the cells oriented in the x and y directions may be installed in different rock types, the material factors K and S are computed separately for each rock type, as Kx, Ky, Sx, and Sy. Substituting equations C-4 and C-5 for I_x and I_y in equations C-12 and C-13 results in the following equations:

$$Px = ZKx((1 + R \cdot Sx)Nx + (R + Sx)Ny) \qquad \text{(C-14)}$$

$$Py = ZKy((1 + R \cdot Sy)Ny + (R + Sy)Nx). \qquad \text{(C-15)}$$

Note: The factors Z and R depend on the grout-flat jack coupling and are independent of the rock properties; therefore, they are the same for both cells and are not subscripted. Rearranging terms in equations C-14 and C 15 yields the following expressions for Nx and Ny:

$$Nx = \frac{(1 + R \cdot Sy)Px/Kx - (R + Sx)Py/Ky}{Z(1 - R^2)(1 - SxSy)} \qquad \text{(C-16)}$$

$$Ny = \frac{(1 + R \cdot Sx)Py/Ky - (R + Sy)Px/Kx}{Z(1 - R^2)(1 - SxSy)}. \qquad \text{(C-17)}$$

In equations C-16 and C-17, the only unknown factor, Z, can be determined by substituting equations C-16 and C-17 into equation C-3 and solving for Z. The following equation is used to determine Z for a complete BPC-CPC package:

$$Z = \frac{(1 - Sy)Px/Kx + (1 - Sx)Py/Ky}{(1 + R)(1 - SxSy)Pc/(1-\nu_c)}. \qquad \text{(C-18)}$$

The above equations C-14 through C-18 form the basis for the analysis of absolute stresses. The actual procedures used to apply these equations to determine absolute stresses will be discussed in the following sections.

Absolute Pillar Stresses

Because all cells were installed in the same material, coal, the basic equations can be simplified by setting Kx = Ky = K, and Sx = Sy = S. The simplified form of equations C-14 through C-18 are as follows:

$$Px = ZK((1 + RS)Nx + (R + S)Ny) \qquad \text{(C-19)}$$

$$Py = ZK((1 + RS)Ny + (R + S)Nx) \qquad \text{(C-20)}$$

$$Nx = \frac{Px(1 + RS) - Py(R + S)}{ZK(1 - R^2)(1 - S^2)} \qquad \text{(C-21)}$$

$$Ny = \frac{Py(1 + RS) - Px(R + S)}{ZK(1 - R^2)(1 - S^2)} \qquad (C\text{-}22)$$

$$Z = \frac{Px + Py}{K(1 + R)(1 + S)Pc/(1 - \nu_c)}. \qquad (C\text{-}23)$$

These simplified equations reduce to the unmodified pressure convergence equations when the inclusion material factor, S, is zero. In general, S is nonzero; however, for the range of elastic properties typically encountered, S ranges from approximately -0.1 to +0.1. The terms in the above equations involving 1 + RS and 1 - S^2 are approximately equal to one, which corresponds to the pressure convergence theory. However, the R + S term can vary significantly from the value of R in the pressure convergence theory, since R and S are the same order of magnitude. Thus, the modified inclusion method and the pressure convergence method produce similar stress values when S is approximately zero, but produce increasingly different values as S becomes different from zero. The specific elastic properties of the rock which produce a zero value for S are given by the following equation:

$$\nu_r = 0.25(1 - (1 - 4\nu_i)\mu_r/\mu_i). \qquad (C\text{-}24)$$

For most rocks, the required value of Poisson's ratio to produce a zero value for S is slightly less than 0.25. Thus, when Poisson's ratio is about 0.25, both methods should provide similar results.

Certain assumptions were made regarding both the vertical and horizontal stress distributions within the pillars to account for the nonideal arrangement of pressure cells. Ideally, two BPC's and one CPC should be installed at approximately the same location such that all cells experience identical stress conditions. However, to minimize the number of cells and boreholes required, the simplified plan described earlier was implemented. Under the simplified plan, only one CPC was installed in pillar D, and a total of four BPC's, one in each pillar, were installed and oriented to measure horizontal pressure. The required assumptions were as follows:

1. linear variation of vertical stress and cell pressure between adjacent cells measuring vertical pressures,
2. constant horizontal stress throughout each pillar, and
3. constant cell response factor, Z, for all pillars.

The first assumption was used to determine an equivalent vertical cell pressure at the horizontal BPC and CPC locations. Since the true vertical stress distribution is unknown, an assumption of a linear variation between cells appears to be reasonable.

The second assumption was used to provide equivalent horizontal cell pressures at the vertical BPC locations. A supplementary analysis using a nonuniform distribution of horizontal stress was performed to evaluate the significance of the error incurred by assuming a uniform distribution. The nonuniform distribution used for comparison consisted of horizontal stresses that increase linearly from zero at the pillar edge toward the pillar interior. The vertical stresses calculated using the nonuniform distribution were approximately 10% higher than the stresses calculated using the uniform distribution. The difference between stresses calculated using the two distributions decreased toward the pillar interior and were approximately equal (less than 1% difference) at the deepest cells. Because the non-uniform distribution used for comparison is thought to be an extreme condition, the error in vertical stresses due to the assumption of uniform horizontal stress should be well below 10%. This level of error is consistent with the resolution of the recording charts and is considered acceptable for this study.

Since all the pillar cells were installed in approximately the same horizon in the coal seam, it appears reasonable to assume that the cell response factor, Z, is the same in all pillars. The detailed procedures for calculating the pillar stresses are described.

1. The material constants K and S were calculated from the elastic constants of the coal and grout using equations C-6, C-7, C-8, and C-9. For the coal, the values of the elastic constants, E = 337,000 psi and ν = 0.30, were obtained from tests performed by the mine operator. The elastic constants for the grout, E = 9.65×10^6 psi and ν = 0.17, were obtained from reference (*62*) for lumnite cement.
2. Equivalent vertical cell pressures were determined for the CPC and horizontal BPC locations in pillar D by linearly interpolating between the cell pressures from the two adjacent vertical BPC's.
3. An equivalent horizontal cell pressure was determined for the CPC location using the following form of equation C-22:

$$Py = \frac{NyZK(1 - R^2)(1 - S^2)}{1 + RS} + \frac{R + S}{1 + RS} Px. \qquad (C\text{-}25)$$

By substituting known values for Px, Py, R, and S from the CPC and horizontal BPC locations, two equations result which are solved to find Py at the CPC location. The following equation summarizes the solution of these two equations:

$$(Py)_c = \frac{R + S}{1 + RS} ((Px)_c - (Px)_h) + (Py)_h. \qquad (C\text{-}26)$$

The subscripts c and h in equation C-26 represent cell pressures from the CPC and horizontal cell, respectively.

4. The equivalent vertical and horizontal cell pressures at the CPC location are substituted in equation C-23 to determine the response factor, Z.

5. The uniform horizontal pillar stress is found by substituting the equivalent vertical and horizontal cell pressures at the CPC location and the response factor, Z, in equation C-22.

6. The vertical pillar stress at each BPC location is determined using the following form of equation C-19:

$$Nx = \frac{Px/ZK - (R + S)Ny}{1 + RS}. \qquad (C\text{-}27)$$

The remaining pillars are analyzed using step 2 for the horizontal BPC location only; step 5 using cell pressures for the horizontal BPC and the response factor, Z, from pillar D; and step 6 for all cell locations.

Figure C-1 shows a plot of the response factor, Z, from intersection widening through the end of the monitoring period. It is concluded that the stabilization of the response factor values, which occurred 110 days after widening, indicates the actual date that equilibrium occurred.

Absolute Roof Stresses

Analysis of absolute roof stresses using the BPC-CPC packages was complicated by the spatial separation of the three cells and by installation of the cells in two different rock types. In addition, the magnitude and direction of the horizontal secondary principal stresses cannot be determined using the current package configuration. The packages can only be used to determine the components of the horizontal stress aligned with the measurement directions of the BPC's.

Of necessity, the cells were separated in the borehole and were located in distinctly different layers of the roof having different physical properties. Equations C-14 through C-18 were developed to account for these differences, but they do not directly address the likely variations of the magnitude and direction of the horizontal stresses in the different roof layers. This variation in stress may arise from stress concentrations around the opening and from additional concentration of stress in the stiffer roof layers. For this analysis, it was assumed that the directions of the horizontal stresses were identical in all layers, but that the magnitudes of the stresses were different. Figure C-2 shows a theoretical stress distribution around an elliptical hole in an elastic plate. This configuration corresponds approximately to a diagonal section through the intersection. The stresses at the BPC's, 2 and 4 ft deep, and the CPC, 6 ft deep (fig. C-2) are estimated to be, respectively, 1.36, 1.23, and 1.16 times greater than the horizontal field stress (*51*).

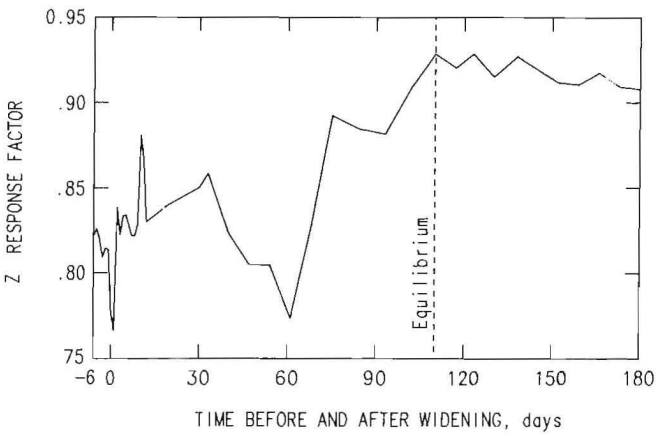

Figure C-1.—Response factor in pillars.

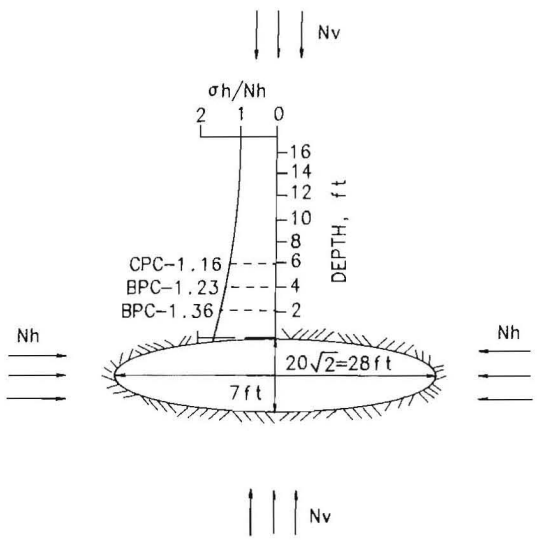

Nv/Nh=400/950 based on Bureau stress-relief measurments

Figure C-2.—Horizontal stress concentration around elliptical opening.

The actual distribution of stresses in the roof is not expected to agree with the above estimates because of the rectangular cross-sectional shape of the entries, the three-dimensional character of the intersection geometry, and the nonisotropic and inelastic properties of the roof and pillars. In addition, the stresses at the lower BPC, in shale, are estimated to be less than the stresses at the upper cells, in limestone, by a factor equal to the ratio of the elastic moduli of the two rocks. This factor is 4.28/0.68 or 6.29. The corresponding reduction factor for stresses at the lower BPC compared with stresses at the CPC due to the elastic distribution is 1.36/1.16 or 1.17. Thus the stiffness ratio, 6.29, appears to be the predominant factor influencing the stress distribution. To account for the variation in stress due to different rock types, the material factor, K_x, is reduced by the stiffness ratio before substitution into equations C-11 through C-15. The resulting calculated stresses correspond to the limestone layer and the stresses in the shale layer can be found using the stiffness ratio.

The response factor, Z, for package 3, at the southwest corner of the intersection (fig. 13), remained relatively constant after equilibrium was reached, whereas the response factors for the other two packages varied widely. Since the response factor should be constant for a given cell configuration, the average value of the response factor for package 3 was used to calculate the stresses for all packages.

Analysis using the current three-component cell package can only determine the component stresses aligned with the BPC's. However, under certain circumstances, a four-component cell package consisting of three BPC's and one CPC provides sufficient information to determine both the magnitude and direction of the horizontal secondary principal stresses. A procedure was developed to analyze pressure data from a four-component package; however, the procedure is limited to situations where the material and response factors can be assumed equal for all cells. To meet this limiting condition, the instrumentation plan should be designed such that all cells are installed in the same type rock and are subjected to identical stress conditions. These restrictions may be met, approximately, by installing the cells at the same depth in separate, closely spaced boreholes or in a single borehole located in a thick layer outside the influence of the opening. The procedure, described by the following steps, applies to a package having BPC's oriented 60° apart.

1. The material factors, K and S, are determined for the appropriate rock type using equations C-6 through C-9.

2. Intermediate factors, A and B, are calculated using the following equations:

$$A = \frac{P_1 + P_2 + P_3}{3K(1+R)(1+S)} \tag{C-28}$$

$$B = \frac{\sqrt{2}}{3K(1-R)(1-S)} [(P_1-P_2)^2 + (P_2-P_3)^2 + (P_1-P_3)^2]^{1/2} \tag{C-29}$$

where P_1, P_2, P_3 = BPC cell pressures. The measurement direction of cell-2 is 60° counterclockwise from the direction of cell-1, and the direction of cell-3 is 120° counterclockwise from cell-1.

3. The response factor, Z, is determined using the following equation:

$$Z = \frac{2A(1-\nu_c)}{Pc}. \tag{C-30}$$

4. The principal stresses, N_1 and N_2, are calculated as follows:

$$N_1 = \frac{A + B}{Z} \tag{C-31}$$

$$N_2 = \frac{A - B}{Z}. \tag{C-32}$$

5. The orientation of the principal stresses is found from the following equation:

$$\theta = \frac{1}{2} \tan^{-1} \left[\frac{\sqrt{3}\,(P_3-P_2)}{2P_1-P_2-P_3} \right]. \tag{C-33}$$

The correct value of the rotation angle, θ, is found by considering the quantities $\sqrt{3}\,(P_3 - P_2)$ and $2P_1 - P_2 - P_3$ in equation C-33 as y and x components, respectively, of a vector in cartesian coordinates. The angle between the vector and positive x-axis is two times the angle between the direction of cell-1 and N_1. The angular sense of rotation from cell-1 to N_1 is the same as the rotation of the vector to the positive x-axis.

STRESS CHANGES

The cell pressures used to calculate stress changes correspond to the end of stage 1 and the beginning of stage 3 in figure 12. The cell pressures were relatively constant during these periods and allowed a consistent determination of pressures for all cells. The transient effects in stage 2 made determination of representative

and consistent pressure differentials difficult; therefore, the stage 2 data were not used for analysis. Using the procedures discussed in the previous section, absolute stresses were calculated for the roof and pillars, both before and after widening operations, using the initial (stage 1) and final (stage 2) cell pressures. The stress change is just the difference between these two absolute stresses. The cell pressure data used for the stress change calculations were obtained before the cells had reached equilibrium; therefore, the absolute stresses used to find stress changes are not considered accurate. However, since the period between the initial and final data sets is relatively short, approximately 4 days, the influence of cell-to-rock adjustments in reaching equilibrium should not be significant, and the calculated stress changes should be reasonably accurate. It is likely that a nonuniform distribution of stress changes occurs during widening, both in the roof and pillars. Thus, the three cells in a given package, two BPC's and one CPC, may experience different stress changes resulting in different calculated response factors before and after widening. To minimize this effect, an average of the response factors obtained before and after widening was used to calculate absolute stresses.

Stress changes were also determined using the method introduced by Babcock (*4*). This method is described by the following equations relating initial and final cell pressures to the corresponding change in ground stress:

$$Cx - Cy/3 = 2/(3M) \ln (Px/P'x) \qquad (C\text{-}34)$$

$$Cy - Cx/3 = 2/(3M) \ln (Py/P'y) \qquad (C\text{-}35)$$

where Cx,Cy = ground stress changes in x and y directions,

P'x,P'y = initial cell pressures,

Px,Py = final cell pressures,

and M = response factor.

The response factor, M, is determined using the following equation when ground stress and cell pressure are specified in pound per square inch units:

$$M = 4.238 \left(\frac{1 - \nu^2}{E} \right)^{2/3} . \qquad (C\text{-}36)$$

To accommodate the shale and limestone in the roof and the associated variation of horizontal stress, the response factor, M, was determined for each rock type and denoted as Mx and My. In addition, the factor Mx was reduced using the stiffness ratio of the limestone layer relative to the shale layer. Table C-1 lists the elastic properties, base response factors, and adjusted response factors for the shale, limestone, and coal present at the test site.

Pillar Stress Changes

Because of the spatial separation of the BPC's in the pillars, two assumptions were made regarding the distribution of cell pressures and horizontal stresses. These assumptions, which are identical to those made for the absolute pillar stress calculations, are as follows:

1. A linear distribution of cell pressure between cells, and
2. A uniform distribution of horizontal stress throughout the pillar.

A separate analysis was performed using a linearly increasing distribution of horizontal stress to evaluate the validity of the second assumption. Because the stress changes were relatively small, the differences between the calculated values for the two distributions are a large fraction of the total stress change. However, the shapes of the stress change distributions are not significantly affected by variations in the horizontal stress distribution. Thus, the evaluation of pillar stress changes was directed more toward analyzing the relative distribution of the changes rather than toward analysis of the magnitudes of the stress changes.

Table C-1.—Response factors for determining ground stress changes at test site

Parameter	Shale (Mx)	Limestone (My)	Coal (M)
Young's modulus, (E) . . . . 10^6 psi . .	0.680	4.280	0.337
Poisson's ratio (ν)	0.20	0.34	0.30
Response factor	0.000533	0.000148	0.000822
Reduction factor	6.29	1	1
Adjusted response factor	0.000085	0.000148	0.000822

Simultaneous solution of equations C-34 and C-35 result in the following equations for the stress change:

$$Cx = 1/(4M)\ [3 \ln (Px/P'x) + \ln (Py/P'y)] \qquad (C\text{-}37)$$

$$Cy = 1/(4M)\ [3 \ln (Py/P'y) + \ln (Px/P'x)]. \qquad (C\text{-}38)$$

The pressure cell data for each pillar were analyzed using the following procedure:

1. Equivalent initial and final vertical cell pressures were determined for the horizontal cell location by interpolating linearly between the corresponding pressures from the two adjacent vertical cells.
2. Using equations C-37 and C-38, the stress changes at the horizontal cell location were determined. Because it was assumed that the horizontal stress is uniform, the change in horizontal stress was also assumed to be uniform throughout the pillar.
3. By assuming a constant horizontal stress change at all cells, the following relation was derived to determine an equivalent ratio of final to initial horizontal cell pressure:

$$Py/P'y = [(P'x/Px)\exp(4MCy)]^{1/3}. \qquad (C\text{-}39)$$

Substitution of equation C-39 in equation C-37 yields the following equation to determine the vertical stress change at the vertically oriented cells:

$$Cx = (2/(3M))\ln(Px/P'x) + Cy/3. \qquad (C\text{-}40)$$

Roof Stress Changes

To determine the stress changes in the roof, the response factors Mx and My were determined for the shale and limestone layers and adjusted for expected stress concentrations (table C-1). The response factor for shale, Mx, was substituted into equation C-34, and the response factor for limestone, My, was substituted into equation C-35. The solution of these two equations provides the stress changes, Cx and Cy, in the limestone layer as follows:

$$Cx = \frac{1}{4}\left[\frac{3\ln(Px/P'x)}{Mx} + \frac{\ln(Py/P'y)}{My}\right] \qquad (C\text{-}41)$$

$$Cy = \frac{1}{4}\left[\frac{3\ln(Py/P'y)}{My} + \frac{\ln(Px/P'x)}{Mx}\right]. \qquad (C\text{-}42)$$

INT.BU.OF MINES,PGH.,PA 29282

☆U.S. GOVERNMENT PRINTING OFFICE:1991-511-270